Studies on the Relativistic Electrons and X-Rays Generated by Laser WakeField Accelerators

Michael Samuel Bloom

Imperial College London

2014

Submitted in partial fulfilment of the requirements for the degree of Doctor of Philosophy of Imperial College London

Department of Physics
Imperial College London
Prince Consort Road
London SW7 2BZ

Declaration of Originality

I hereby declare that the material of this thesis, which I submit for the award of Doctor of Philosophy, is entirely my own work unless otherwise cited or acknowledged within the body of the text.

Abstract

Laser wakefield accelerators (LWFAs) operate through a high intensity ultra short laser pulse exciting a relativistic density wave in a plasma. I carried out experiments constructing LWFAs using lasers of a wide range of powers. Thereby allowing me to examine the generation of electrons and x-rays under these different conditions. The comparison of these results with my own and existing analytical models and computational modelling is discussed.

In fulfilment of this, I developed novel techniques to measure hard x-rays in the tens of KeV energy range. In measurement of the relativistic electrons I found it possible to develop techniques to not only accurately measure the energy but also discern the three momentum vectors of electrons measured on a multiscreen electron spectrometer.

As LWFAs open up the ability to produce high energy electron beams without the need of tens of meters of RF acceleration cavities and the lasers used to drive them can also be made relatively compact perhaps one of the most exciting application of this is the production of hard x-rays for imaging. As the source size of a LWFA betatron source is typically of micron scale, I investigated using LWFA derived x-rays for phase contrast imaging.

Acknowledgements

First I would like to express my sincere thanks and appreciation to my Ph.D. supervisor Stuart Mangles, I couldn't ask for a better supervisor, brilliant, enthusiastic, attentive and always willing to help. I would like to thank Zulfikar Najmudin who with an open door was happy to help with any tricky physics I was tackling. AE Dangor for always showing an interest and being willing to discuss my work.

I would deeply like to thank and acknowledge those people who worked on and around my first experiment at the University of Michigan: S. Kneip, C. McGuffey, F. Dollar, V. Chvykov, G. Kalintchenko, K. Krushelnick, S. P. D. Mangles, T. Matsuoka, Z W. Schumaker, A. G. R. Thomas, and V. Yanovsky. Especially Chris McGuffey and Stefan Kneip for showing me the ropes, and Franklin, Alec, Louise, and Karl for making me feel so welcome.

Then I must acknowledge and thank everyone who worked so hard to make the experiment at the university such a success: Guillaume Genoud, Kristoffer Svensson, Stuart Mangles, Matthias Burza, Anders Persson, Jens Uhlig, and Claes-Goran Wahlstrom. Special thanks go to: Gullaume from whom I learned such a great deal; Kristoffer who worked long through the night and morning with me and with whom I enjoyed the portal song; Claes-Goran who was simply amazing, from jury-rigging pulleys and springs when every motor failed, to cleaning the lab despite being the most senior person there, to producing a residual gas analyser from absolutely nowhere; and Anders Persson who built such a wonderful laser, let me use it, and came in early on a Saturday morning so I could have just one more day of shots. Not to forget Laserlab Europe for paying for it.

For the Gemini data in this work the Central Laser Facility at the Rutherford Appleton Laboratory deserve an awful lot of credit for pushing forward the boundaries of laser science and letting academic students like my self use them. PP Rajeev, P Foster, RJ Clarke, SJ Hawkes, CJ Hooker, O Chekhlov, EJ Divall, K Ertel, and of course the support personnel, engineers, technicians and Target Fabrication. Then to the those who worked so hard to make the experiment a success: M. J. Streeter, S. Kneip, R Bendoyro, A Dopp, J. Holloway, J Jiang, N Lopes, Z. Najmudin, H. Nakamura, D. Symes and S. P. D. Mangles. Special thanks goes to Matt Streeter and Stefan Kneip for their hard work as TAOs (Target Area Operators) allowing me to take my data; to Dan Symes who is amazing and greeted the sun with me on one night of shots while also stepping in as emergency TAO; to Donna Wyatt and

Christopher Spindloe at Target Fabrication RAL- Chris for helping bring so many of my novel filter designs to life, not just those in this thesis, and Donna for building them with care and precision; Darren Neville and his team who literally did the heavy lifting; and Rob Clarke for his extra help calibrating my x-ray detector using his Fe-55 source.

I would also like to thank Jason Cole, Jimmy Holloway, Scott Mandry, Nakamura Hirotaka, and Kristjan Poder who worked so hard on an experiment that, though it didn't make it into this thesis, taught me a great deal about being a TAO. Emma Harris from The Institute of Cancer Research with whom I had many long decisions on phase contrast imaging. Bob Bingham, Peter Norreys, and Raoul Trines for taking the time discussing with me my crazy ideas, and understanding some of what is possible in our field.

I would like to mention Diego Garcia-Florez who showed me by teaching something to someone else you can learn a lot and who was a constant source of enthusiasm and who, despite being younger than myself, died in 2011 before having a chance to finish his PhD. Both a huge personal and professional loss.

Cheers and thanks goes to everyone else in the plasma group at Imperial: Nick, Tom, Matt, Claudio, Kris, John, Charlotte, J Schreiber, Sabrina, Chris, Chris Ridgers to name just a few. Holger Schmitz whom was kind enough to teach me to improve my programing skills as well as play Go. Collectively you all helped to make my PhD an enjoyable experience.

I would also like to mention Alan Michette who was the teacher who first got me excited over laser plasma physics at Kings College London and who passed away in 2013. He was an inspirational teacher and I regret I wasn't able to take up his invitation to visit Kings to discuss x-ray sources in 2012.

To my friends and family, not already mentioned, Uncle Ron who was always interested in discussing Radiology; My Aunt Elisabeth who was always willing to discuss the finer points of English grammar; Bob and Deb; Adam Newton for his help with the picture of the Death Star, who is a far better artist than I, but never failed to remind me of the connection between art and science. To my friends, for their help keeping me sane. Finally to my parents Anne and Basil, it would have been impossible for me to have come this far without your love and support.

Michael Bloom 2014

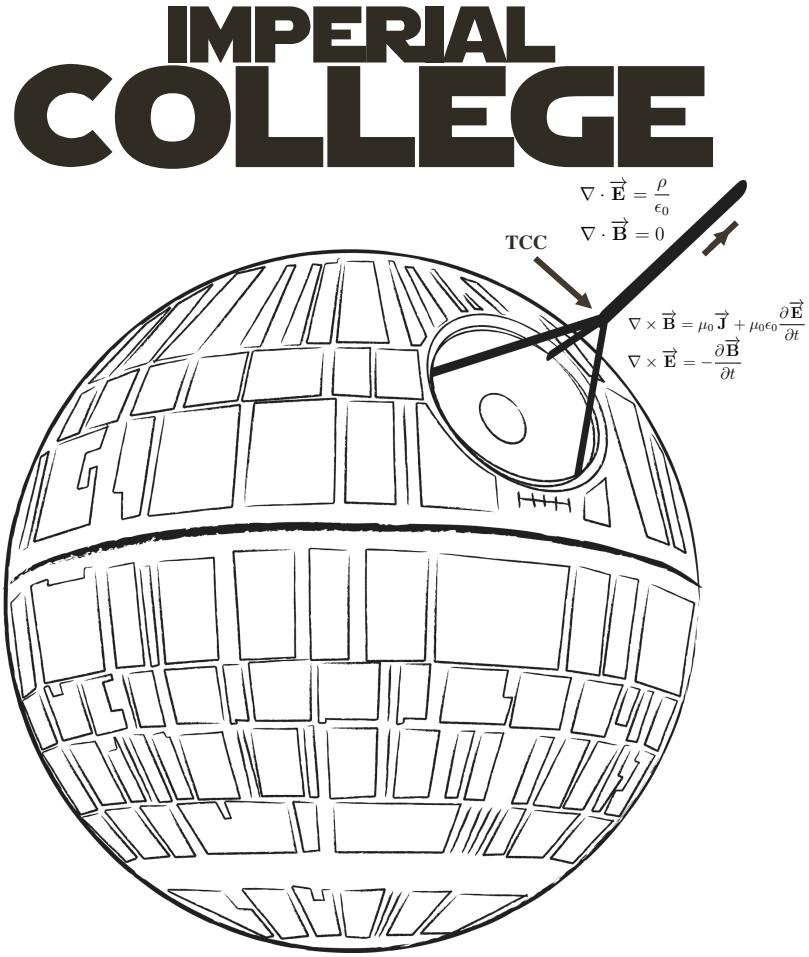

LASER PLASMA PHYSICS GROUP

Michael Bloom 2014[1]

Our dreams; Are our wings.

[1]There is a tradition in our group of PhD students putting a small, often humorous, and personal touch at the beginning of their thesis. Image above is meant as such. I of course have no claim on the trade name Imperial College or any material belonging to Star Wars.

Role of the Author

In the experiment in Lund, discussed in chapter 4, the author took a leading role in setting up the experiment and in the shot schedule. I was responsible for collecting data on all electron diagnostics, and took a leading role in analysis and interpretation of the electron data.
For the calibration of the x-ray detection system I was responsible for setting up the experiment (assisted by Rob Clarke) and for analysis of the data.
In the experiment on Astra Gemini the experiment was run by target area operators M. Streeter and S. Kneip. I took a leading role in setting up the experiment and collecting data and led the design of the x-ray detection system including designing the filter pack suitable for measuring high energy x-rays.
I was responsible for all analysis of the electron spectrometer data, including developing the two screen algorithm, for all analysis of the X-ray data and for interpretation and formation of main conclusions, including development of the PIPE model.

Contents

1 Introduction. **10**

2 Theory. **19**

2.1 High Intensity Short Pulse Laser Concepts. 19

2.1.1 Rayleigh Range 19

2.1.2 The laser strength parameter a_0 19

2.1.3 The size of a diffraction limited focal spot. 20

2.2 Concepts of Plasma Physics. 21

2.2.1 Debye length. 21

2.2.2 Plasma frequency 21

2.2.3 Dispersion relation of an Electromagnetic wave in Plasma . . . 22

2.2.4 Dispersion relation of an Electron Plasma Wave. 24

2.2.5 Critical density 25

2.3 Concepts of Laser plasma interactions. 27

2.3.1 Wave Interactions Inside a Laser Wakefield Particle Accelerator 27

2.3.2 Rigorous Mathematical Treatment of Laser Propagation in Underdense Plasma 29

2.3.3 Wave Breaking 35

2.3.4 The critical power for self focusing 37

2.3.5 Laser Depletion Length 37

2.3.6 The Dephasing Length 37

2.3.7 Betatron Radiation 38

3 Methods. **39**

3.1 Electron Measurement. 39

3.1.1 Electron Spectrometry. 39

3.1.2 Electron Profile Measurements. 49

3.2 X-Ray Measurement . . . 49
3.2.1 Filter Pack Design . . . 50
3.2.2 Data Treatment for X-ray Spectrum . . . 55
3.2.3 Princeton PIXIS camera . . . 57
3.2.4 Princeton PIXIS Camera System Calibration . . . 60

4 Lund Experiment **67**
4.1 Experimental Set Up. . . . 67
4.2 Examining the energy-density threshold for wavebreaking . . . 71
4.2.1 Model of The Self-Injection Threshold in Self-Guided Laser Wakefield Accelerators. . . . 78
4.2.2 Comparing The Self-Injection Threshold Model With The Experiment. . . . 80

5 Experiments Using The Astra Gemini Laser **82**
5.1 Experimental Set-Up . . . 83
5.2 3D Momentum Distributions of GeV Electron Beams . . . 85
5.3 A Model For The Electron Energy As Function Of Density Including The Pre-Injection Pulse Evolution Length . . . 89
5.3.1 A Simple Model Applied To Maximum Achievable Electron Energy In The LWFA . . . 92
5.4 X-Ray Measurements . . . 97

6 Discussion, Conclusions and Outlook **104**
6.1 Threshold For Self-Injection In A Self-Guided LWFA . . . 104
6.2 Two-Screen Spectrometer Method for Measuring the 3D Momentum Distributions of GeV Electron Beams . . . 105
6.3 The Pre-Injection Pulse-Evolution Length of a LWFA . . . 106
6.4 betatron X-Rays from LWFAs . . . 106
6.5 Phase Contrast Imaging . . . 109
6.6 Future Directions . . . 109

A Formula **113**
A.1 Maxwell's Equations . . . 113
A.2 Taylor's Series . . . 113
A.3 Miscellaneous . . . 114

A.4 Identities 115

B Derivation of the Debye length **116**

C Derivation of the Plasma Frequency **118**

D Phase Velocity, Group Velocity, and Dispersion Relation **121**

Chapter 1

Introduction.

Plasma based accelerators are of great interest due to their ability to sustain extremely large accelerating gradients of about three orders of magnitude greater than that obtained in conventional linacs [1] . The consensus in the world high energy physics community is that a TeV-scale lepton collider would be the next step after the LHC. As such, plasma based accelerators represent an option as they would, due to their smaller size, afforded by their higher accelerating gradients, ideally be an order of magnitude lower in cost. However there are a huge number of technical, and plasma physics challenges which would need to be overcome to reach these kinds of energies. However lower energy plasma based accelerators can be produced. In this work I will be describing my studies on one such type of accelerator, and I will show that it is capable of producing electron beams of GeV-scale over accelerating lengths on the cm-scale, so allowing for table top sized machines.

This thesis is concerned with laser wakefield plasma accelerators. Laser wakefield accelerators (LWFAs) open up the ability to produce high energy electron beams without the need of tens of meters of radio frequency acceleration cavities. One of the most exciting application of this, because the lasers used to drive them can also be made relatively compact, is the production of hard x-rays which before now had required large synchrotron, and free electron-laser facilities. My studies are on the electron beams generated by laser wakefield accelerators, and the x-rays generated by the electrons while they are in the accelerator.

[1] Conventional radio-frequency linear accelerators are currently limited to ≈100 MV/m before material breakdown begins to occur [1]. Where as in plasma based accelerators accelerating gradients on the order of 100 GV/m have been produced [2]. The electric fields that can be sustained by plasma waves can be approximated by $E_0 = cm_e\omega_p/e$ see section 2.3.3 for details.

I will start with a basic description of what a LWFA is, and how it generates x-rays. I will then provide a literature review in this chapter. The second chapter will describe standard theory used in this thesis. In the third chapter experimental methods will be presented. I will discuss novel techniques I implemented to measure the 3 momentum components of accelerated electrons, and to measure x-rays in the 1-100 keV range.

In the fourth (and first experimental) chapter an 18 TW laser is used to create a self-guided laser wakefield accelerator. A detailed study is conducted to examine the plasma density threshold for electron self injection in a self guided LWFA, a parameter critical for both electron, and x-ray generation. An analytical model is derived, and compared to experiment.

In the fifth (and second experimental) chapter a 180 TW laser is used to again create a self-guided laser wakefield accelerator. It is shown that this produces much higher energy electrons, up to 1.3 GeV. The x-rays are measured, and found to have betatron like spectra with critical energies of 15-30 keV, and brightness of 10^{24}-10^{25} photons per second per mrad^2 per mm^2 per 0.1% bandwidth. The effects of plasma density on electron energy are examined in detail, and a simple model is compared to experiment. The transverse momentum of the electrons is measured.

In the sixth, and final chapter the conclusions from the two experiments are discussed, and the connections between the results of the studies in this work are made clear.

Laser Wake Field Accelerators

In a LWFA a high intensity short laser pulse excites a relativistic plasma wave in a low density plasma. If the electron density of the plasma is n_e, and the critical density for the laser is[2] $n_c = (2\pi c/\lambda_0)^2 m_e \epsilon_0 / e^2$, then the Lorentz factor of this excited wave's phase velocity will be[3]: $\gamma_{\phi p} = \sqrt{n_c/n_e}$. This plasma wave can be an ideal accelerating cavity, with fields in excess of 100 GeV/m.

As in the case of the experiments reported here, by ensuring the amplitude of the laser pulse is sufficiently large the plasma wave can be driven beyond breaking. This causes electrons to become self-injected in the laser's wake, and experience the

[2]Discussed in section 2.2.5.

[3]Derived in section 2.3.1, equation 2.55.

accelerating force of the plasma wave. Additionally if the laser pulse's power is greater than[4] $P_c = 17 \times 10^9 (n_c/n_p)W$, then a focused laser pulse will not diffract away but instead can be guided through the plasma until its power falls below this value, this is known as the critical power for self focusing. The depletion length, the distance the laser pulse propagates through the plasma before its energy is depleted can be estimated as[5] $L_{dp} = \tau_0 c n_c/n_e$. where τ_0 is the pulse duration of the pulse before entering the plasma.

The first period of the plasma wave behind the laser pulse can be thought of as a spheroid or "bubble" devoid of background plasma electrons travelling at $\gamma_{\phi p}$ behind the laser pulse. Electrons self injected into this bubble will oscillate around its axis as they are accelerated, retaining the transverse potential energy they possessed on entry to the bubble. This is due to the bubble electric fields being directly proportional to the distance from the center of the bubble. Due to this oscillation the electrons will emit synchrotron like radiation.

Literature Review of LWFAs

The laser driven plasma wave accelerator (LWFA) was first proposed 35 years ago in 1979 by Tajima, and Dawson [3], and simulated using what computational means were available at the time.

Despite this early invention the first experimental evidence for the generation of laser induced wake field did not come about until 1993, Hamster [4]. The first example of acceleration from a self-modulated wakefield was by Nakajima in 1995 [5]. The first example of laser wake field acceleration from a broken relativistic plasma wave was by Modena in 1995 [6], and the first experimental observation of laser wake field acceleration (without self modulation) was by Amiranoff in 1998 [7].

The original high powered lasers[6] had too long a pulse duration to allow for resonant driving of plasma waves, where $\tau \approx 1/\omega_p$ is needed. So instead the beat wave scheme was invented (PBWA), where the interference between two relativity long co-propagating laser pulses can be used as the driver for plasma waves for particle acceleration, as outlined in Rosenbluth in 1972 [8]. Though it should be pointed out that the idea for using optical mixing as a plasma density probe was around as

[4] See section 2.3.4.
[5] See section 2.3.5.
[6] Utilising CO_2 or Neodymium:Glass laser mediums.

early as 1964 [9], and was also suggested in Tajima's, and Dawson's original paper. Key experiments into beat wave acceleration, ranging from 1985 to 2006, are given in Clayton et al. 1985 [10], Dangor et al. 1990 [11], Kitawa et al. 1992 [12], Everett et al. 1994 [13], Clayton et al. 1994 [14], Amiranoff et al. 1995 [15], Walton et al. 2002 [16], and Wlaton et al. 2006 [17].

The invention of chirped pulse amplification (CPA) in 1985 [18], revolutionised high powered laser systems, providing shorter, and more powerful laser pulses. This allowed access to Self Modulated Laser Wake Field Accelerator regime (SM-LWFA). Here the laser pulse is self-modulated due to non-linear plasma optical effects caused by the laser pulse's high intensity. This results in the laser pulse, which is originally longer that the plasma period $\tau > 1/\omega_p$, becoming split (through resonant modulation) into a pulse train capable of driving a high amplitude plasma wave. Experiments utilising the SM-LWFA, ranging from 1995 to 2003, include Modena et al. 1995 [6], Coverdale et al. 1995 [19], Ting et al. 1997 [20], Santala et al. 2001 [21], and Najmudin et al. 2003 [22].

SM-LWFA also differed from PBWA in another important aspect. The PBWA was not in of its self a source of electrons. So it was necessary to inject bunches of electrons which where already well localised in both space, and time. This presents a number of technical challenges given that the laser focal spot waist are on the order of $10\mu m$. SM-LWFAs are capable of driving a plasma wave beyond the point of wave breaking (see section 2.3.3), allowing plasma electrons to become trapped in the accelerating structure. This is known as "self trapping". The SM-LWFA can therefore act as its own source of electrons without the need of elaborate injection mechanisms.

Eventually pulses shorter than required for the self-modulation process became available (with $\tau \approx 1/\omega_p$). These could drive the plasma waves directly but had intensities large enough to lead to modification of the pulse itself. This is known as the Forced Laser Wakefield regime (F-LWFA), and was first observed in 2002 by Malka et al. [2]. In this regime the plasma wave focuses the laser pulse space, and compresses it in time.

The next important milestone in laser wake field acceleration was made possible with the development of Ti:Sapph lasers. Pulse lengths of $c\tau \simeq \lambda_p/2$, and powers exceeding 100 TW became available, , and it became possible to access the yet another scheme, some times referred to as the "bubble regime", where wave breaking could

be caused to occur in a single plasma cycle[7] . See Pukhov, 2002 [24]. In this highly non-linear regime, the plasma wave is reduced to a solitary cavity free of electrons, where the wave breaking, and self-trapping is localised in the back of the bubble-like structure. This leads to all the self-injected electrons experiencing the same accelerating field, and results in quasi-mono-energetic electron spectra.

A real revolution in Laser Wakefield Acceleration occurred in 2004 when the bubble regime was first accessed by three groups near simultaneously, Mangles [25], Geddes [26], and Faure [27]. Here utilising only moderate laser powers of tens of terawatts, quasi-monoengetic (with energy bandwidths of less than 3%), low divergence electron beams with energy of the order of 100 MeV, and charges of up to 100pC were first observed. These were a favourable contrast to the quasi-thermal electron spectra[8] which were typical of the previous Wakefield regimes.

Since then even higher energies have been reached in the F-LWFA regime. Expements include Mangles et al. 2006 [28], Hsieh et al. 2006 [29], Hidding et al. 2006 [30], Hosokai et al. 2003 [31], and Karsch et al. 2007 [32].

The first LWFA experiment to pass the GeV level was reported in 2006 by Leemans [33]. This utilised an external guiding structure to over come diffraction relaxing the power requirements of the beam.

Further Advanced Techniques in LWFA

There are a great number of avenues, not mentioned above, being pursued to improve one aspect of LWFA or another. Though of interest they do not fit neatly into the discussion above. Some of them are therefore mentioned in this section.

Laser stability, and laser focal spot quality is of great importance in laser wake field acceleration, and are examined in Mangles et al. 2006 [34], Mangles et al. 2007 [35], and Lindau et al. 2008 [36]. It is also the topic of the first experiment in this thesis.

One new technique to improve electron trapping. Thus improving the amount of charge accelerated, and working towards higher energy mono-energetic electron

[7] There is another scheme known as the "blow out regime" which is similar in concept to the "bubble regime". The "blow out regime" is described in Lu et al. 2006 [23]. The two scheme's are very similar but give slightly different scaling laws. The bubble regime claims applicability when $a_0 > 1$ where as the blow out does for $a_0 > 2$.

[8] Quasi-thermal Spectra: With the number of electrons decreasing with beam energy.

beams is " ionization induced trapping" [37]. See McGuffey [38], and Pak [39]. The idea behind this is to dope the plasma with heavy ions which will not release all their available electrons until the very peak of the driving laser pulse passes. The will cause electrons to be "born" right in the middle of the acceleration structure.

External wave guides (or light pipes) can be used to increase the interaction length, and help guild the laser pulse in the plasma lessening the requirements of self focusing. Work on this has been done utilising a number of diffrent external waveguilding structures. In 2001 Spence et al. 2001 [40] describes the first example of a gas-filled capillary discharge waveguide of the same type as used in the Leemans 2006 GeV paper [33]. Osterfhoff 2008 [41] demostrates a steady-state-flow gas cell. The grazing angle reflection capillary is shown in Courtois et al. 2001 [42]. The Heater Ignitor Technique is shown in Volfbeyn et al. 1999 [43], where a short (75 fs) ignitor pulse, and a long (160 ps) heater pulse are used to create a plasma channel through a combination of inverse Bremsstrahlung heating, and hydrodynamic shocks. The 'light pipe' guiding technique is given in Durfee 1993 [44], where a second co-propagating pulse is guided behind a first by the channel formed through hydrodynamic effects. A similar result is achieved in Krushelnick 1997 [45] through ponderomotive force effects.

Another ongoing avenue of research is the laser injection scheme first proposed by Umstadter in 1996 [46]. In this a second orthogonal laser beam locally alters the trajectory of some of the electrons in such a way as to allow them to become trapped in the plasma wave. However the second laser pulse's duration must be of the same order as the driving beam, and alignment is difficult. The advantage being however that the injection of electrons into the wake field can be stabilised, and controlled allowing for the accelerated electron's energy to be precisely tuned, at least in theory. Experiments utilising this technique include Faure et al. 2006 [47], Rechatin et al. 2009 [48], Davoine et al. 2009 [49], and Kotaki et al. 2009 [50].

Another method of injection is for electrons to be provided by an external linac. A theretical investigation is presented in Irman's 2007 paper [51], and this is the topic of the EuroLEAP Consortium (European Laser Electron controlled Acceleration in Plamas to GeV energy range)[9].

Multi-stage LWFA are also a way forward to longer interaction lengths, and higher energies, see Leeman et al. 2009 [52], not to mention being a possible route to

[9] http://www.laser-electron-acceleration-plasma.eu/

laboratory scale HEP experimentation.

Other Forms of Wake Field Acceleration

The relativistic electron plasma waves necessary to act as high energy particle acceleration structures can be set up other ways than through the use of lasers.

One obvious candidate to drive the plasma waves are other particle beams. Particle driven Wake Field Accelerators (PWFA) are an on going area of research. The physics is similar to that of a LWFA, and it is easy to envisage a plasma stage being added to a large conventional RF linac. Electron driven PWFA is decribed by Chen et al. [53]. Positively charged particle (positron or proton) driven PWFA is decribed by Caldwell et al. 2009 [54], and even Neutrino driven wake field accelertion has been proposed see Bingham et al. 1994 [55].

In electron beam driven PWFA energy doubling of the energy of some electrons has been seen, Blumenfeld 2007 [56], where electrons from a 48 GeV drive beam have been accelerated to $>$ 80 GeV. Though these energy spectra are quasi-thermal. The PWFA acts to increase the energy of some of the beams particles while lowering the total number of accelerated particles. It has exciting possibilities for the future HEP applications[10].

X-Ray Production: The WakeField Wiggler

In a similar way to high energy photons (hard X-rays) being produced in circular conventional RF accelerators[11] due to the acceleration the high energy particles experience as they follow the curve of the machine, the electrons accelerated in LWFA can emit X-rays as they oscillate inside the accelerating bubble. Furthermore this oscillation can more closely resemble that found in a magnetic insertion device[12]. This is generally known as betatron radiation, and was first observed experimentally by Rousse in 2004 [57].

[10] Current work at SLAC (The Stanford linear accelerator), and ongoing research as part of CERN is directed to this end. See FACET (Facilities for Accelerator Science, and Experimental Test Beams at SLAC), http://facet.slac.stanford.edu/ .

[11] Synchrotrons.

[12] A magnetic insertion device (undulator or wiggler) consists of rows of oppositely aligned alternately poled permanent magnets which electron beams are inserted between. This make the incoming electrons wiggle slightly as they pass thus emitting collimated beams of synchrotron radiation. The

The Wake Field Wiggler is theoretically treated in Kostyukov et al. 2003 [58], Kostyukov et al. 2004 [59], Kiselev et al. 2004 [60], and Thomas et al. 2009 [61]. Furthermore Thomas et al. 2010 [62] is of interest to the experimental work in this report as it is tested in section 4.2.

Experiments into wakefield wiggler radiation include Phuoc et al. 2005 [63], Albert et al. 2008 [64], and Albert et al. 2009 [65]. High quality x-ray production has been seen in Kniep et al. 2008 [66], Mangles et al. 2009 [67], and Kneip et al. [68], and Kneip et al. 2011 [69] where I am also a co-author.

Related to this field Phuoc et al. 2006 [70], and Phuoc et al. 2008 [71] shows imaging of electron orbits in plasma cavities (or at least the electron orbits are deduced from the emitted radiation). It is reasonable to assume that the radiation pulse length must be ultra short, similar to the bunch duration of the electron beam. In Phouc et al. 2007 [72] the ultra short nature of the radiation is verified. Finally in Khachatryan's 2008 paper [73] it is found that at wavelengths longer than the electron bunch length, the radiation is coherent.

X-ray Production in Other Related Areas

In this section a review of some related radiation production techniques will be presented. Techniques which are either closely related physical systems or employ similar experimental techniques.

The following papers show betatron radiation generated from PWFA's;Wang et al. 2002 [74], and Clayton et al. 2002 [75]. The physics here is very similar to betatron emission in LWFA however the inserted electron beam provided the drive for the plasma wave, and the plasma channel then acts as an undulator. Again here the high field gradients available in plasmas can be an advantage.

When beams of relativistic high energy electrons are inserted into a conventional undulators as they emit radiation they act in a very similar way to a laser medium. This has lead to the term Free Electron Laser (FEL). The idea was first proposed in 1976 by Madey et al. [76]. Conventional accelerators such as SLAC[13] are now

radiation will be at wavelength

$$\lambda_\beta = \frac{\lambda_\mu}{2\gamma^2}$$

where γ is the relativistic factor of the electrons, and λ_μ the periodic spacing of the magnets.

[13]The Stanford Liner Accelerator.

being used for this purpose to provide coherent X-ray radiation (X-FELs), but are expensive to build, and maintain. Other FELs include PETRA III, and FLASH.

Work is also being done on inserting the electrons produced from a LWFA into a conventional magnetic undulator. This has the potential to provide table top X-FELs. Progress in this area is reported in Gruner et al. 2007 [77], Schlenvoig et al. 2008 [78], Fuchs et al. 2009 [79], and is the aim of the Alpha-X project[14].

[14] http://phys.strath.ac.uk/alpha-x/

Chapter 2

Theory.

2.1 High Intensity Short Pulse Laser Concepts.

In this chapter I will introduce some of the key concepts used throughout this thesis.

2.1.1 Rayleigh Range

The Rayleigh Range (or length), denoted with z_R, is a useful parameter in defining the length of a laser plasma interaction. It is defined as the distance along the direction of propagation of a beam from its narrowest waist (or focus) to the place where its area of cross section is doubled. For a Gaussian beam this corresponds to

$$z_R = \frac{\pi w_0^2}{\lambda_L} \tag{2.1}$$

where w_0 is the radius of focus. See figure 2.1.

2.1.2 The laser strength parameter a_0

An important parameter in the discussion of intense laser-plasma interactions is the laser strength parameter a_0. It is defined as the peak amplitude of the normalized vector potential of the the laser field.

$$\vec{\mathbf{a}} = \frac{e\vec{\mathbf{A}}}{m_e c^2} \tag{2.2}$$

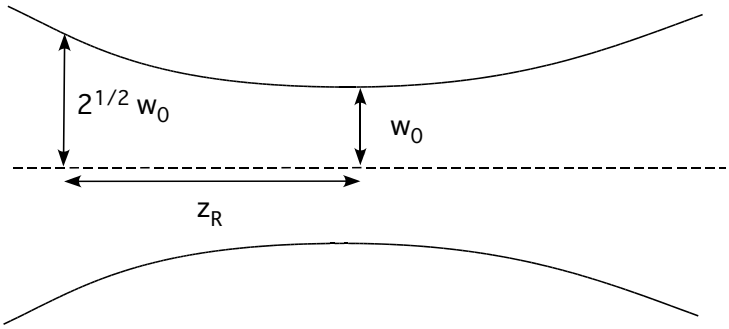

Figure 2.1: Relevant lengths in the definition of the Rayleigh length.

Assuming a Gaussian radial profile[1], the laser strength parameter is related to the peak laser intensity by

$$I_0 = \frac{\pi c}{2}\left(\frac{m_e c^2 a_0}{e\lambda_L}\right)^2 \tag{2.3}$$

and to the laser power,

$$P = \frac{\pi w_0^2 I_0}{2} \tag{2.4}$$

The peak electric field amplitude due to the laser is also given by [1],

$$E_L = \frac{m_e c \omega_L a_0}{e} \tag{2.5}$$

Physically if $a_0 > 1$ then then it can cause electrons to move relativistically. This corresponds, for a laser wavelength of about 1 μm, $I > 10^{18}$ W/cm^3.

2.1.3 The size of a diffraction limited focal spot.

In the case of a lens or parabolic mirror the F-number f_n is given by the focal length divided by the width of the entrance pupil. The diameter of the diffraction limited spot $2w_0$ is then given by

$$2w_0 = 2.44\frac{f_n}{\lambda_L} \tag{2.6}$$

[1] $\overrightarrow{\mathbf{a}} = a_0 exp(-r^2/w_0^2)\cos(k_L z - \omega_L t)\widehat{\mathbf{i}}$

2.2 Concepts of Plasma Physics.

Here subscripts p and L will be used to distinguish values associated with the plasma wave and electromagnetic wave in the plasma accordingly. The exception to this will be ω_w which will refer to the frequency of the plasma wave opposed to the frequency of the plasma (ω_p).

2.2.1 Debye length.

Plasma have the property of masking charges present in them. As for any single charge, the ions and electrons given sufficient time are able to move to obscure it. In the treatment of this property it is useful to define a convenient length known as the Deybye length above which this screening takes place (see Appendix B for derivation and discussion).

$$\lambda_D = \left(\frac{\epsilon_0 k_B T_e}{n_e e^2} \right)^{1/2} \tag{2.7}$$

Thus for hotter plasmas the shielding is greater and the λ_D greater and for more dense plasmas the shielding is less. [2]

2.2.2 Plasma frequency

Another extremely important property of a given plasma is its natural frequency ω_p which is the frequency the electrons will oscillate at, if perturbed from quasi-neutral equilibrium and is: [3]

$$\omega_p = \left(\frac{e^2 n_e}{\epsilon_0 m_e} \right)^{1/2} \tag{2.8}$$

A full derivation of this is given in Appendix C.

[2] So

$$\lambda_D[\mathrm{m}] = 7430 \left(\frac{K_B T[\mathrm{eV}]}{n_e[m^{-3}]} \right)^{1/2}$$

or

$$\lambda_D[\mathrm{cm}] = 2.35 \times 10^{-8} \left(\frac{K_B T[\mathrm{eV}]}{n_e 10^{-21}[\mathrm{cm}^{-3}]} \right)^{1/2}$$

[3]

$$\omega_p[rad/s] \approx 5.64 \times 10^4 n_e^{1/2}$$

2.2.3 Dispersion relation of an Electromagnetic wave in Plasma

Dispersion relation of an Electromagnetic wave in Vacuum

If we consider a plane electromagnetic wave propagating in the x direction in a vacuum with no external electric or magnetic Fields. The relevant Maxwell equations are Faraday's Law A.3 and Ampere's Law A.4:

$$-\nabla \times \vec{\mathbf{E}} = \frac{\partial \vec{\mathbf{B}}}{\partial t} \tag{2.9}$$

$$c^2 \nabla \times \vec{\mathbf{B}} = \frac{\partial \vec{\mathbf{E}}}{\partial t} \tag{2.10}$$

Taking the curl of Ampere's law and the time derivative of Faraday's law:

$$-\nabla \times \frac{\partial \vec{\mathbf{E}}}{\partial t} = \frac{\partial^2 \vec{\mathbf{B}}}{\partial t^2} \tag{2.11}$$

$$c^2 \nabla \times (\nabla \times \vec{\mathbf{B}}) = \nabla \times \frac{\partial \vec{\mathbf{E}}}{\partial t} \tag{2.12}$$

Equating:

$$-c^2 \nabla \times (\nabla \times \vec{\mathbf{B}}) = \frac{\partial^2 \vec{\mathbf{B}}}{\partial t^2} \tag{2.13}$$

Now assuming the plane waves are varying as $e^{i(\vec{\mathbf{k}}\vec{\mathbf{r}} - \omega t)}$ and using identity A.13. We have:

$$\omega^2 \vec{\mathbf{B}} = -c^2 \vec{\mathbf{k}} \times (\vec{\mathbf{k}} \times \vec{\mathbf{B}}) = -c^2 \left(\vec{\mathbf{k}} (\vec{\mathbf{k}} \cdot \vec{\mathbf{B}}) - \vec{\mathbf{k}}^2 \vec{\mathbf{B}} \right) \tag{2.14}$$

From Gauss's Law of Magitusum we have:

$$\vec{\mathbf{k}} \cdot \vec{\mathbf{B}} = -i \nabla \cdot \vec{\mathbf{B}} = 0 \tag{2.15}$$

This leads to:

$$\omega^2 = k^2 c^2 \tag{2.16}$$

Which is the dispersion relation for a EM wave in vacuum. From Appendix D the phase velocity and the group velocity are thus both equal to the speed of light as expected.

$$c = \frac{\omega}{k} = v_\phi = \frac{d\omega}{dk} = v_g \tag{2.17}$$

Dispersion relation of an Electromagnetic wave in Plasma

Now instead conceder an EM wave in a plasma. The Equation of Amperes law will gain a $\vec{\mathbf{J}}_1/\epsilon_0$ to account for charged particle motions. I will use the sub script 0 and 1 to represent particles at, and moved from, their equilibrium positions respectively. So 2.10 becomes:

$$c^2\nabla \times \vec{\mathbf{B}}_1 = \frac{\vec{\mathbf{J}}_1}{\epsilon_0} + \frac{\partial \vec{\mathbf{E}}_1}{\partial t} \tag{2.18}$$

Taking the time derivative and curl on opposite equations this time in the same way as before:

$$c^2\nabla \times \dot{\vec{\mathbf{B}}}_1 = \frac{\partial \vec{\mathbf{J}}_1}{\epsilon_0 \partial t} + \ddot{\vec{\mathbf{E}}}_1 \tag{2.19}$$

$$\nabla \times (\nabla \times \vec{\mathbf{E}}_1) = -\nabla \times \dot{\vec{\mathbf{B}}}_1 \tag{2.20}$$

Eliminating $\nabla \times \dot{\vec{\mathbf{B}}}_1$, using A.13 and assuming $e^{i(\vec{\mathbf{k}}\,\vec{\mathbf{r}}-\omega t)}$ dependence we arrive at:

$$-\vec{\mathbf{k}}(\vec{\mathbf{k}} \cdot \vec{\mathbf{E}}_1) + k^2\vec{\mathbf{E}}_1 = \frac{i\omega}{\epsilon_0 c^2}\vec{\mathbf{J}}_1 + \frac{\omega^2}{c^2}\vec{\mathbf{E}}_1 \tag{2.21}$$

Transverse waves mean $\vec{\mathbf{k}} \cdot \vec{\mathbf{E}}_1 = 0$. As $\vec{\mathbf{E}}_1$ is $\perp$ to $\vec{\mathbf{k}}$.

$$(\omega^2 - c^2k^2)\vec{\mathbf{E}}_1 = -i\omega\frac{\vec{\mathbf{J}}_1}{\epsilon_0} \tag{2.22}$$

If we consider light waves or higher frequency waves ions can be considered fixed so $\vec{\mathbf{J}}_1$ comes only from electrons. $\vec{\mathbf{J}}_1 = -n_0 e\vec{\mathbf{v}}_{e1}$ where $\vec{\mathbf{v}}_{e1}$ has the usual $e^{i(\vec{\mathbf{k}}\,\vec{\mathbf{r}}-\omega t)}$ dependence. Now let us consider the temperature of the electrons ($k_B T_e$) to be unimportant. We may then used the linearised equation of electron motion derived while considering the plasma frequency C.9:

$$m_e\frac{\partial \vec{\mathbf{v}}_{e1}}{\partial t} = -e\vec{\mathbf{E}}_1 \quad \Rightarrow \quad \vec{\mathbf{v}}_{e1} = \frac{e\vec{\mathbf{E}}_1}{im_e\omega} \tag{2.23}$$

So substituting in:

$$(\omega^2 - c^2k^2)\vec{\mathbf{E}}_1 = \frac{n_0e^2}{\epsilon_0 m_e}\vec{\mathbf{E}}_1 = \omega_p^2\vec{\mathbf{E}}_1 \tag{2.24}$$

So finally we arrive at the dispersion relation which is:

$$\omega_L^2 = \omega_p^2 + c^2k_L^2 \tag{2.25}$$

So

$$v_{\phi L}^2 = \frac{\omega_L^2}{k_L^2} = \frac{\omega_p}{k_L} + c^2 > c^2 \quad , \quad v_{gL} = \frac{d\omega_L}{dk_L} = \frac{c^2 k_L}{\omega_L} = \frac{c^2}{v_{\phi L}} < c \tag{2.26}$$

Which means that the phase velocity in the plasma is likely to be greater than c. However causality is preserved due to the group velocity necessary being less than c, and it is this that would carry any information.

2.2.4 Dispersion relation of an Electron Plasma Wave.

Electrons streaming into adjacent layers of plasma with their thermal velocities will carry information about the oscillating region. If the Equation of Motion is (from equation C.2 in appendix) :

$$m_e n_e \left(\frac{\partial \overrightarrow{\mathbf{v}}_e}{\partial t} + (\overrightarrow{\mathbf{v}}_e \cdot \nabla) \overrightarrow{\mathbf{v}}_e \right) = -e n_e \overrightarrow{\mathbf{E}} \tag{2.27}$$

Then we must add term $-\nabla p_e$ to the EOM to account for this. In one dimension it can be argued that:

$$-\nabla p_e = 3k_B T_e \nabla n_e = 3k_B T_e \nabla (n_0 + n_1) = 3k_B T_e \frac{\partial n_1}{\partial x} \widehat{\mathbf{x}} \tag{2.28}$$

So the linearized equation of motion is, where some terms have been neglected:

$$m_e n_0 \frac{\partial v_1}{\partial t} = -e n_0 E_1 - 3k_B T_e \frac{\partial n_1}{\partial x} \tag{2.29}$$

Now assuming wave like behaviour, (So $E_1 = E_m e^{i(xk - \omega t)}$), we have:

$$-i\omega v_1 m_e n_0 = -e n_0 E_1 - 3k_B T_e i k n_1 \tag{2.30}$$

Using,

$$-i\omega n_1 = -n_0 i k v_1 \quad \text{and,} \quad ik\epsilon_0 E_1 = -e n_1 \tag{2.31}$$

So,

$$-i\omega v_1 m_e n_0 = \left[e n_0 \left(\frac{-e}{ik\epsilon_0} \right) + 3k_b T_e ik \right] \frac{n_0 ik}{i\omega} v_1 \tag{2.32}$$

$$\omega^2 v_1 = \left(\frac{n_0 e^2}{\epsilon_0 m} + \frac{3k_B T_e}{m} k^2 \right) v_1 \tag{2.33}$$

So we end up with what is sometimes referred to as the Bohm-Gross Dispersion relation for an electron plasma wave:

$$\omega_w^2 = \omega_p^2 + \frac{3}{2}k_p^2 v_{th}^2 \tag{2.34}$$

Where $v_{th}^2 = 2k_B T_e/m$ is the thermal velocity of the electrons, and subscripts have been added to avoid confusion[4]. The group and phase velocities are respectively then:

$$\text{Using:} \quad 2\omega_w d\omega_w = \frac{3}{2}v_{th}^2 2k_p dk_p \tag{2.35}$$

$$v_{gp} = \frac{d\omega_w}{dk_p} = \frac{3}{2}\frac{k_p}{\omega_w}v_{th}^2 = \frac{3}{2}\frac{v_{th}}{v_{\phi p}} \tag{2.36}$$

So if the plasma's temprature (T_e) is negligible then so will be the group velocity of the electron plasma wave (v_{gp}).

$$v_{\phi p} = \frac{\omega_w}{k_p} = \sqrt{\frac{\omega_p^2}{k_p^2} + \frac{3}{2}v_{th}^2} \tag{2.37}$$

So ($k_p \to \infty, \quad v_{\phi p} \to \frac{3}{2}v_{th}^2$), for large wave numbers the phase velocity only depends on the plasma temperature.

2.2.5 Critical density

Another important concept to do with plasmas is the critical density for a given electromagnetic wave with a given frequency in vacuum ω_0. At densities above this and electromagnetic wave will not propagate into a plasma and will be completely masked by electrons moving to obscure it. As we will see the critical density for a plasma turns out to be when the $\omega_p = \omega_0$. This means the natural oscillations of the plasma (derived in Appendix C) are faster than that of the EM waves and so can mask it. However this can also be shown from the dispersion relation 2.25.

$$\omega_L^2 = \frac{n_0 e^2}{\epsilon_0 m_e} + c^2 k_L^2 \tag{2.38}$$

As the wavenumber, k of the radiation will change on entering the plasma but the frequency (ω_0) will not (So $\omega_L = \omega_0$), we arrive at

$$k_L^2 = \frac{\omega_0^2}{c^2} - \frac{n_0 e^2}{\epsilon_0 m_e c^2} \tag{2.39}$$

[4] As mentioned before here subscripts p and L will be used to distinguish values associated with the plasma wave and electromagnetic wave in the plasma accordingly. The exception to this will be ω_w which will refer to the frequency of the plasma wave opposed to the frequency of the plasma (ω_p).

now $k_L^2 > 0$ for it to have any physical meaning. So

$$\frac{\omega_0^2}{c^2} > \frac{n_0 e^2}{\epsilon_0 m_e c^2} \tag{2.40}$$

Thus $\omega_p < \omega_0$ and

$$n_e < \frac{\omega_0^2 m_e \epsilon_0}{e^2} \equiv n_c \tag{2.41}$$

Which is the condition for a electromagnetic wave to propagate in a plasma. Where n_c is known as the critical density [5].

[5]

$$n_c[cm^{-3}] = \frac{1.113 \times 10^{21}}{(\lambda[\mu m])^2}$$

2.3 Concepts of Laser plasma interactions.

2.3.1 Wave Interactions Inside a Laser Wakefield Particle Accelerator

In the case of a Laser Wakefield Particle Accelerator (LWFA). The electromagnetic wave from a short laser pulse is focused into a plasma and used to excite an electron plasma wave. This causes the phase velocity of the plasma wave to become equal to the group velocity of the laser wave.

$$v_{\phi p} = v_{gL}$$

Lorentz Factor Associated with the Phase Velocity of a LWFA's Plasma wave.

From section 2.2.4 we know that the dispersion relation for a electron plasma wave is:

$$\omega_w^2 = \omega_p^2 + \frac{3}{2}k_p^2\frac{v_{th}^2}{v_{\phi p}} \tag{2.42}$$

As usual here subscripts p and L will be used to distinguish values associated with the plasma wave and electromagnetic wave in the plasma accordingly and the exception to this will be ω_w which will refer to the frequency of the plasma wave opposed to the frequency of the plasma (ω_p). From 2.25 we have the dispersion relation of an electromagnetic wave being:

$$\omega_L^2 = \omega_p^2 + k_L^2c^2 \tag{2.43}$$

This gives the group and phase velocities as follows:

$$v_{gL} = \frac{c^2k_L}{\omega_L} = \frac{c^2}{v_{\phi L}} \quad , \quad v_{gp} = \frac{3}{2}\frac{k_p}{\omega_w}v_{th}^2 = \frac{3}{2}\frac{v_{th}^2}{v_{\phi p}} \tag{2.44}$$

$$v_{\phi L} = \sqrt{\frac{\omega_p^2}{k_L^2} + c^2} \quad , \quad v_{\phi p} = \sqrt{\frac{\omega_p^2}{k_p^2} + \frac{3}{2}v_{th}^2} \tag{2.45}$$

Now if we consider the ratio of the critical frequency to the plasma frequency we have the following relation:

$$\frac{\omega_p^2}{\omega_L^2} = \frac{n_e e^2}{\epsilon_0 m_e}/\frac{n_c e^2}{\epsilon_0 m_e} = \frac{n_e}{n_c} \tag{2.46}$$

This result will come in useful later. From the relations above we can also deduce:

$$k_L^2 = \frac{\omega_L^2 - \omega_p^2}{c^2} \tag{2.47}$$

So again from above we may write down:

$$v_{\phi L}^2 = \frac{\omega_p^2 c^2}{\omega_L^2 - \omega_p^2} + c^2 \tag{2.48}$$

$$\frac{v_{\phi L}^2}{c^2} = \frac{\omega_L^2}{\omega_L^2 - \omega_p^2} \tag{2.49}$$

$$= \frac{1}{1 - \omega_p^2/\omega_L^2} \tag{2.50}$$

From equation 2.46 we have,

$$\frac{v_{\phi L}}{c} = \left(1 - \frac{\omega_p^2}{\omega_L^2}\right)^{-1/2} = \left(1 - \frac{n_e}{n_c}\right)^{-1/2} \tag{2.51}$$

From our expression for v_{gL} above, we have;

$$\frac{v_{gL}}{c} = \frac{c}{v_{\phi L}} = \left(1 - \frac{n_e}{n_c}\right)^{1/2} \tag{2.52}$$

Now by definition the Lorentz factor associated with the phase velocity of a LWFA's plasma wave ($\gamma_{\phi p}$) is given by:

$$\gamma_{\phi p} = \left(1 - \frac{v_{\phi p}^2}{c^2}\right)^{-1/2} \tag{2.53}$$

Now as also has been dissussed in a LWFA $v_{\phi p} = v_{gL}$ so:

$$\gamma_{\phi p} = \left(1 - \frac{v_{gL}^2}{c^2}\right)^{-1/2} = \left(1 - \left(1 - \frac{n_e}{n_c}\right)\right)^{1/2} \tag{2.54}$$

where equation 2.52 has been used. Thus we obtain:

$$\gamma_{\phi p} = \frac{\sqrt{n_c}}{\sqrt{n_e}} = \frac{\omega_L}{\omega_p} \tag{2.55}$$

which is a very elegant result indeed.

The wavelength of a LWFA's Plasma wave.

Starting from the group velocity of the laser pulse v_{gL} and combining with equation 2.46 for the wave number k_L we arrive at:

$$v_{gL}^2 = c^2(1 - \frac{\omega_p^2}{\omega_L^2}) \tag{2.56}$$

Now as discussed before equating $v_{\phi p} = v_{gL}$ and squaring both sides we have,

$$\frac{\omega_p^2}{k_p^2} + \frac{3}{2}v_{th}^2 = c^2(1 - \frac{\omega_p^2}{\omega_L^2}) \tag{2.57}$$

The quickly rearranges, noting that $k_p = 2\pi/\lambda_p$,

$$\frac{1}{k_p^2} = \frac{c^2}{\omega_p^2} - \frac{c^2}{\omega_L^2} - \frac{3}{2}\frac{v_{th}^2}{\omega_p^2} = \frac{\lambda_p^2}{4\pi^2} \tag{2.58}$$

This is a exact equation for the wavelength of the plasma wave. However it is common to simply this equation. As $\omega_L > \omega_p$ for laser propgation to occur the second term in the middle can be neglected. Also in the systems we are considering $v_{th}^2 << c^2$ and so can also be ignored. This yields the well known result:

$$\lambda_p = \frac{2\pi c}{\omega_p} \tag{2.59}$$

2.3.2 Rigorous Mathematical Treatment of Laser Propagation in Underdense Plasma

In this subsection the relevant mathematics for a laser wave propagating in an under dense plasma causing a plasma wave to develop will be explored, resulting in TRANSVERSE and LONGITUDINAL WAVE EQUATIONS, as will expressions for the magnitude of the electric field and electron density as a functions of time. This leads neatly to the derivation of the 'well known' cold wave-breaking limit in section 2.3.3. This treatment expands upon and follows Gibbon 2005 [80] however in SI units.

To begin let us right down the Lorentz equation of motion for the electrons[6](see A.7) and Maxwell equations (see A.1) for this system, noting we have no external magnetic field:

$$\frac{\partial \overrightarrow{\mathbf{p}}}{\partial t} = (\overrightarrow{\mathbf{v}} \cdot \nabla)\overrightarrow{\mathbf{p}} = -e(\overrightarrow{\mathbf{E}} + \overrightarrow{\mathbf{v}} \times \overrightarrow{\mathbf{B}}) \tag{2.60}$$

Gauss's Law:

$$\nabla \cdot \overrightarrow{\mathbf{E}} = \frac{e}{\epsilon_0}(n_0 - n_e) \tag{2.61}$$

Faraday's Law:

$$\nabla \times \overrightarrow{\mathbf{E}} = -\frac{\partial \overrightarrow{\mathbf{B}}}{\partial t} \tag{2.62}$$

Gauss's Law of Magnesium.

$$\nabla \cdot \overrightarrow{\mathbf{B}} = 0 \tag{2.63}$$

Ampére's Law:

$$\nabla \times \overrightarrow{\mathbf{B}} = -en_e \overrightarrow{\mathbf{v}} \mu_0 + \frac{1}{c^2} \frac{\partial E}{\partial t} \tag{2.64}$$

Where $\overrightarrow{\mathbf{v}}$ is the velocity of an electron at this position, n_e the electron density and n_0 the initial plasma electron density. Now making a quite large[7] assumption that all the relevant quantities[8] have an oscillating time spatial dependence of the form $f(\omega t - \overrightarrow{\mathbf{k}} \cdot \overrightarrow{\mathbf{r}})$, but for ease using $f(\tau)$ where,

$$\tau = t - \widehat{\mathbf{i}} \cdot \frac{\overrightarrow{\mathbf{r}}}{v_\phi} = \frac{1}{\omega}(\omega t - \overrightarrow{\mathbf{k}} \cdot \overrightarrow{\mathbf{r}})$$

$\overrightarrow{\mathbf{k}}$ and $\widehat{\mathbf{i}}$ are in the direction of propagation of our laser, and v_ϕ is the phase velocity (see D) of the electromagnetic wave in the plasma ($v_{\phi L}$) (given by 2.26) but here the subscript L will be omitted. The following substitutions for derivatives are therefore possible with this assumption [9]

$$\frac{\partial}{\partial t} \Rightarrow \frac{\partial}{\partial t} \quad , \quad \nabla\cdot \Rightarrow -\frac{\widehat{\mathbf{i}}}{v_\phi}\frac{\partial}{\partial \tau} \quad , \quad \nabla\times \Rightarrow -\frac{\widehat{\mathbf{i}}}{v_\phi}\frac{\partial}{\partial \tau}\times$$

Then doing some substitutions, integration and replacing partial derivatives with total derivatives the equations become:

$$\left(\frac{\widehat{\mathbf{i}} \cdot \overrightarrow{\mathbf{v}}}{v_\phi} - 1\right) \frac{d\overrightarrow{\mathbf{p}}}{d\tau} = e(\overrightarrow{\mathbf{E}} + \overrightarrow{\mathbf{v}} \times \overrightarrow{\mathbf{B}}) \tag{2.65}$$

$$-\widehat{\mathbf{i}} \cdot \frac{d\overrightarrow{\mathbf{E}}}{d\tau} = \frac{ev_\phi}{\epsilon_0}(n_0 - n_e) \tag{2.66}$$

$$\overrightarrow{\mathbf{B}} = \frac{1}{v_\phi}\widehat{\mathbf{i}} \times \overrightarrow{\mathbf{E}} + \overrightarrow{\mathbf{B}}_0 \tag{2.67}$$

[6] Here using the convective derivative A.3

[7] A quite large but well founded assumption. Given that we are looking for wave like behaviour.

[8] Such as n_e, $\overrightarrow{\mathbf{E}}$ and $\overrightarrow{\mathbf{B}}$

[9] It should be pointed out that $v_{\phi p}$ not $v_{\phi L}$ should be used if the operators act on an non electromagnetic quantity.

$$\widehat{\mathbf{i}} \cdot \frac{d\overrightarrow{\mathbf{B}}}{d\tau} = 0 \tag{2.68}$$

$$-\widehat{\mathbf{i}} \times \frac{d\overrightarrow{\mathbf{B}}}{d\tau} = -ev_\phi n_e \overrightarrow{\mathbf{v}}\mu_0 + \frac{v_\phi}{c^2}\frac{d\overrightarrow{\mathbf{E}}}{d\tau} \tag{2.69}$$

The term $\overrightarrow{\mathbf{B}}_0$ which comes about as a constant of integration represents an external magnetic field which here is of course zero. Taking the dot product of our equation for Gauss' Law 2.69 with $\widehat{\mathbf{i}}$,

$$-\widehat{\mathbf{i}}\left(\widehat{\mathbf{i}} \times \frac{d\overrightarrow{\mathbf{B}}}{d\tau}\right) = -ev_\phi n_e \widehat{\mathbf{i}} \cdot \overrightarrow{\mathbf{v}}\mu_0 + \frac{v_\phi}{c^2}\overrightarrow{\mathbf{i}} \cdot \frac{d\overrightarrow{\mathbf{E}}}{d\tau}$$

$$0 = -ev_\phi n_e \widehat{\mathbf{i}} \cdot \overrightarrow{\mathbf{v}}\mu_0 - \frac{v_\phi}{c^2}\frac{ev_\phi}{\epsilon_0}(n_0 - n_e)$$

substituting with 2.66. Thus rearranging we get:

$$n_e = \frac{v_\phi n_0}{v_\phi - \overrightarrow{\mathbf{i}} \cdot \overrightarrow{\mathbf{v}}} \tag{2.70}$$

which is an important expression for n_e. Like wise taking the cross product of the equation of motion 2.65,

$$\left(\frac{\widehat{\mathbf{i}} \cdot \overrightarrow{\mathbf{v}}}{v_\phi} - 1\right)\widehat{\mathbf{i}} \times \frac{d\overrightarrow{\mathbf{p}}}{d\tau} = e\widehat{\mathbf{i}} \times \overrightarrow{\mathbf{E}} + e\widehat{\mathbf{i}} \times (\overrightarrow{\mathbf{v}} \times \overrightarrow{\mathbf{B}})$$

Substituting in equation 2.67, and using identity A.14,

$$\left(\frac{\widehat{\mathbf{i}} \cdot \overrightarrow{\mathbf{v}}}{v_\phi} - 1\right)\widehat{\mathbf{i}} \times \frac{d\overrightarrow{\mathbf{p}}}{d\tau} = ev_\phi \overrightarrow{\mathbf{B}} + e[0 - (\widehat{\mathbf{i}} \cdot \overrightarrow{\mathbf{v}})\overrightarrow{\mathbf{B}}]$$

$$= -e\overrightarrow{\mathbf{B}}v_\phi\left(\frac{\widehat{\mathbf{i}} \cdot \overrightarrow{\mathbf{v}}}{v_\phi} - 1\right)$$

$$\overrightarrow{\mathbf{B}} = -\frac{1}{ev_\phi}\widehat{\mathbf{i}} \times \frac{d\overrightarrow{\mathbf{p}}}{d\tau} \tag{2.71}$$

This is a very useful expression for the magnitude of the magnetic field in terms of momentum. Taking $\widehat{\mathbf{i}}\times$ Ampére's Law (2.69) and using identity A.14 then substituting in 2.67,

$$\widehat{\mathbf{i}} \times \left(\widehat{\mathbf{i}} \times \frac{d\overrightarrow{\mathbf{B}}}{d\tau}\right) = -ev_\phi n_e \widehat{\mathbf{i}} \times \overrightarrow{\mathbf{v}}\mu_0 + \frac{v_\phi}{c^2}\widehat{\mathbf{i}} \times \frac{d\overrightarrow{\mathbf{E}}}{d\tau}$$

$$-(i \cdot \frac{d\overrightarrow{\mathbf{B}}}{d\tau})\widehat{\mathbf{i}} + (\widehat{\mathbf{i}} \cdot \widehat{\mathbf{i}})\frac{d\overrightarrow{\mathbf{B}}}{d\tau} = -ev_\phi n_e \widehat{\mathbf{i}} \times \overrightarrow{\mathbf{v}}\mu_0 + \frac{v_\phi^2}{c^2}\overrightarrow{\mathbf{B}}$$

then noting 2.68 gives $(i \cdot d\overrightarrow{\mathbf{B}}/d\tau) = 0$ and rearranging gives:

$$\frac{d\overrightarrow{\mathbf{B}}}{d\tau} = en_e c\mu_0 \frac{\beta_\phi}{\beta_\phi^2 - 1}\widehat{\mathbf{i}} \times \overrightarrow{\mathbf{v}} \tag{2.72}$$

where $\beta_\phi = v_\phi/c$. Then taking $d/d\tau$ of 2.71 and subtracting 2.72 we get:

$$\frac{d\overrightarrow{\mathbf{B}}}{d\tau} - \frac{d\overrightarrow{\mathbf{B}}}{d\tau} = \frac{d}{d\tau}\frac{1}{ev_\phi}\widehat{\mathbf{i}} \times \frac{d\overrightarrow{\mathbf{p}}}{d\tau} + en_e c\mu_0 \frac{\beta_\phi}{\beta_\phi^2 - 1}\widehat{\mathbf{i}} \times \overrightarrow{\mathbf{v}}$$

which rearranging[10] becomes the TRANSVERSE WAVE EQUATION:

$$\widehat{\mathbf{i}} \times \frac{d^2\overrightarrow{\mathbf{p}}}{d\tau^2} + \frac{e^2 n_e}{\epsilon_0}\frac{\beta_\phi^2}{\beta_\phi^2 - 1}\widehat{\mathbf{i}} \times \overrightarrow{\mathbf{v}} = 0 \tag{2.73}$$

Taking the $\widehat{\mathbf{i}}\cdot$ of the equation of motion 2.65, then differentiating we have:

$$\frac{d}{d\tau}\left[\left(\frac{\widehat{\mathbf{i}} \cdot \overrightarrow{\mathbf{v}}}{v_\phi} - 1\right)\widehat{\mathbf{i}} \cdot \frac{d\overrightarrow{\mathbf{p}}}{d\tau}\right] = e\,\widehat{\mathbf{i}} \cdot \frac{d\overrightarrow{\mathbf{E}}}{d\tau} + e\frac{d}{d\tau}\left[\widehat{\mathbf{i}} \cdot \overrightarrow{\mathbf{v}} \times \overrightarrow{\mathbf{B}}\right]$$

Substituting in using Gauss' Law 2.66 and our expression for $\overrightarrow{\mathbf{B}}$ 2.71 the right hand side becomes:

$$\begin{aligned}
&= -\frac{e^2 v_\phi}{\epsilon_0}(n_0 - n_e) + e\frac{d}{d\tau}\left[\widehat{\mathbf{i}} \cdot \overrightarrow{\mathbf{v}} \times \left(-\frac{1}{ev_\phi}\widehat{\mathbf{i}} \times \frac{d\overrightarrow{\mathbf{p}}}{d\tau}\right)\right] \\
&= -\frac{e^2 v_\phi}{\epsilon_0}(n_0 - \frac{v_\phi n_0}{v_\phi - \overrightarrow{\mathbf{i}} \cdot \overrightarrow{\mathbf{v}}}) - \frac{1}{v_\phi}\frac{d}{d\tau}\left[\widehat{\mathbf{i}}\left((\overrightarrow{\mathbf{v}} \cdot \frac{d\overrightarrow{\mathbf{P}}}{d\tau})\widehat{\mathbf{i}} - (\overrightarrow{\mathbf{v}} \cdot \widehat{\mathbf{i}})\frac{d\overrightarrow{\mathbf{P}}}{d\tau}\right)\right] \\
&= \frac{e^2 v_\phi n_0\left(\widehat{\mathbf{i}} \cdot \overrightarrow{\mathbf{v}}\right)}{\epsilon_0\left(v_\phi - \widehat{\mathbf{i}} \cdot \overrightarrow{\mathbf{v}}\right)} - \frac{1}{v_\phi}\frac{d}{d\tau}\left[\overrightarrow{\mathbf{v}} \cdot \frac{d\overrightarrow{\mathbf{P}}}{d\tau} - (\overrightarrow{\mathbf{v}} \cdot \widehat{\mathbf{i}})\left(\widehat{\mathbf{i}} \cdot \frac{d\overrightarrow{\mathbf{P}}}{d\tau}\right)\right]
\end{aligned}$$

where identity A.14 and our expression for n_e 2.70 have been used as required. The LONGITUDINAL WAVE EQUATION is then:

$$\frac{d}{d\tau}\left[\left(\frac{\widehat{\mathbf{i}} \cdot \overrightarrow{\mathbf{v}}}{v_\phi} - 1\right)\widehat{\mathbf{i}} \cdot \frac{d\overrightarrow{\mathbf{p}}}{d\tau}\right] = \frac{e^2 v_\phi n_0\left(\widehat{\mathbf{i}} \cdot \overrightarrow{\mathbf{v}}\right)}{\epsilon_0\left(v_\phi - \widehat{\mathbf{i}} \cdot \overrightarrow{\mathbf{v}}\right)} - \frac{1}{v_\phi}\frac{d}{d\tau}\left[\overrightarrow{\mathbf{v}} \cdot \frac{d\overrightarrow{\mathbf{P}}}{d\tau} - (\overrightarrow{\mathbf{v}} \cdot \widehat{\mathbf{i}})\left(\widehat{\mathbf{i}} \cdot \frac{d\overrightarrow{\mathbf{P}}}{d\tau}\right)\right] \tag{2.74}$$

Now to make the longitudinal and transverse wave equations more useful we will set $\overrightarrow{\mathbf{k}}, \widehat{\mathbf{i}}$ to be in the x-direction so:

$$\widehat{\mathbf{i}} \cdot \overrightarrow{\mathbf{p}} = p_x, \quad \widehat{\mathbf{i}} \times \overrightarrow{\mathbf{p}} = (0, -p_z, p_y)$$

[10] Noting $c^2 = (\epsilon_0\mu_0)^{-1}$

and so on for the other vectors. We will also use $\overrightarrow{\mathbf{u}} = \overrightarrow{\mathbf{v}}/c$. The expression for n_e then becomes:

$$n_e = \frac{\beta_\phi n_0}{\beta_\phi - u_x} \tag{2.75}$$

This means the density has a singularity whenever the fluid velocity approaches the phase velocity. This of course does not happen however it does result in large electron plasma densities and is indicative of wave breaking (see 2.3.3).

Splinting the transverse wave equation (2.73) into y and z components and making use of our expression for the plasma frequency ω_p (2.8) yealds:

$$\frac{1}{m_e c}\frac{d^2 p_z}{d\tau^2} + \frac{\omega_p^2 \beta_\phi^2}{\beta_\phi^2 - 1}\frac{\beta_\phi u_z}{\beta_\phi - u_x} = 0 \tag{2.76}$$

$$\frac{1}{m_e c}\frac{d^2 p_y}{d\tau^2} + \frac{\omega_p^2 \beta_\phi^2}{\beta_\phi^2 - 1}\frac{\beta_\phi u_y}{\beta_\phi - u_x} = 0 \tag{2.77}$$

These where first shown in [81] and form a closed set of equations for a non-linear plasma wave of arbitrary amplitude and fixed phase velocity v_ϕ. It is therefore possible to find explicit expressions for all the field components. From our expression for $\overrightarrow{\mathbf{B}}$ 2.71:

$$(B_x, B_y, B_z) = -\frac{1}{e v_\phi}\frac{d}{d\tau}(0, -p_z, p_y)$$

$$B_x = 0 \quad , \quad B_y = \frac{1}{ec\beta_\phi}\frac{dp_x}{d\tau} \quad , \quad B_z = -\frac{1}{ec\beta_\phi}\frac{dp_y}{d\tau} \tag{2.78}$$

From 2.67 we have:

$$(0, \frac{1}{ec\beta_\phi}\frac{dp_z}{d\tau}, -\frac{1}{ec\beta_\phi}\frac{dp_y}{d\tau}) = \frac{1}{v_\phi}(0, -E_z, E_y)$$

$$E_y = --\frac{1}{e}\frac{dp_y}{d\tau} \quad , \quad E_z = --\frac{1}{e}\frac{dp_z}{d\tau} \tag{2.79}$$

Naturally E_x being the most useful quantity to find for wake field acceleration it is the most difficult to derive. Starting from $\cdot\widehat{\mathbf{i}}$ of the equation of motion 2.65, and noting that $\overrightarrow{\mathbf{v}} = \overrightarrow{\mathbf{p}}/(m\gamma)$. Where $\gamma^2 = 1 + p^2/(m^2c^2)$.

$$\left(\frac{\widehat{\mathbf{i}}\cdot\overrightarrow{\mathbf{p}}}{\beta_\phi}\frac{1}{m_e c\gamma} - 1\right)\widehat{\mathbf{i}}\cdot\frac{d\overrightarrow{\mathbf{p}}}{d\tau} = e\widehat{\mathbf{i}}\cdot\left(\overrightarrow{\mathbf{E}} + \frac{\overrightarrow{\mathbf{P}}\times\overrightarrow{\mathbf{B}}}{m_e\gamma}\right)$$

$$\frac{1}{m_e c\gamma}\frac{p_x}{\beta_\phi}\frac{dp_x}{d\tau} - \frac{dp_x}{d\tau} = eE_x + \frac{e}{m_e\gamma}(p_y B_z - p_z B_y)$$

Using the expresions for B_y and B_z in 2.78:

$$\frac{1}{m_e c\gamma}\frac{p_x}{\beta_\phi}\frac{dp_x}{d\tau} - \frac{dp_x}{d\tau} = eE_x + \frac{e}{m_e\gamma}\left(-\frac{p_y}{ec\beta_\phi}\frac{dp_y}{d\tau} - \frac{p_z}{ec\beta_\phi}\frac{dp_z}{d\tau}\right)$$
$$eE_x = -\frac{dp_x}{d\tau} + \frac{1}{ec\beta_\phi}\frac{\overrightarrow{\mathbf{p}}}{\gamma}\cdot\frac{d\overrightarrow{\mathbf{p}}}{d\tau}$$

This can be simplified noting the following:

$$\gamma^2 = 1 + p^2/(m^2c^2) \Rightarrow \frac{d\gamma^2}{d\tau} = \frac{1}{m_e^2c^2}\frac{dp^2}{d\tau} \Rightarrow 2\gamma\frac{d\gamma}{d\tau} = \frac{2\overrightarrow{\mathbf{p}}}{m_e^2c^2}\cdot\frac{d\overrightarrow{\mathbf{p}}}{d\tau}$$

$$\frac{\overrightarrow{\mathbf{p}}}{\gamma}\cdot\frac{d\overrightarrow{\mathbf{p}}}{d\tau} = m_e^2c^2\frac{d\gamma}{d\tau} \tag{2.80}$$

So

$$E_x = -\frac{m_ec}{e}\frac{1}{\beta_\phi}\frac{d}{d\tau}\left[\frac{p_x\beta_\phi}{m_ec} - \gamma\right] \tag{2.81}$$

This is a widely used result. There are no general analytical solutions for this set of equations however some limiting cases exist and are shown in [82] and [81]. There is also a useful treatment in [83] which is relevant to particle acceleration in a plasma wave, which contains the following. First we will consider a PURE LONGITUDINAL PLASMA OSCILLATION. So $p_y = p_z = 0$, and so the subscript will be dropped from u_x for convenience. The longitudinal wave equation 2.74 becomes:

$$\frac{d}{d\tau}\left[(u-\beta_\phi)\frac{dp}{d\tau}\right] = m_ec\frac{\omega_p^2\beta_\phi^2 u}{\beta_\phi - u} \tag{2.82}$$

The left hand side of this equation becomes:

$$= m_ec\frac{d}{d\tau}\left[(u-\beta_\phi)\frac{du\gamma}{d\tau}\right] = m_ec\frac{d}{d\tau}\left[u\frac{du\gamma}{d\tau} - \beta_\phi\frac{du\gamma}{d\tau}\right]$$

Noting:

$$\frac{d\gamma}{d\tau} = \frac{d}{d\tau}\left(1+\frac{p^2}{m_e^2c^2}\right)^{1/2} = \frac{1}{2}\left(1+\frac{p^2}{m_e^2c^2}\right)^{-1/2}\frac{2p}{m_e^2c^2}\frac{dp}{d\tau} = \frac{u\gamma m_ec}{m_e^2c^2}\frac{1}{\gamma}\frac{dp}{d\tau} = u\frac{d\gamma u}{d\tau}$$

Thus

$$m_ec\frac{d}{d\tau}\left[\frac{d\gamma}{d\tau} - \beta_\phi\frac{du\gamma}{d\tau}\right] = m_ec\frac{\omega_p^2\beta_\phi^2 u}{\beta_\phi - u}$$

$$\frac{d^2}{d\tau^2}\left[\gamma(1-\beta_\phi u)\right] = \frac{\omega_p^2\beta_\phi^2 u}{\beta_\phi - u} \tag{2.83}$$

Now setting: $Y = \frac{d}{d\tau}\left[\gamma(1-\beta_\phi u)\right]$, and multiplying through 2.83 by Y:

$$Y\frac{dY}{d\tau} = \frac{\omega_p^2\beta_\phi^2 u}{\beta_\phi - u}\frac{d}{d\tau}\left[\gamma(1-\beta_\phi u)\right]$$

Noting:

$$\frac{d\gamma}{d\tau} = \frac{u}{(1-u^2)^{3/2}}\frac{du}{d\tau} \tag{2.84}$$

This becomes

$$\frac{1}{2}\frac{dY^2}{d\tau} = \frac{\omega_p^2\beta_\phi^2 u}{\beta_\phi - u}\frac{u}{(1-u^2)^{3/2}}\frac{du}{d\tau}\left(u - \beta_\phi u^2 - \beta_\phi(1-u^2)\right)$$

Using 2.84 then gives

$$\frac{1}{2}\frac{dY^2}{d\tau} = -\omega_p^2\beta_\phi^2\frac{d\gamma}{d\tau}$$

So finally integrating one gets:

$$\frac{1}{2}Y^2 = -\omega_p^2\beta_\phi^2\gamma + C \tag{2.85}$$

The constant C can be found by seeing that the left hand side is zero when there is a stationary point in u. This also corresponds to the maximum value of u which is this case we shall call $u_m = v_{xm}/c$ with associated Lorentz factor γ_m. So $C = \omega_p^2\beta_\phi^2\gamma_m$. Thus

$$Y = \frac{d}{d\tau}\left[\gamma(1-\beta_\phi u)\right] = \pm\sqrt{2}\omega_p\beta_\phi[\gamma_m - \gamma(\tau)]^{1/2} \tag{2.86}$$

Now noting that 2.81 gives $E_x = \frac{m_e c}{e\beta_\phi}Y$

$$E_x(\tau) = \pm\frac{m_e c}{e}\sqrt{2}\omega_p[\gamma_m - \gamma(\tau)]^{1/2} \tag{2.87}$$

This is an important result which shows that the magnitude of the electric field and the maximum gamma factor, really only depend on each other.

2.3.3 Wave Breaking

Wave Breaking is an important phenomena in plasma based accelerators as it can result in self injection into the plasma wave causing an much greater number of particles to be accelerated. In this section the standard theoretical treatment is discussed, in section 4.2.1 a more advanced experimentally applicable model is developed.

There is more than one definition of wave breaking and it depends on the oscillations involved and the type of wave. However fundamentally if the oscillation is in a fluid medium and the fluid velocity (in our case v) exceeds the phase velocity of the wave (in our case v_ϕ) the density sheets (in our case also charge sheets) will cross causing the wave to "break".

The cold relativistic wave breaking field.

Wave breaking also holds the key to understanding what the maximum possible accelerating field maintainable for a given plasma length is. Apparently this was a problem for many years before the treatment of [81] shown above was postulated. The an answer was first found by Dawson and Oberman in [84]. Here a similar expression will be found utilising a different argument.

From equation 2.87:

$$E_x(\tau) = \pm\frac{m_e c}{e}\sqrt{2}\omega_p[\gamma_m - \gamma(\tau)]^{1/2} \tag{2.88}$$

We can see the electric field takes on its maximum value when $\gamma(\tau)$ is minimum. The minimum value it can take is $\gamma(\tau) = 1$. So:

$$E_m = \frac{m_e c}{e}\sqrt{2}\omega_p[\gamma_m - 1]^{1/2} \tag{2.89}$$

So assuming our definition of a broken wave to be when $u_m = u_{\phi p} = v_{\phi p}/c$ and $\gamma_m = \gamma_{\phi p}$. Meaning the maximum velocity an accelerated electron in the wave can have is greater than the phase velocity of the wave itself.

$$E_m = \frac{m_e c}{e}\sqrt{2}\omega_p[\gamma_{\phi p} - 1]^{1/2} \tag{2.90}$$

The cold non-relativistic wave breaking field.

For non-relativistic plasmas where $u_{\phi p}$ is small, then[11] $\gamma_{\phi p} \simeq u_{\phi p}^2/2 + 1$, and equation 2.90 can be simplified. So

$$E_m = \frac{m_e \omega_p c u_{\phi p}}{e} = \frac{m_e \omega_p v_{\phi p}}{e} \tag{2.92}$$

[11] Using the Taylor expansion

$$\frac{1}{(1-x)^{1/2}} = 1 + \frac{x}{2} + ... \tag{2.91}$$

With more approximation it can be seen that in a cold electron plasma the maximum electric fields that can be sustained are

$$E_m \simeq cm_e\omega_p/e \equiv E_0 \tag{2.93}$$

which is sometimes in the literature given the symbol E_0. And

$$E_0 \approx 96\sqrt{n_0(cm^{-3})}$$

this is known as the non-relativistic wave breaking field.[85]

2.3.4 The critical power for self focusing

Transverse variation in the plasma density and thus the refractive index can lead to self focusing in LWFA. This focusing effect is often balanced by diffraction so the laser can from a channel much longer than the Rayleigh length. It is useful to know the critical power for self focusing and it is given by [86]:

$$P_c = \frac{8\pi\epsilon_0 m_e^2 c^5 \omega_0^2}{e^2\omega_p^2} \approx 17\frac{\omega_0^2}{\omega_p^2}\text{GW} \tag{2.94}$$

2.3.5 Laser Depletion Length

Suffice is to say that laser plasma interactions cannot go on indefinitely. Eventually the driving laser pulse will lose all its energy to the plasma. It can be shown that for $a_0 << 1$, the so call pump depletion length, (other wise known as the etching length) is given by [86]:

$$L_{ETCH} = \tau_0 c\frac{n_c}{n_e} \tag{2.95}$$

Where τ_0 is the duration of the laser pulse before entering the plasma.

2.3.6 The Dephasing Length

One of the largest limiting factors in LWFA is that the accelerated electron will eventually overtake the accelerating structure which is mearly moving at the plasma wave phase velocity. In one dimension it can be shown that the distance over which this take to occur is [86]:

$$L_\phi = \frac{2}{3}\frac{n_c}{n_e}R \tag{2.96}$$

Where R is the bubble radius. This limit can however be over come by the use of staged LWFA as the phase velocity of the accelerating structure can be increased in each subsequent stage by lowering the plasma density.

2.3.7 Betatron Radiation

Electrons in blow out regime (ignoring accelerating field) undergo oscillations at a frequency $\omega_\beta = \frac{\omega_p}{2\gamma}$.

For large oscillations ($K_\beta = \gamma k_\beta r_\beta > 1$) this produces X-ray radiation with a synchrotron-like radiation spectrum characterised by a spectrum $d^2I/(dEd\Omega)_{\theta=0} \propto \xi^2 \mathcal{K}^2_{2/3}(\xi/2)$, where $\mathcal{K}_{2/3}(x)$ is a modified bessel function of order 2/3 and $\xi = E/E_c$.

The shape of this spectrum is characterized by a single parameter, the critical energy E_c. The on-axis spectrum is broadband and peaked close to E_c, which can be approximated to be $E_c = 3/4\hbar\gamma^2\omega_p^2 r_\beta/c$ where r_β is the amplitude of the oscillations.

Chapter 3

Methods.

This chapter will describe methods used to obtain the experimental results in this work. My thesis is concerned with the relativistic electrons and radiation produced by laser wake field accelerators so methods of electron measurement and x-ray measurement will be described here.

3.1 Electron Measurement.

A broad scope of electrons from a span of different plasma processes exits the LWFA before recombination takes place. Although a LWFA plasma also emits low energy electrons in a myriad of directions, it is important to measure the high energy electron beams that can be created by LWFAs. Indeed these are among the most interesting aspects of the phenomena. For this thesis, concern is focused on examining the highly relativistic electrons: finding where and in what direction they exit the plasma; how they are distributed in space; their number; and how much energy they carry. This section describes the methods used to do so.

3.1.1 Electron Spectrometry.

Here the basics of electron spectrometry are discussed. Though the spectrometers used in this work were by and large built, modified and dismantled in a number of weeks. The basic design differs between only two archetypes, a single and two screen design. For the data taken the only change from these archetypes is the magnet used and the distances which separated the magnet and other components.

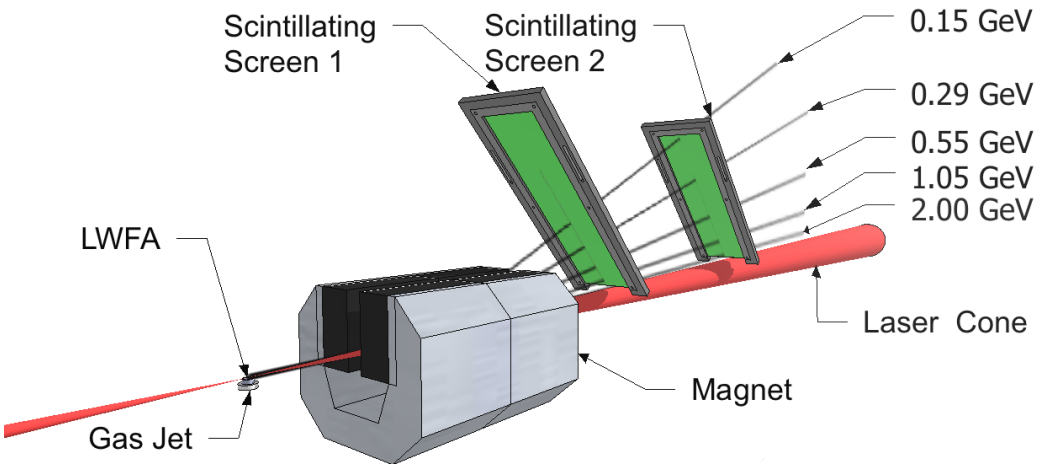

Figure 3.1: A two screen electron spectrometer. Electrons of differing energies are shown passing through scintillating screens as calculated by tracking algorithm. The setup shown is for the Gemini 2011 experiment, and the magnet field map is shown in figure 3.4.

Basics of Electron Spectrometry.

In order to find the kinetic energy of electrons they may be passed through a magnetic field so that particles of different momenta are dispersed by different angles. If they are then detected using some method their energy can be ascertained. Though it should be noted that in this method particles of different mass but the same charge such as muons and electrons can have the same dispersion angle and be mistaken for each other unless the method of detection is able to distinguish them.

The trajectory of an electron through an ideal rectangular magnetic field can be solved analytically. Consider a uniform magnetic field of length L_m parallel to the electrons motion and of width sufficient to allow the electron to exit the boundary perpendicular to the electrons motion, (essentially the same as a field infinite in extent perpendicular to the electrons motion) figure 3.2.

$$\begin{aligned} \overrightarrow{\mathbf{B}}_z(x) &= B_{max}\widehat{\mathbf{z}} & 0 < x < L_m \\ \overrightarrow{\mathbf{B}}_z(x) &= 0 & 0 > x > L_m \end{aligned}$$

An electron will be deflected by the Lorentz force:

$$\frac{d\overrightarrow{\mathbf{P}}}{dt} = \frac{q}{\gamma_e m_e}\overrightarrow{\mathbf{P}} \times \overrightarrow{\mathbf{B}} \tag{3.1}$$

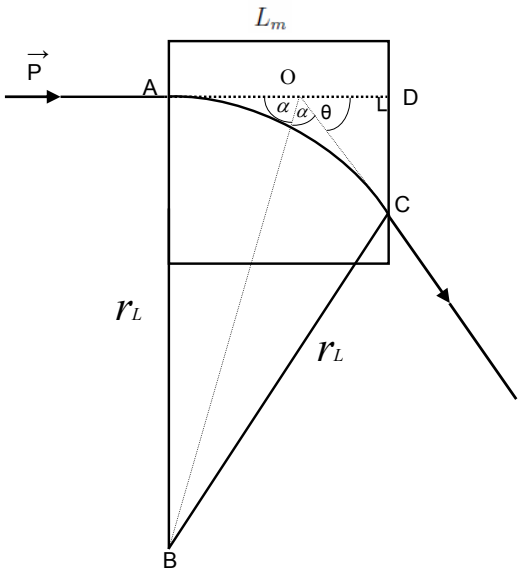

Figure 3.2: The geometry of an electron passing through an ideal rectangular magnetic field.

Equating this to the centripetal force $\vec{\mathbf{P}}^2 m_e^{-1}\gamma_e^{-2}r_L^{-1}$ where r_L is known as the Larmor Orbit gives:

$$r_L = \frac{|P|}{qB_{max}} \tag{3.2}$$

From ΔAOB in figure 3.2 and from the fact that $\Delta AOB = \Delta COB$ it is trivial to show that:

$$\tan\frac{\theta}{2} = \frac{AO}{r_L} \tag{3.3}$$

Similarly it can be shown:

$$AO = \frac{L_m}{1+\cos\theta} \tag{3.4}$$

Thus the analytical equation for the dispersion angle of an electron θ is:

$$\tan\frac{\theta}{2}(1+\cos\theta) = \frac{L_m e B_{max}}{|P|} \tag{3.5}$$

So using the small angle approximation: $\tan\theta \approx \theta$ and $\cos\theta \approx 1-\theta/2$, the left hand side becomes: $\theta+\theta^2/4$. Which means that for deflections of <100mrad the dispersion angle is proportional to $L_m B_{max}$. So in order to increase the dispersion angle, the magnetic field must be increased in magnitude, or the length of the field must be increased.

We have essentially reached the limit of peak field intensity using neodymium magnets in previous work.So in order to increase the dispersion angle of high energy electrons, longer magnets where constructed to produce the results in this work. Though another approach would be the use of electromagnets or superconducting electromagnets, which can support higher peak magnetic fields. However the smaller size of the electromagnets is often countered by the size or the necessary power supplies and cooling apparatus.

In this work a range of LWFA experiments are presented which produced electrons of energies up to over a GeV but also electrons with energies down to MeVs. Different magnets are appropriate for looking at different energy ranges. If $L_m B_{max}$ is too low then electrons are not deflected sufficiently to have good resolution and to give precise measurements. If $L_m B_{max}$ is too large then electrons are deflected too much and will impact inside the magnet. Magnet selection was made using theoretical predictions of the range of electron energies exiting the LWFAs.

In order to calculate energy of electrons once they were detected I used a code developed over a number of years in-house at Imperial College. [The Imperial College Tracker]. It works by solving the Lorentz force (3.1) numerically using a centre-differencing (or leap-frog) method. Where the approximation:

$$\frac{\overrightarrow{\mathbf{P}}(t+dt) - \overrightarrow{\mathbf{P}}(t-dt)}{2dt} \approx -\frac{e}{m_e\gamma(t)}(\overrightarrow{\mathbf{P}}(t) \times \overrightarrow{\mathbf{B}}(t,x,y)) \tag{3.6}$$

Becomes:

$$\overrightarrow{\mathbf{P}}(t+dt) \approx -\frac{e}{m_e\gamma(t)}(\overrightarrow{\mathbf{P}}(t) \times \overrightarrow{\mathbf{B}}(t,x,y))2dt + \overrightarrow{\mathbf{P}}(t-dt) \tag{3.7}$$

Where dt is small. Then using the forward difference method it calculates the electrons position. Where the approximation:

$$\frac{x(t+dt) - x(t)}{dt} \approx \frac{P_x}{m_e\gamma(t)} \tag{3.8}$$

Becomes:

$$x(t+dt) \approx \frac{P_x}{m_e\gamma(t)}dt + x(t) \tag{3.9}$$

This code has been heavily benchmarked and compared with the analytical solution.

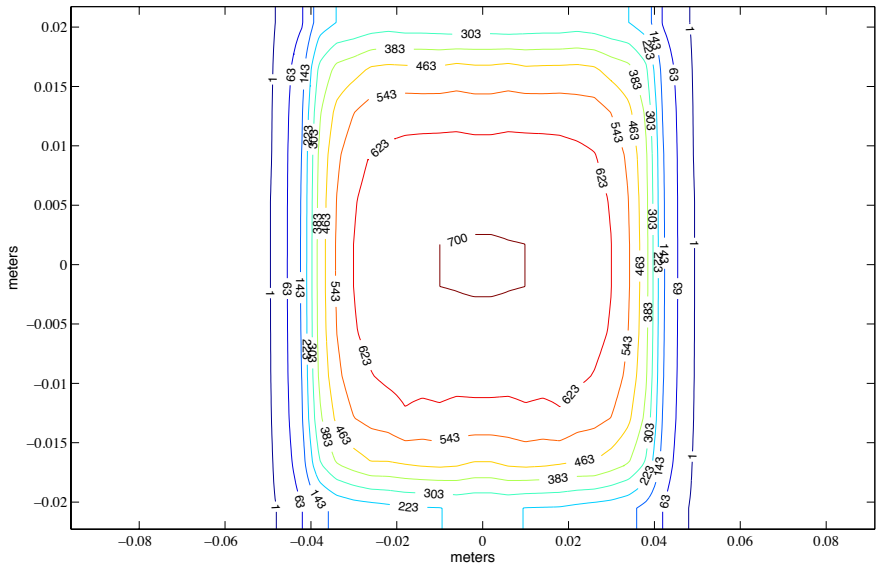

Figure 3.3: The mapped field of the magnet used in the Lund Experiment. The units of the labelled contours are mT .

Single Screen Design

In the simple case of a single screen electron spectrometer The electrons are dispersed through a magnet and impact on an electroluminescent screen at 45^0 to the laser axis.

The magnet's fields were measured using a Hall probe mounted on a micrometer stage. The magnetic field maps are shown in figures 3.3 and 3.4 along with their dimensions. In each case the fields where found to not vary appreciably in the dispersion direction which is out of the page in relation to the figures.

The electroluminescent screen used for all the experiments was composed of Gd_2O_2S:Tb and is sold under the trade name Kodak Lanex. Gd_2O_2S:Tb emits 546nm photons when energy is deposited in the scintillator layer by incident electrons. The energy deposited is an almost constant (80 eV) for electrons of energy greater than 4 MeV [87]. So energies less than this were discarded in the analysis. The screens were shielded from laser and interaction light on the front by layers of Al coated Mylar as this would also cause luminescence. The screens were imaged from the back by CCD's at an angle of 45^o. The imaging lines were fitted with 546 nm interference filters to minimize the signal from non-electroluminescent light. The relaxation time of the scintillator is of the order of a millisecond. Thus to further minimize the signal

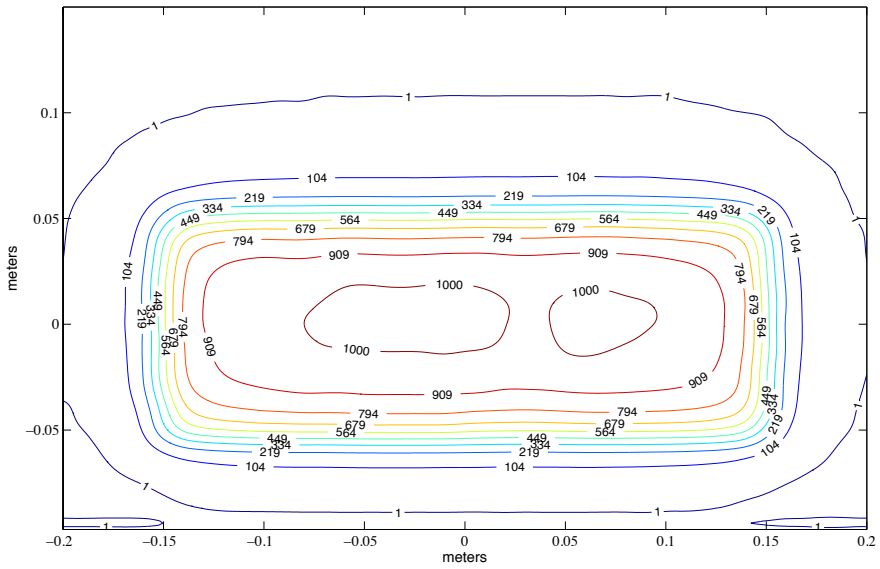

Figure 3.4: The mapped field of the magnet used in the Gemini Experiment. The units of the labelled contours are mT. The magnet consists of rectangular pole pieces constructed from sintered neodymium blocks, mounted in a c-shaped yoke. This c-shape allows low energy electrons to leave the spectrometer without striking the yoke, further reducing the bremsstrahlung radiation produced. The pole piece separation is 25 mm. We find that the field maximum is 1.02 T in the mid-plane of the magnet with a field uniformity of 0.01 T r.m.s. over the central 200 mm of the magnet. The yoke design ensures that there is no field reversal along the electron propagation direction. The magnet is constructed in two sections, each 150 mm long. In this experiment these were fixed together providing a single magnet 300 mm long.

from non-electroluminescent light the CCD's were triggered 0.1 ms after the electron beam. This is long enough for laser light not be present and for the light from plasma recombination to have ceased. However in practice it was found that laser or recombination light could be reflected onto the backs of the Lanex screens and cause photoluminescence. For this reason light tight shielding was installed as well.

Electrons with positive or negative momentum in the magnets dispersion direction (i.e. electrons which exit the accelerator at an angle to the spectrometer axis) can cause the beam energy to be over or under estimated, (see figure 3.5). In addition the electron beams spatial extent in the dispersion direction and the lasers pointing variation can have a similar effect.

One way to limit the uncertainty of the measurement due to this is to employ a collimator before the electron beam enters the magnet, to stop these electrons. However in this work I am interested in measuring the x-rays created in the LWFA. The electrons stopped in the collimator would be in the line of sight of the x-rays being measured and would create large amounts of bremsstrahlung radiation in the same cone. This would introduce large amounts of noise to the x-ray measurement. This makes the use of collimating apertures unsuitable for electron spectrometers for experiments where betatron radiation is important.

It is however possible to use the electron beam divergence in the non-dispersion direction, as detected on the scintillating screen, to give estimates of the spatial extent of the electron beam and deduce its divergence. Thus assuming this is the same in the dispersion direction the uncertainty in the electron energy can be assessed. This assumption is however not always valid. This method also does not deal with the problem of laser pointing variation. Another way is to use the information provided by an electron beam pointing measurement. However as these could not be done on the same shot as the electron measurements only statistical measurements can be used. Finally a two screen spectrometer method can be utilized as described below.

Two Screen Design

As shown in Figure 3.5, electrons with different energies can strike the same point on a single screen due to differing exit angles. However with the inclusion of a second screen their energies and angles can be ascertained. Separating the exit angle from the electron energy is equivalent to measuring two components of the electron momentum: the electron momentum in the laser propagation direction (p_z), and the

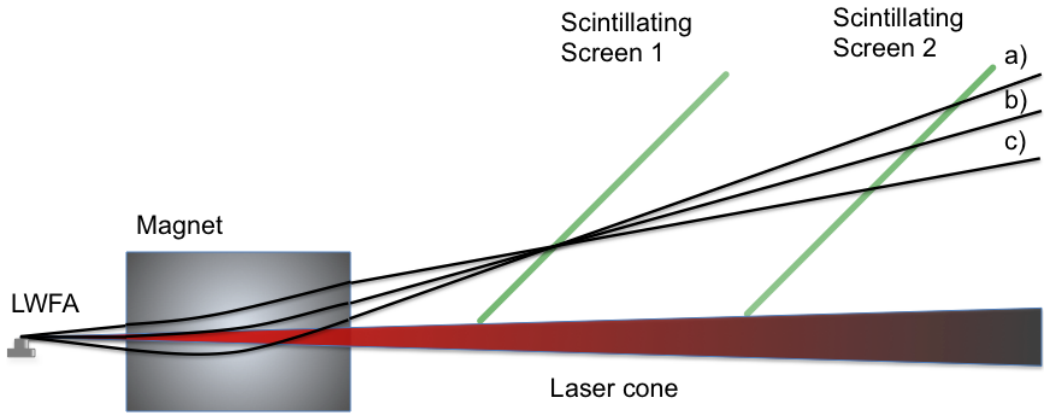

Figure 3.5: Three electron paths are shown which all impact screen 1 at the same position. b) Shows the path of an electron exiting the LWFA along the laser axis. a) Shows a higher energy electron exiting at a positive angle. c) Shows a lower energy electron exiting at a negative angle.

electron momentum in the magnet dispersion direction (p_y). The third component of the electron momentum (p_x), can be recovered from the position of the electron beam on the screens in the direction perpendicular to the magnet dispersion direction.

The two-screen method allows the bending magnet to be placed close to the LWFA without a collimator, see figure 3.1. This allows the whole electron beam to pass between the magnet pole pieces without deteriorating the magnet performance, thereby reducing bremsstrahlung radiation. This geometry also produces sufficient deflection of electrons away from the laser axis reducing the chance of the electron beam colliding with x-ray detectors. This collimator-free two screen spectrometer still allows a reliable and full measurement of the electron energy to be produced. Furthermore the method allows all three momentum components of the electron beam to be measured which can provide insight into the acceleration and radiation generation mechanisms.

In order to find the energy and angle of exit from the LWFA of a given electron, it is necessary, to first identify what point it passes on both of the electroluminescent screens, which I will call $\vec{\mathbf{s}}_1$ and $\vec{\mathbf{s}}_2$.

If many electrons are incident on the screens identifying these positions is not trivial. One method of solving this problem is to place fiducials in the beam between the two screens, creating shadows in the images on the second screen. However this method has the disadvantage of not sampling the whole spectrum. Alternatively, I identified $\vec{\mathbf{s}}_1$ and $\vec{\mathbf{s}}_2$ points using clearly identifiable features in the electron spec-

trum.

Once a feature has been identified and points $\overrightarrow{\mathbf{s}}_1$ and $\overrightarrow{\mathbf{s}}_2$ have been defined, the correct electron momentum and exit angle (or equivalently p_z and p_y) can be found by tracking electrons through the mapped magnetic field using the relativistic Lorentz force equation in an iterative process. There are two methods which I considered in order to solve this computational problem.

The first is, given the two points on the screens $\overrightarrow{\mathbf{s}}_1$ and $\overrightarrow{\mathbf{s}}_2$ the point at which the electron exits the magnet and its position vector could be found. In the same way as the Lorentz force solver described above tracks an electron through the magnet it should be possible via reversing time and charge to track the electron back through the magnet and iteratively guess the electrons energy until its path takes it back to the LWFA. This has the advantage of having only one iteration loop.

However given I already had access to a well benchmarked iterative tracking code. The second method which I used is as follows, and is depicted in figure 3.6. I modified the existing Imperial College Tracker code slightly to act as a matlab function which when passed a given exit angle and energy, would only track a single electron through a magnetic field set up given by another file. The algorithm I wrote then receives the input of $\overrightarrow{\mathbf{s}}_1$ and $\overrightarrow{\mathbf{s}}_2$ and starts with a guess of an angle and energy, passes this to the matlab function, which passes back to it the positions $\overrightarrow{\mathbf{r}}_1$ and $\overrightarrow{\mathbf{r}}_2$ which are the screen positions for this guess of the angle and energy. There are two loops.

In the first loop $\overrightarrow{\mathbf{r}}_1$ is compared to $\overrightarrow{\mathbf{s}}_1$. Depending on which is larger the guess of energy is changed. The process is repeated iteratively until the difference between $\overrightarrow{\mathbf{r}}_1$ and $\overrightarrow{\mathbf{r}}_2$ is small.

Then $\overrightarrow{\mathbf{r}}_2$ and $\overrightarrow{\mathbf{s}}_2$ are compared. Depending on which is larger the angle is changed. Then the first loop is repeated.

Finally, when $\overrightarrow{\mathbf{r}}_1$ and $\overrightarrow{\mathbf{r}}_2$ match $\overrightarrow{\mathbf{s}}_1$ and $\overrightarrow{\mathbf{s}}_2$, within a certain tolerance, the algorithm outputs the energy and exit angle of the electron.

I chose this method because it was more compatible with the existing bench marked code, and all the ancillary magnetic field maps and libraries developed for it could be retained. Computationally the first method would in principle be faster. However this code takes around 10 minutes to run a dozen points on a desktop computer so further optimization was not necessary for my purposes.

It is not necessarily the case that for highly non-uniform magnetic fields there will be a unique mapping of momentum vectors p_z and p_y to positions on the screens $\overrightarrow{\mathbf{s}}_1$

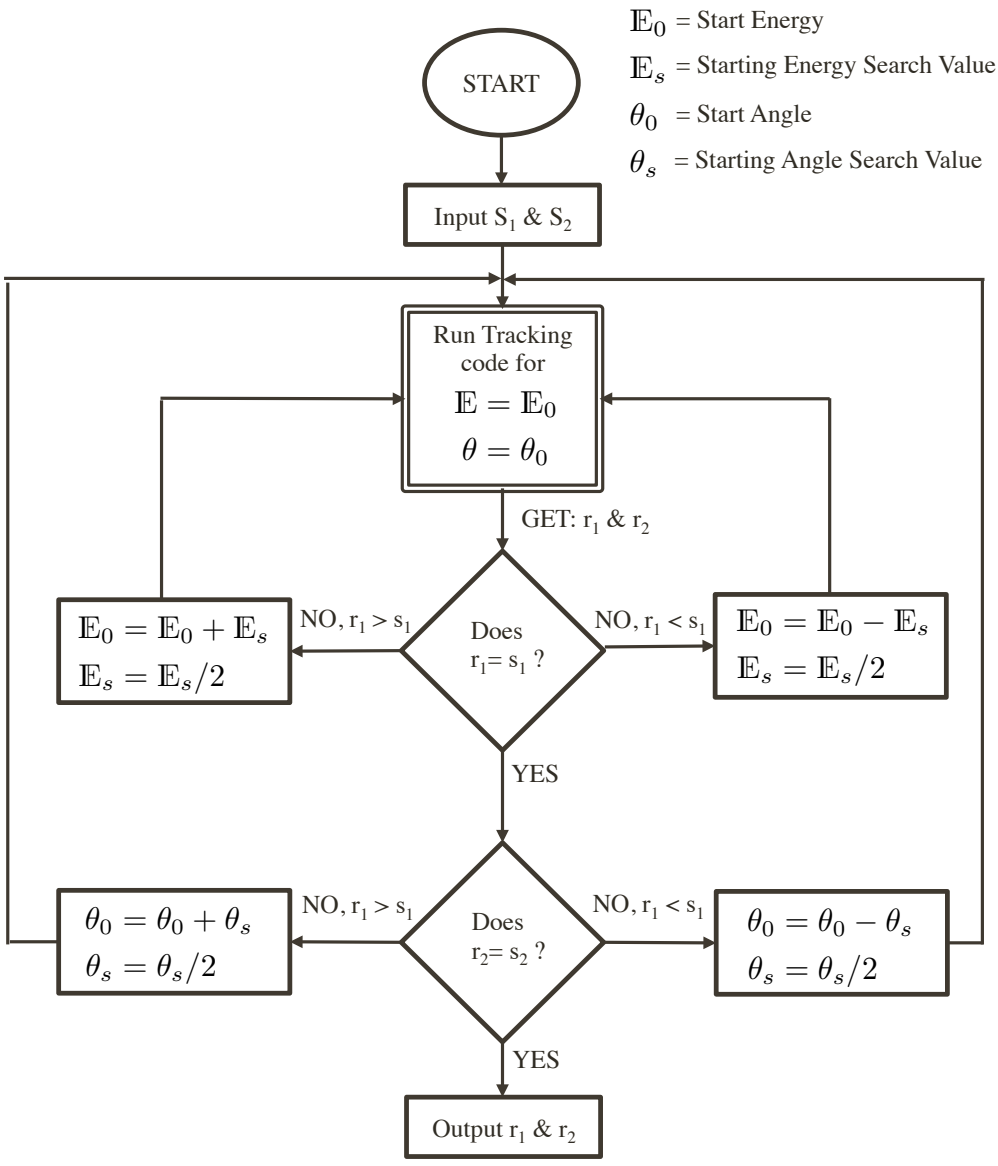

Figure 3.6: Diagram of the iterative algorithm for finding the energy and exit angle of electrons exiting a LWFA incident on a two screen spectrometer.

and $\overrightarrow{\mathbf{s}}_2$. However as shown in figures 3.3 and 3.4, the magnetic fields which I have used are highly uniform. This leads to there being a unique mapping as long as the electron source point is known. I verified this by carrying out fittings of electrons of energies between 1 MeV and 2 GeV with exit angles of between +100 mrad and -100 mrad. I took note of the turning points in the positions on the screens where the electrons hit. There where no obvious discontinuities and so concluded that the map from p_z and p_y to $\overrightarrow{\mathbf{s}}_1$ and $\overrightarrow{\mathbf{s}}_2$ is smooth.

So the two-screen method allows the full three dimensional momentum distribution of the beam to be examined which provides insight into the dynamics of electron motion in a LWFA such as injection and acceleration. This is vital for understanding the processes responsible for beam instabilities and x-ray generation.

3.1.2 Electron Profile Measurements.

In various places I will refer to electron profile measurements. These were conducted using a similar method to the electron spectrometry. However instead the deflecting magnet was removed and a scintillating screen was placed along the laser axis after the LWFA. It was positioned at 45 degrees to the normal of the laser axis and imaged using mirrors and lenses terminating in a CCD camera placed at 45 degrees to the final mirror thus removing the distortion due to angle. The scintillating screen is constructed in the same way as for the spectrometers with layers of aluminised Mylar to block laser light and Lanex scintillator however with the addition of a sheet of solid aluminium to block low energy electrons ($\lesssim$ 1 MeV).

3.2 X-Ray Measurement

In this section I will describe the methods I used to measure the betatron x-rays generated by the wakefield accelerators, the goal being to arrive at a measurement of the peak brightness and critical energy of the x-ray spectrum. These two numbers together give you all you need to know about the x-rays assuming betatron like spectrum.

The basic method is to deflect the electrons produced by the laser wakefield accelerator so that they are no longer concurrent with the x-ray beam, filter out any remaining laser light, pass the x-rays through a filter pack made of materials with different atomic weights, and then detect the x-rays using a phosphor and a CCD

camera. By using the known transmission curves of the filters making up the filter pack, an iterative fitting algorithm was used to find the critical energy of the synchrotron like spectrum which best fitted the observed experimental data. This along with a calculation of the number of photons incident on the detector and measurements of the size of the x-ray source is sufficient to give the peak brightness of the x-ray spectrum.

I will start off by describing the filter pack designs used in this thesis, then discuss the details of the data treatment and finally talk about the x-ray detection system.

3.2.1 Filter Pack Design

The purpose of the filter pack is to find the spectrum of the x-rays transmitted through it. The method is similar to the use of Ross filters, where the purpose of the filters is to produce a mono-chromatizing effect. In Ross filters this is accomplished by using two filters composed of elements of adjacent atomic number with thicknesses adjusted so that the transmitted spectra are identical for all wavelengths except those lying within the K-absorption limits [88]. Here however, instead of using only two filters, a number are used with K-alpha absorption peaks spread across the range of wavelengths we wish to measure. This allows for the spectrum to be fitted using an iterative (trial and error) algorithm.

The first filter pack I constructed using the design in Kneip 2010 [89]. It is shown in figure 3.7 and was used in the experiment using the Lund laser (18 TW). It is designed to measure the spectrum between 1 and 10 keV as this is a x-ray energy range consistent with a 18 TW laser producing a LWFA betatron spectrum [90].

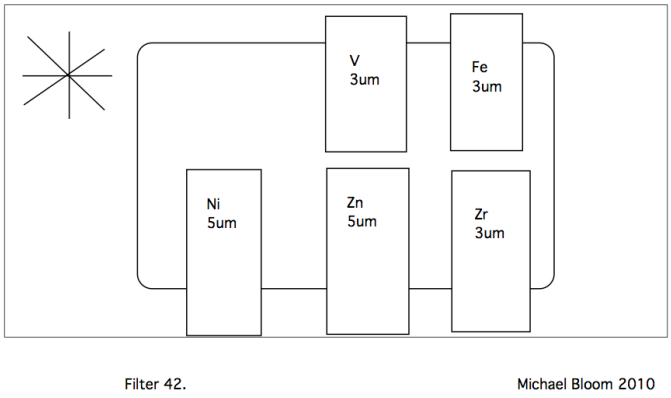

Figure 3.7: Initial filter pack design. Designed for categorising the critical energy of a betatron-like x-ray spectrum between 1 and 10 keV. The backing material 6 μm of mylar (Biaxially-oriented polyethylene terephthalate) with 90 nm of aluminium.

Element	K-edge KeV
V	6
Fe	7
Ni	8
Zr	10
Zn	18

Figure 3.8: Table of filters used in initial filter pack design. Designed for categorising the critical energy of a betatron like x-ray spectrum between 1 and 10 keV.

As I was to conduct experiments using the much more powerful Gemini laser, (which produced a peak power on target of 180 TW during the experiment), I needed a way to measure x-ray spectrums with critical energies between 1 and 100 keV. To this end I adapted the filter pack method selecting elements with k-alpha absorption edges as equally spaced as possible across this energy range, while considering their availability, chemical stability, affordability and safety. I chose filter thicknesses which would provide a similar transmission of betatron like spectra other than the changes due to the K-alpha edge, which could be fabricated by combining layers of commercially available foils. I tested the filter pack fitting algorithm by creating test x-ray spectra, adding Gaussian noise, passing them through the transmission curves expected for my selected thicknesses of elements [91], also adding appropriate noise at this stage. I then took the resultant signals through each filter and used the fitting

algorithm to calculate the critical energy of the original spectra. With some adjustment to the filter thicknesses I found filter elements and thicknesses which worked effectively. These are shown in the table of figure 3.9.

Element	Thickness mm	K Edge KeV
V	0.003	6
Zn	0.005	18
Mo	0.050	20
Sn	0.050	29
Pr	0.050	43
Gd	0.050	50
Yb	0.050	61
W	0.025	70
Au	0.010	81
Pb	0.040	88
Bi	0.040	91

Figure 3.9: Table of elements used in filter pack designed for betatron like spectra with critical energies between 1 and 100 keV.

My first attempt at measuring x-rays, from the Lund laser, is not presented in the accompanying chapter on the experiment, as I found fitting the spectrum using the algorithm was not possible due to the noise levels being too high. I will however discuss it here as it helped inform the methodology in the subsequent experiments and my filter pack design.

Figure 3.10 shows an image from the x-ray camera in the Lund experiment with the filter pack from figure 3.7. In the sections 1 and 8 shown in the figure 3.10 2 mm pieces of copper have been placed. The signal through these sections is due to Bremsstrahlung gamma rays generated by the electron beam from the LWFA stopping. This prevented the x-rays from being properly categorised on this occasion. For the Gemini experiment I took measures to prevent this problem described in that chapter.

I did however note from figure 3.10 the signal through the thin backing material could be useful. I wanted to address the potential problem of the x-ray beam not being homogenous across the field of view of the x-ray camera. This could come about if the beam was smaller than the solid angle of the CCD. It could also come about if the beam was not centred on the x-ray camera and there was a change

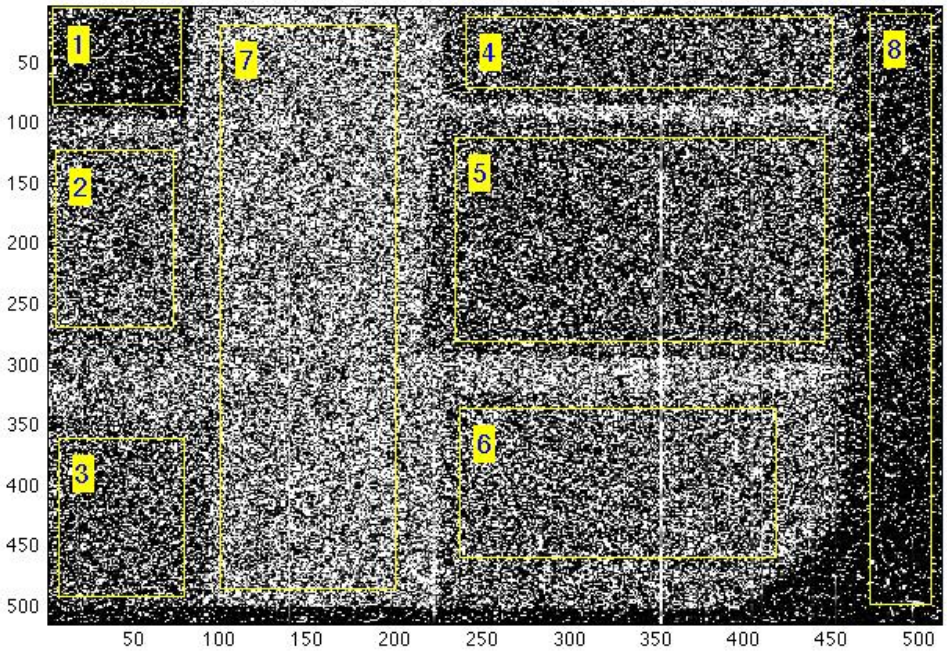

Figure 3.10: This a typical (if bright) image captured by the x-ray camera on the Lund experiment. The different filters are clearly visible. For analysis purposes the image is broken into the sections shown. 1) and 8) act as a background calibration and are covered with 2mm Copper. 2) 3μm V, 3) 3μm Fe, 4) 5μm Ni, 5) 5μm Zn, 6) 3μm Zr, 7) The backing material 6 μm of mylar (Biaxially-oriented polyethylene terephthalate) with 90 nm of aluminium. The camera was a front illuminated Andor CCD mounted in vacuum. The axis show pixel number.

in intensity across the chip. For this reason I selected a grid design (as shown in figure 3.11). This would mean that it would be possible to know if the beam was inhomogeneous, something that would not necessary be possible without a thin grid of backing material. It would also allow for measurements to be made if the x-ray beam changed in intensity across the field of view, of course assuming that the change in x-ray spectrum was small.

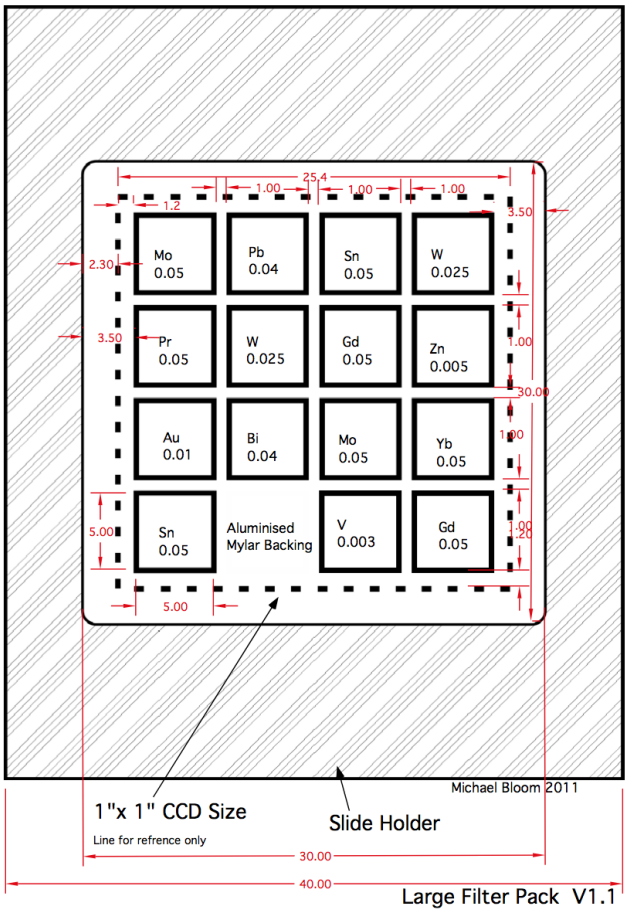

Figure 3.11: Grid filter pack design 4x4. Designed for categorising the critical energy of a betatron like x-ray spectrum between 1 and 100 keV. The backing material 6 μm of mylar (Biaxially-oriented polyethylene terephthalate) with 90 nm of aluminium. Used in the Gemini Experiment chapter.

In the design of the filter in figure 3.11, some key filter elements are repeated. This is for two reasons, one for the case of the x-ray beam covering a smaller angle than the filter pack, the section for improved confidence in measuring a inhomogeneous x-ray beam. In the case of the x-ray beam covering a smaller section of the filter pack, the filters are arranged to hopefully allow the spectrum to be fitted with only a subset of exposed filters.

In the case of a large inhomogeneous beam this allows the signal through repeated filters to be compared. If the ratio of these repeat filter to the surrounding backing material is the same at different positions on the field of view, then one can conclude that change in x-ray spectrum energy is small across the field of view. Subsequently

the sections of the grid around each filter can be used to normalise the signal before being passed to the fitting algorithm allowing beams of inhomogeneous intensity to have their critical energy fitted.

Once the manufacturing process had been perfected I was able to further improve on the design by cutting the area of each filter by a quarter, leading to the filter design shown in figure 3.12. This has the advantage of more repetition of elements thus increasing the confidence in the measurement.

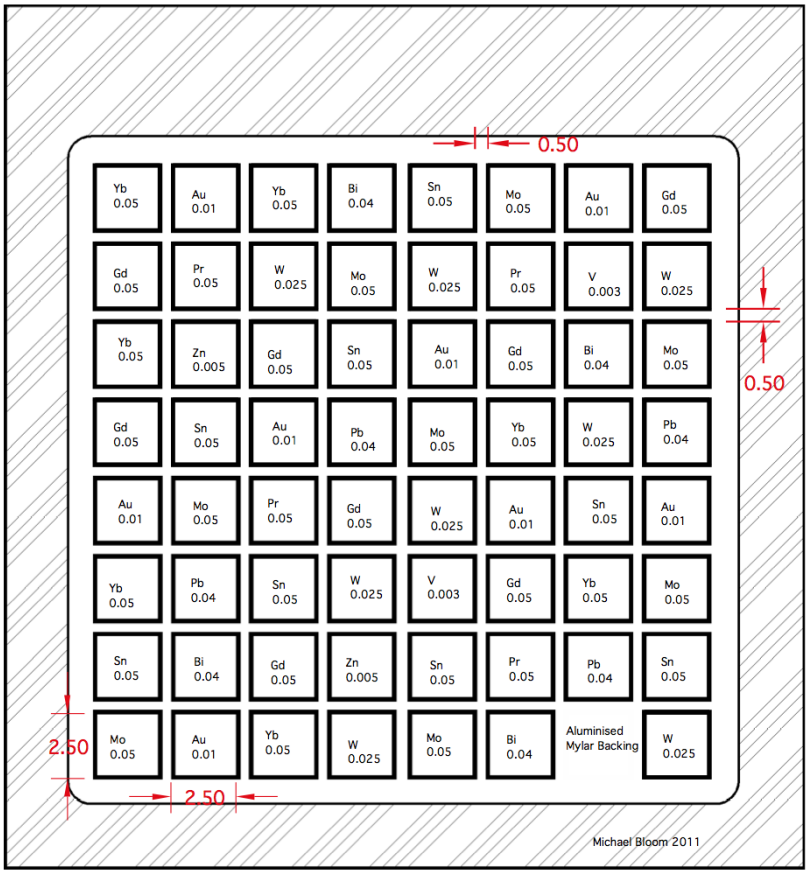

Figure 3.12: Grid filter pack design 8x8. Designed for categorising the critical energy of a betatron like x-ray spectrum between 1 and 100 keV. The backing material 6 μm of mylar (Biaxially-oriented polyethylene terephthalate) with 90 nm of aluminium. Used in the Gemini Experiment.

3.2.2 Data Treatment for X-ray Spectrum

In the x-ray measurements discussed in the chapter on the Gemini Experiment. The x-ray beam was found to be inhomogeneous, figure 3.13 shows an extreme example.

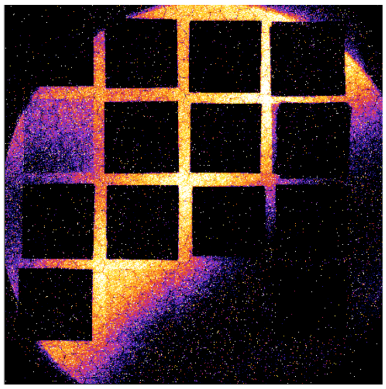

Figure 3.13: An image from the Princeton PIXIS camera system used on the Gemini experiment. The colour table is arbitrary but linear. One can see the x-ray beam varies in intensity.

Due to this the signal through each elemental filter was normalised to the four backing regions around it (shown in figure 3.14. Then passed through the fitting algorithm. The long Al vacuum tube (shown in figure 3.15) is used to measure the level of bremsstrahlung gamma rays in the four regions at the corners of the image, this is subtracted from the data before the photon number is calculated. Once normalised the ratios between repeat filters were seen to be the same. Allowing for the assumption of only a small change in spectrum across the field of view of the camera.

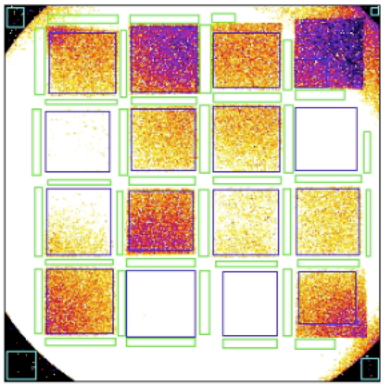

Figure 3.14: An image from the Princeton PIXIS camera system used on the Gemini experiment. The colour table is arbitrary but linear and saturated in places. The extent of each filter region is shown in blue. The regions around each filter(to normalise for inhomogeneities in the beam) are shown in green.

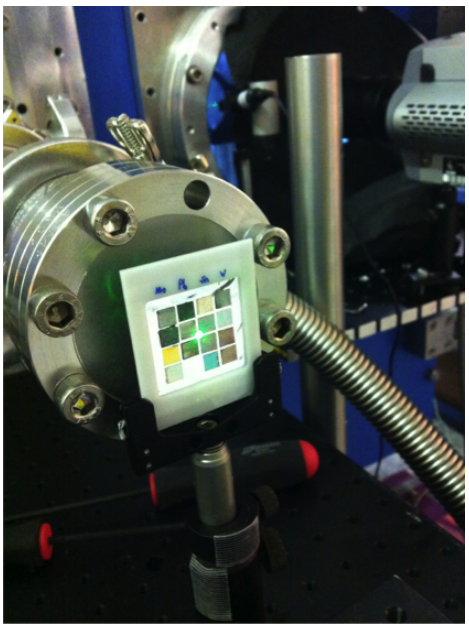

Figure 3.15: Photograph of a filter pack in place on the Gemini experiment. A beryllium window is used to pass the x-rays into air. The length of vacuum tube is used to provide information on the level of bremsstrahlung radiation.

3.2.3 Princeton PIXIS camera

In order to detect and characterise x-rays which have energies between 1 keV and 100 keV a PIXIS-XF:2048BL system supplied by Princeton Instruments was used. This consisted of a Csl:TI scintillator coupled to a CCD array using optical fibres and enclosed behind a Be window. The process of x-ray detection involved in this system is summarised in the illustration of figure 3.16.

The Csl:TI has a reasonably good response to x-rays in the 10 - 100 keV part of the spectrum as shown in figure 3.17. For the measurements of the x-ray source reported in this thesis, it was necessary to absolutely calibrate the camera response, i.e. to provide a direct relationship between the signal recorded by the camera and the number of incident photons. This was performed using an Fe-55 source. The following section describes this calibration process and the method for calculating the absolute number of photons.

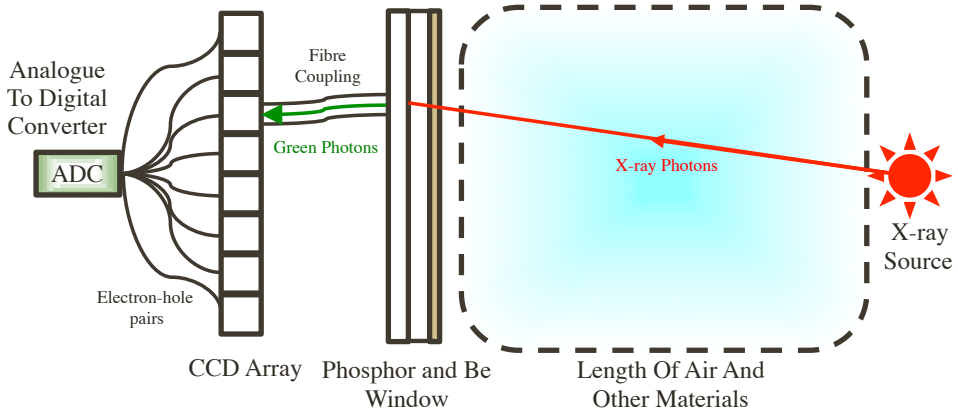

Figure 3.16: An illustration of the stages involved in an x-ray causing an ADC count in the Princeton PIXIS camera system.

Calculation of Princeton PIXIS system counts from photon number.

To understand the coefficients that need to be calibrated, consider the calculation of the number of counts given by a certain number of x-ray photons incident on the Princeton PIXIS system for a given x-ray spectrum. It can be considered as follows, (working from right to left in illustrationin figure 3.16):

1. Let us assume a known spectral shape function ($S'(E)$), which gives the number of photons per photon energy (E). For instance a synchrotron like spectrum could be assumed.

2. The fraction of the total number of photons in the spectrum at a given energy ($S(E)$) is then given by the following integral equation:

$$S(E) = \frac{S'(E)}{\int S'(E)dE} \tag{3.10}$$

3. The fractional transmission of x-rays through the length of air and/or other materials such as metallic filters and Be windows between the x-ray source and the Princeton PIXIS system is given by the function $T(E)$. This function can be found from reference values [91], as long as the length of air or of other materials is precisely measured.

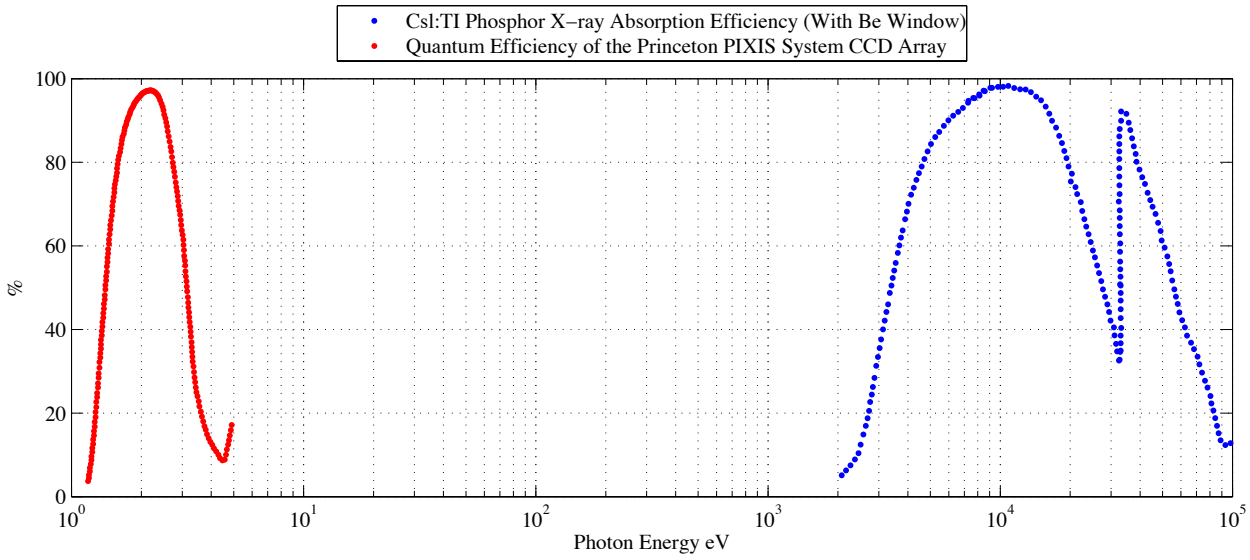

Figure 3.17: The Princeton PIXIS system's CCD array quantum efficiency is shown in red. The Princeton PIXIS camera system's Csl:TI scintillator's x-rays absorption efficiency is shown in blue. This includes the transmission through the 10 mm Be window. Data reproduced from Princeton Instruments documentation [92].

4. The fraction of photons absorbed as a function of photon energy in the scintillator $Q(E)$ is given in figure 3.17. This also takes account of the transmission of the integrated Be window which is part of the Princeton PIXIS system.

5. The integral I then gives the total energy deposited in the phosphor on average per photon of the incident x-ray spectrum.

$$I = \int T(E)Q(E)S(E)EdE \tag{3.11}$$

6. Now that a certain amount of x-ray energy has been deposited in the phosphor scintillator it will produce 2.25 eV green photons with a certain energy conversion efficiency g.

7. The green photons are emitted over an angular distribution, some fraction of them (α) are captured and guided to a CCD array pixel by an optical fibre (or collection of fibres). This constant α will not necessary be the same for all camera pixels. This is because distortions and blemishes are inherently produced during the fibres' manufacturing process and introduce distortion and

non-uniformity of response in the fibres, [93]. In addition certain 'dead' fibres are used by design and create the hexagonal pattern seen in figure 3.20c). These effects collectively can be modelled by a slight variation in the constant α.

8. The green photons are then deposited in the CCD. The CCD quantum efficiency can be seen in figure 3.17. Its efficiency for 2.25 eV photons is $q(2.25\ \text{eV}) = 97\%$.

9. Each deposited green photon will create one electron-hole pair, as this is normal for a CCD interacting with a visible light photon, [94].

10. The resulting number of counts recorded for each of the electron-hole pairs created depends on the analogue-to-digital converter. Its details are shown in figure 3.18. The number of counts for each green photon is then given by the factor ADC.

11. So the number of counts (c) given for a certain number of incident photons (N_p) for a pixel of the CCD array is then given by this expression:

$$c = N_p \frac{I(S')}{E_{2.25eV}} \cdot g \cdot \alpha \cdot q(2.25\text{eV}) \cdot \text{ADC} \tag{3.12}$$

12. This expression can be simplified into the factors which do not depend on the incident x-ray radiation spectrum (M') and the integral $I(S')$.

$$c = N_p \cdot I(S') \cdot M' = N_p \cdot M \tag{3.13}$$

3.2.4 Princeton PIXIS Camera System Calibration

As the values of the phosphor energy conversion efficiencies (g) and the fibre coupling efficiencies (α) for each pixel were not precisely known. It was necessary to calibrate the system using a source of known brightness.

Conversion Gain (e-/ADU) and Non-Linearity			
Mode	**Gain setting**	**(e-/ADU)**	**Non-Linearity**
Low-Noise Output (LNO)			
LNO 100 kHz	1	3.58	<2%
	2	1.85	<2%
	3	0.90	<2%
LNO 2 MHz	1	3.89	<2%
	2	1.98	<2%
	3	1.05	<2%
High-Capacity Output (HCO)			
HCO 100 kHz	1	14.99	<3%
	2	7.54	<3%
	3	3.97	<3%
HCO 2 MHz	1	16.52	<3%
	2	8.01	<3%
	3	4.55	<3%
Read Noise (e- rms)			
Mode		**Speed**	**Measured**
Low-Noise Output (LNO)		100 kHz	4.29
Low-Noise Output (LNO)		2 MHz	14.85
High-Capacity Output (HCO)		100 kHz	7.90
High-Capacity Output (HCO)		2 MHz	36.21
Dark Charge (e-/pixel/sec)			
	Measured		
	0.1 @ -30 degree Celsius		

Figure 3.18: The ADC settings for the Princeton PIXIS system. Reproduced from Princeton Instrument's unique calibration.

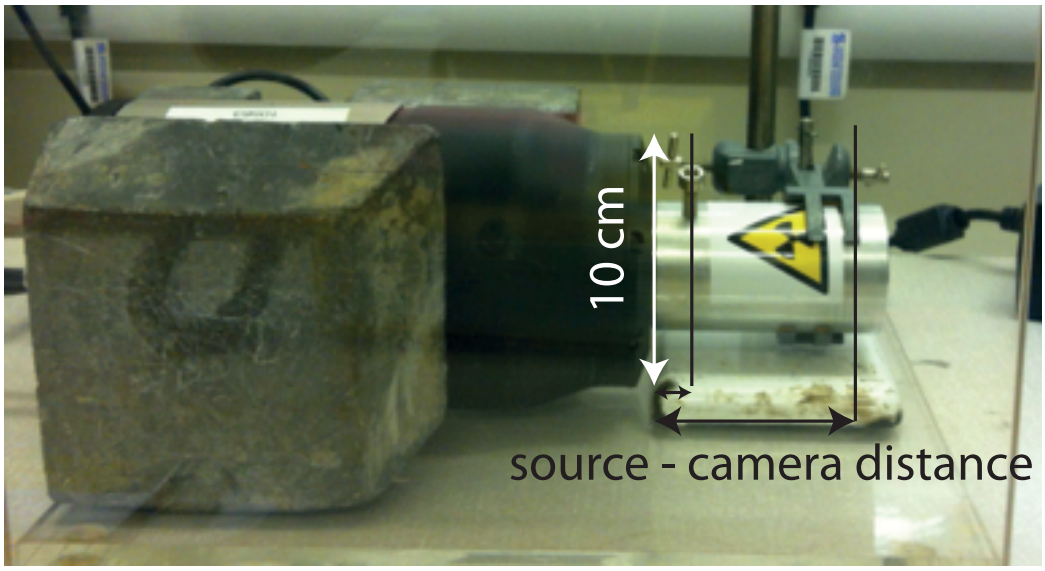

Figure 3.19: Photo of calibration setup with approximate scale.

The calibration was carried out at the Rutherford Appleton laboratory using a Fe-55 disk source of 11 mm diameter, and an activity of 2.5926 MBq at the time of the calibration. The camera was placed in contact with the source holder and a number

of 30 min (1800 s) exposures were taken. This length of exposure was necessary to yield an appreciable signal on the camera. A number of 1800 s background exposures were also taken without the source present.

It is necessary when using the system to conduct a pixel by pixel subtraction using an appropriate background image. This due to the noise levels in each pixel not being uniform across the CCD array but varying reproducibly for each pixel. The results of this subtraction are shown in figure 3.20. One can notice that in figure 3.20c) there is a hexagonal grid pattern in the data. This is due to the optical fibre design, and is normal.

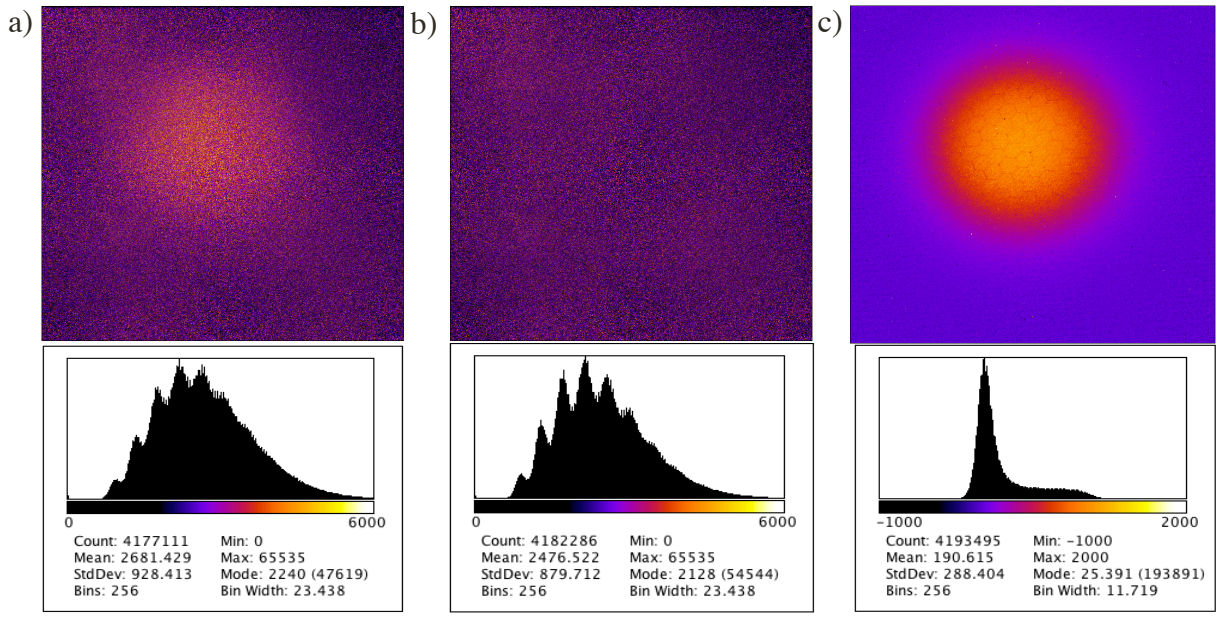

Figure 3.20: Exposure to Fe-55 for 1800 s. b) Exposure with no source present. c) A pixel by pixel subtraction of a) from b). The images above show the camera counts. The histograms below show the exact colour tables used for the images above.

The shape of the distribution seen in 6c) is typical of the distribution produced by a disk source of radiation. From Smith et al.1954 [95] the following expression for this off-axis distribution ($D(z, a, \epsilon)$) of a disk radiation source is given:

$$D(z, a, \epsilon) = \int_0^a \int_0^{2\pi} G(R)S(\rho)\rho d\rho d\theta \tag{3.14}$$

The geometry is shown in figure 3.21. a is the source radius. G(R) is the response of the detector at distance R from the disk. $S(R)$ is the source strength per unit area,

in this case 2.5926 MBq / $(2\pi a^2)$. ρ and θ are the polar coordinates on the disk. z is the perpendicular distance of the detector to the source. ϵ is the distance from the axis of the disk to a point on the detector. R is the distance of a point on the disk to a point of the detector, given by the expression:

$$R = (z^2 + \rho^2 + \epsilon^2 - 2\epsilon\rho\cos\theta)^{1/2} \tag{3.15}$$

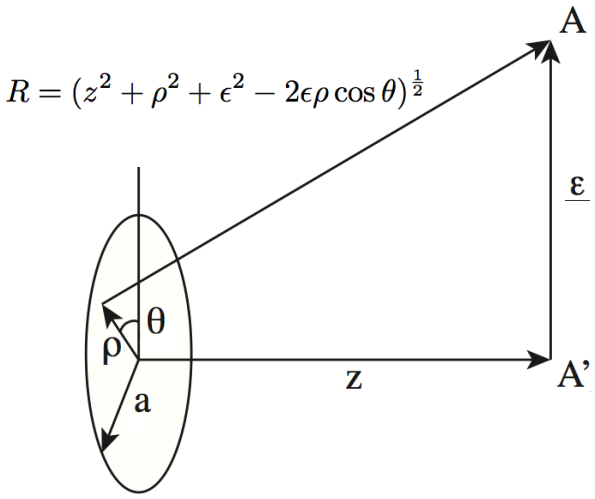

Figure 3.21: The geometry used for the off axis distribution of a disk radiation source.

In the case of a detector such as the Princeton PIXIS camera system the response $G(R)$ varies with solid angle. As the solid angle is reduced, by the angle between the vector R and the normal of the camera increasing, the camera response will decrease. This results in:

$$G(R) = \frac{z}{4\pi R^3} \tag{3.16}$$

This can be substituted into the integral and solved numerically. It is important to do this as the on axis distribution, which is the centre of the distribution in figure 3.20c), will differ from that of a point like source if z is not very much greater than a. A point like source would be expected on axis to vary as: $D = a^2/(4z^2)$. The difference is shown in figure 3.22.

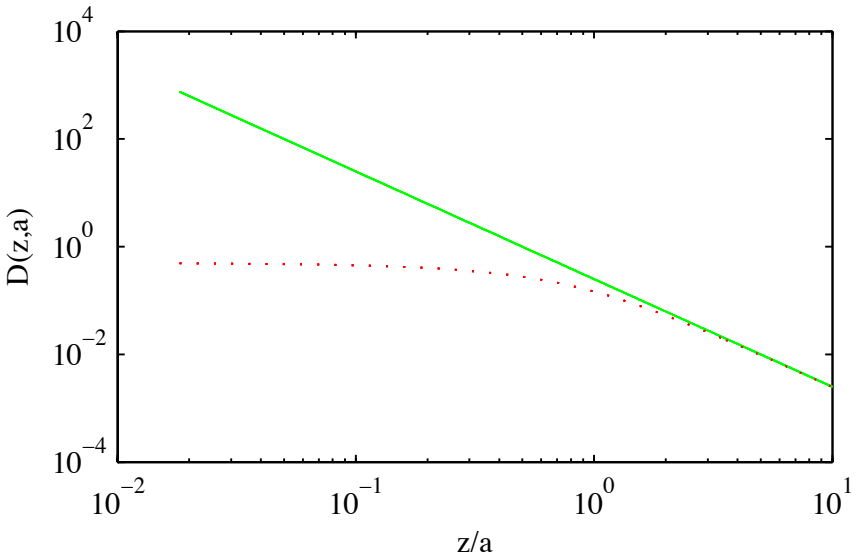

Figure 3.22: The on axis distribution due to a point like source (green line) and the on axis distribution for a disk source (red dotted line).

Unfortunately the distance between the front of the camera and the radiation source (z) could not be measured. This is because the Fe-55 source was too dangerous to examine and the distance of the disk from the front of the enclosure is not known.

However, because the off axis distribution changes in shape with changes to the distance z, as is shown in Figure 3.23, it was possible to numerically solve for $D(z, a, \epsilon)$ and iteratively fit the constant M and the distance z.

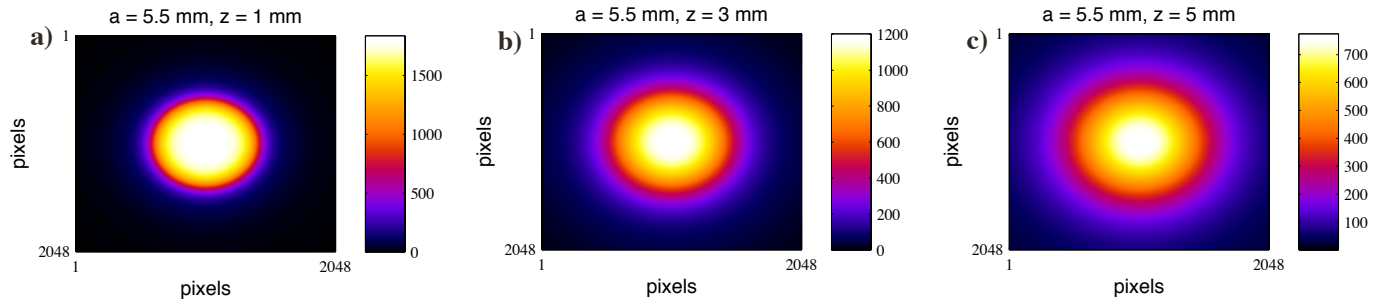

Figure 3.23: Calculation of the off axis distribution of radiation for a uniform disk source of 2.5926 MBq activity radius 5.5 mm, placed at distance z from a pixel detector with the same pixel size and dimensions as the Princeton PIXIS system. The distribution was calculated numerically and in this case the constant M (defined above) has been set to one. a) z = 1 mm. b) z = 3 mm. c) z = 5 mm.

The iterative fitting algorithm found z = 3.11 mm and M = 0.942. This value of z is consistent with the set up shown in figure 3.19 and this value of M is also consistent with reasonable values of the unknown constants mentioned above. The results of the fit are shown in Figure 3.24 and can be seen to be in good agreement with the experimental data.

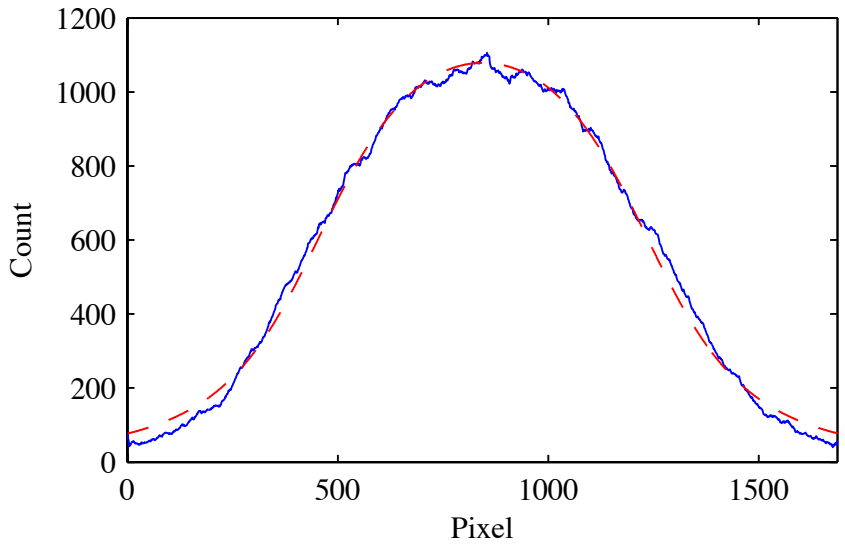

Figure 3.24: Blue Solid Line: A lineout through the centre of the signal due to exposure to the Fe-55 source for 1800 s after a pixel by pixel background subtraction. Red Dashed Line: The off axis distribution calculated with fitted values of z=3.11 mm and M = 0.942 for a uniform 2.5926 MBq activity disk source of radius 5.5 mm, 1800 s exposure.

Recalling the expression of counts due to photon number:

$$c = N_p \cdot I(S') \cdot M' = N_p \cdot M \tag{3.17}$$

The calibration factor M contains the spectrally dependent term $I(S')$ and the spectrally independent term M'. In order to calibrate the system's response to an arbitrary x-ray spectrum S' the constant M' must be found. To do this the integral $I(S')$ must be assessed for the Fe-55 spectrum.

$$I = \int T(E)Q(E)S(E)EdE \tag{3.18}$$

The decay of Fe-55 is via electron capture to Mn-55. The result of this is a rapid adjustment in the electrons around the nucleus and a vacancy in the 'K' shell, which

is usually filled by an electron from a higher shell. There are a variety of ways the excess energy from this process may be emitted via Auger electrons or x-rays of differing energy and probability. However the x-rays energies are so similar they can be specified as mono-energetic radiation of 5.9 keV, [96]. Thus $S'(E) = \delta(E - 5.9keV)$

The transmission of 5.9 keV x-rays through 3.11 mm of air is found from reference values [91], yielding $T(E) = 0.992$. The quantum efficiently of the Csl:TI scintillator for 5.9 keV photons can be assessed from Figure 3.17 as $Q(5.9keV) = 0.899$. Thus I(Fe-55) = 5.26 keV/Photon. So $M' = 0.1791$ counts/keV .

So furnished with an accurate calibration of the Princeton PIXIS system, it is now possible to calculate incident photon number on the system with accurate knowledge of the spectral shape function of the radiation.

Chapter 4

Laser Wakefield Acceleration Experiments with the Lund Multi-TW Laser

For this experiment a multi-TW CPA laser system at the Lund Laser Laboratory (LLC) located in Sweden was used, which delivered 18 TW to target.

Wavelength λ_0 (nm)	Pulse Energy (J)	Pulse Duration τ_0 (fs)	Repetition Rate (shots per min)
800	0.6	45	>1

In this chapter the threshold for electron self injection in a self guided LWFA, a parameter critical for both electron and x-ray generation.

4.1 Experimental Set Up.

The general set up is best described by figure 4.1. The laser beam is focused onto the edge of a supersonic gas jet using an f/9 off-axis parabolic mirror. A range of nozzles was available for the gas jet to examine the guiding properties. In practice the measurements were made with both a 2mm and 3mm diameter nozzle,[97].

A permanent magnet based electron spectrometer was set up inside the vacuum chamber using a Lanex screen and CCD imaging system to record the electron spectrum. The magnet was placed on a translation slide so that it could be moved out of the beam line-of-sight, allowing measurements of the electron beam profile.

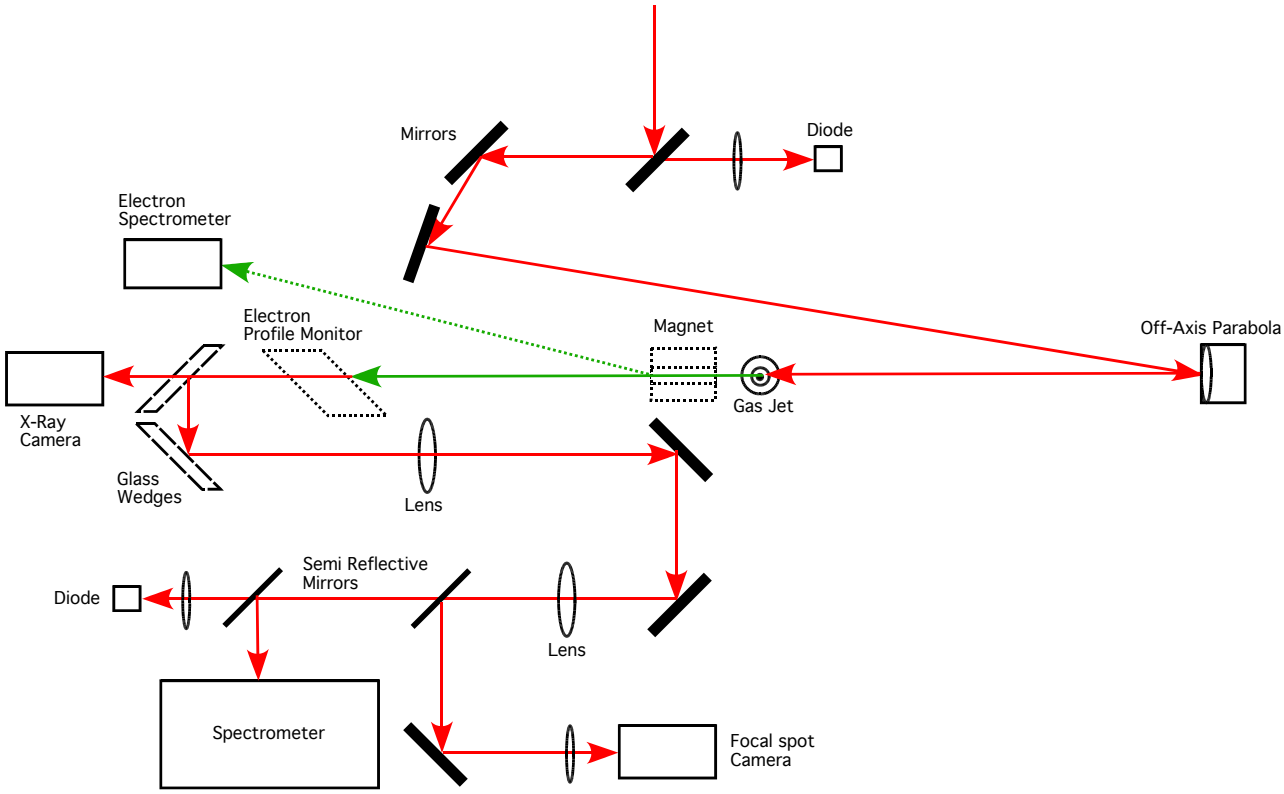

Figure 4.1: The experimental set up for the Lund Laser Lab experiment.

To characterize the guiding, the transmitted laser light was attenuated using two glass wedges before being collected. A magnified image of the exit mode was then recorded on a high dynamic range CCD camera and simultaneous measurement of the transmitted laser spectrum was also recorded. Filters centred around 800nm were used. In addition calibrated measurements of the transmitted laser energy were made using diodes both before and after the interaction.

An x-ray CCD camera was set up on the laser axis able to operate either as a filter transmission spectrometer or in single-photon mode (to provide a high resolution spectrum in a single shot). This is to characterize the x-ray spectrum produced by betatron oscillations of the electron beam.

Through a clever arrangement of the glass wedge, and two Lanex screens of different sizes on a rotation stage it was made possible to operate the experiment in three modes without the need to break vacuum:

1. To measure a portion of the electron spectrum while simultaneously running the x-ray camera. This was achieved through diverting the electrons via the magnet (into a aluminium backed sheet of Lanex) which allowed the laser and subsequent betatron x-rays to pass unobstructed.

2. To take a full image using Al backed Lanex of either the electron spectrum with the magnet in or the electron profile.

3. To use the glass wedge to take measurements on the forward line diagnostics and record the electron spectra or profiles utilizing a Lanex screen mounted on the rear of the glass wedge. (Here it would be expected that glass would filter out the lower energy electrons).

Additionally, use was made of the relatively long fluorescence life time of Lanex, see Buck 2009 [98]. By gating the image taking in the spectrometer to a few microseconds after the interaction, elaborate light shielding was made unnecessary.

Variation of electron density of the plasma.

Electron density in the plasma was varied through changing the backing pressure of the gas feed line before the super sonic gas jet. The resulting density profiles were found offline (but in situ) through use of a Wollaston interferometer using neutral argon gas.

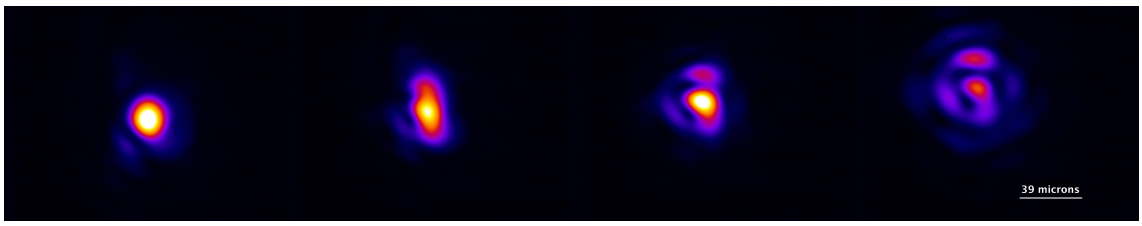

Figure 4.2: Focal spot images recorded with increasing amounts of spherical aberration. From left to right the intensity contained in the FWHM is (a) 47%, (b) 40%, (c) 31%, (d) 20%.

Variation of Energy in FWHM focal spot.

The focal spot quality of the laser and subsequently the energy in FWHM of the focal spot were controlled using the 32 actuator deformable mirror and wave-front sensor available at LLC. Using this system not only could the focal spot quality be maximised but known aberrations could be approximated at focus. Figure 4.2 shows some of the focal spot profiles used.

Variation of focal spot size.

This was achieved through changing a lens before the off axis parabola. This allowed the beam diameter on the parabola to be changed and so subsequently the size of the of the beam at focus to be increased.

Variation of the power of the laser pulse.

This was varied through changing the pulse length by moving the compressor gratings, thus allowing the total energy of the pulse to remain the same but change the power. A side effect of this is to introduce (chromatic) chirp into the pulse, where the wavelength varies linearly over time. Both directions of grating movement were used in order to create positive and negative chirp, positive chirp having shorter wavelengths at the leading edge of the pulse. This also causes skew in the pulse where the electric field gradient varies more quickly on the leading or falling edge of the pulse depending on which direction the gratings are moved in.

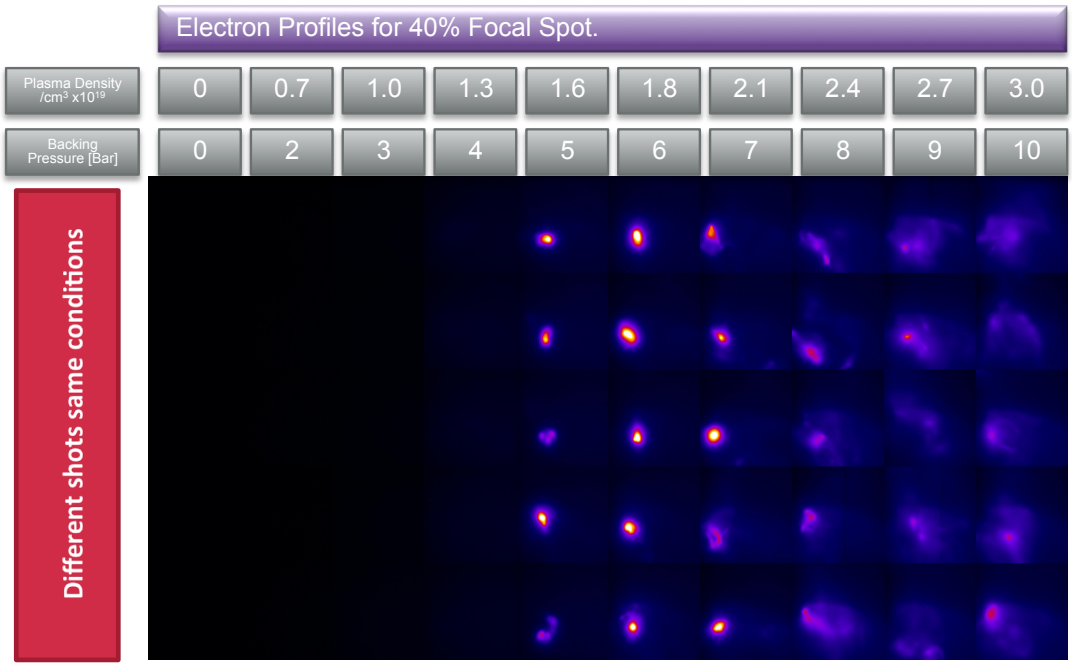

Figure 4.3: Measurements of the electron beam profile for different plasma densities for $\alpha = 0.40$. The colour table is linear and in arbitrary units. A threshold for injection is clearly visible between densities of 1.3 and 1.6 x 10^{19} cm^3.

The total energy of the laser pulse.

The total energy of the laser pulse was varied though changing the number of pump lasers in the CPA system. Through reducing the number of lasers pumping each amplification stage a number of different energies could be produced.

4.2 Examining the energy-density threshold for wavebreaking

As already mentioned in section 4.2.1 in the highly non-linear regime there is a threshold plasma density below which no electron beams are produced. In this section the effects of laser pulse duration τ_0, laser energy E_0 and the laser energy α in the FWHM of the laser spot on this density threshold are examined.

From measurements of the electron beam profile monitor (Figure 4.3), it is clear that the threshold for wavebreaking has, as expected, a dependence on plasma density.

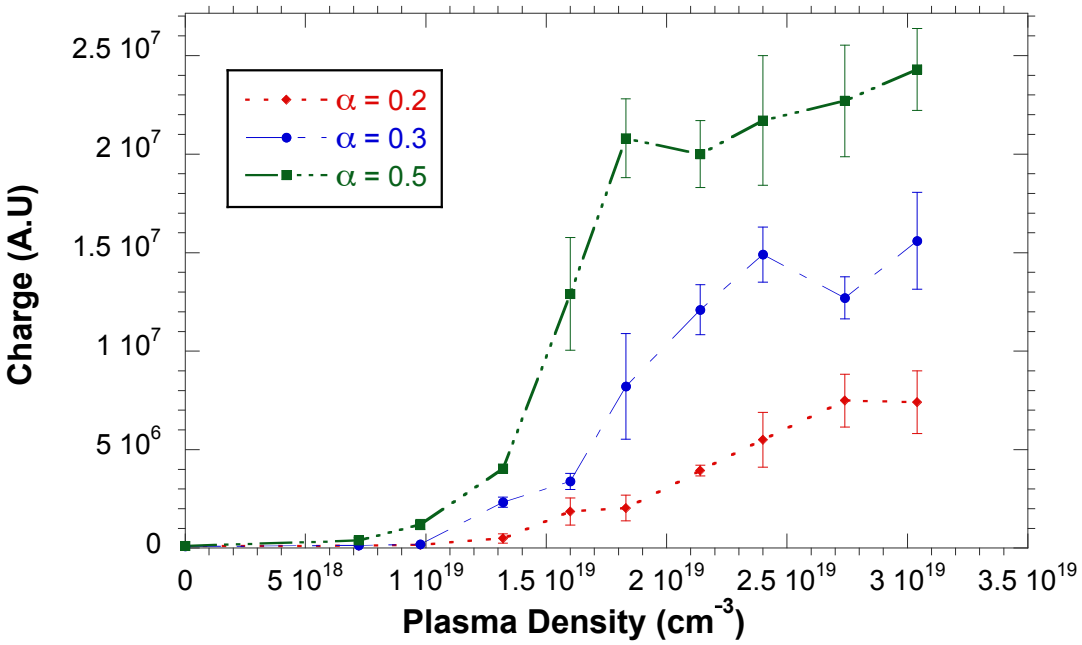

Figure 4.4: The recorded charge for the different focal spot qualities (α) for different plasma densities (n_e).

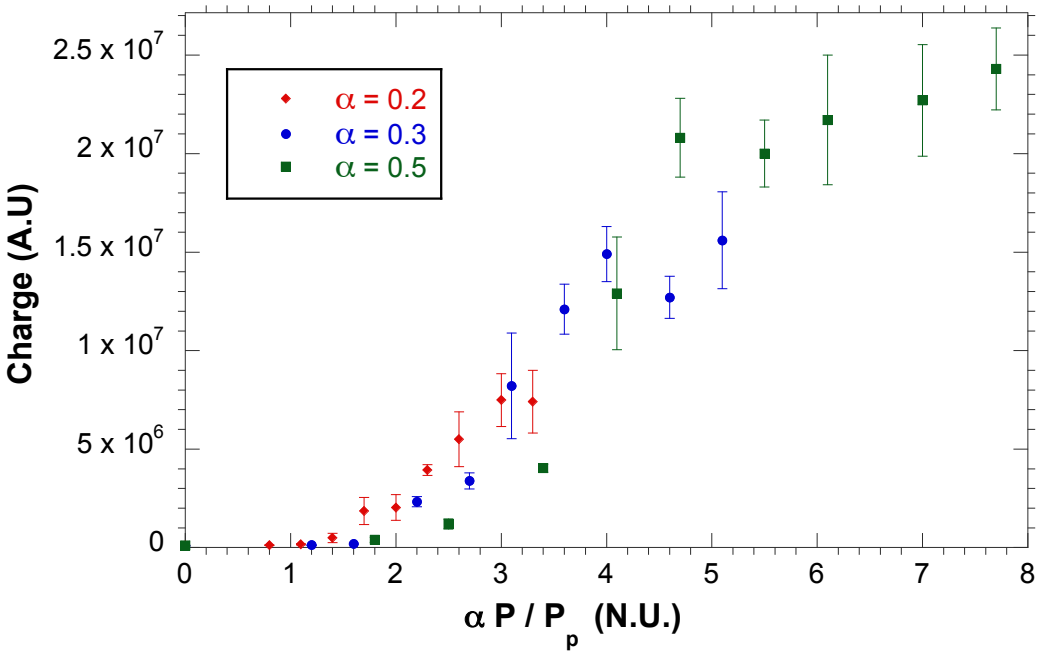

Figure 4.5: The recorded charge for the different focal spot qualities (α) plotted against the power in the FWHM of the pulse as a ratio of power for self focusing ($\alpha P/P_p$).

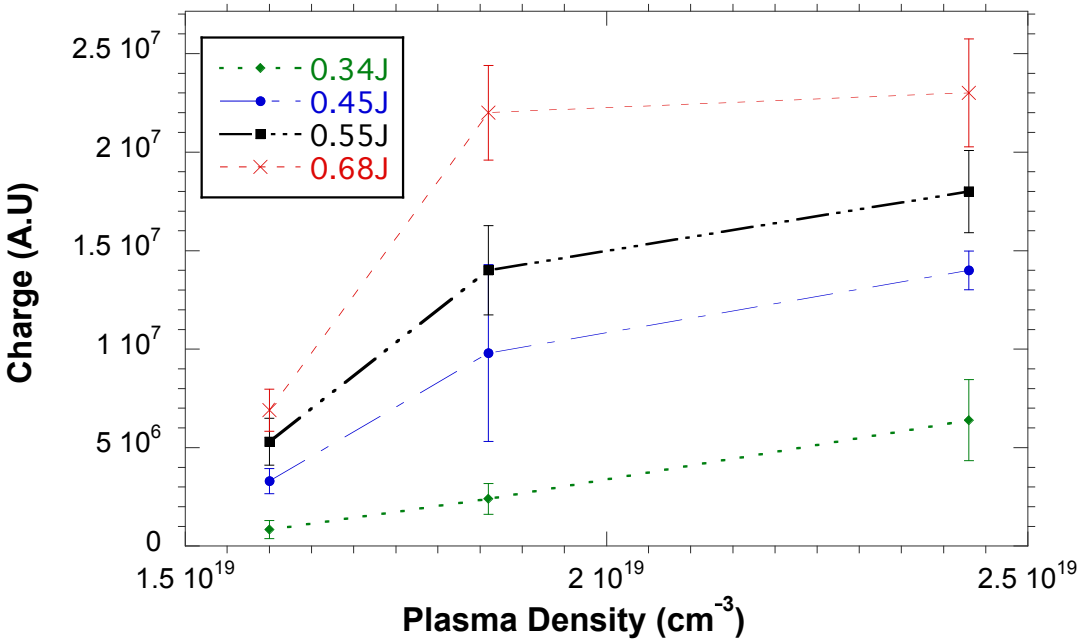

Figure 4.6: The recorded charge for the different laser energies against different plasma densities (n_e). $\alpha = 0.47$.

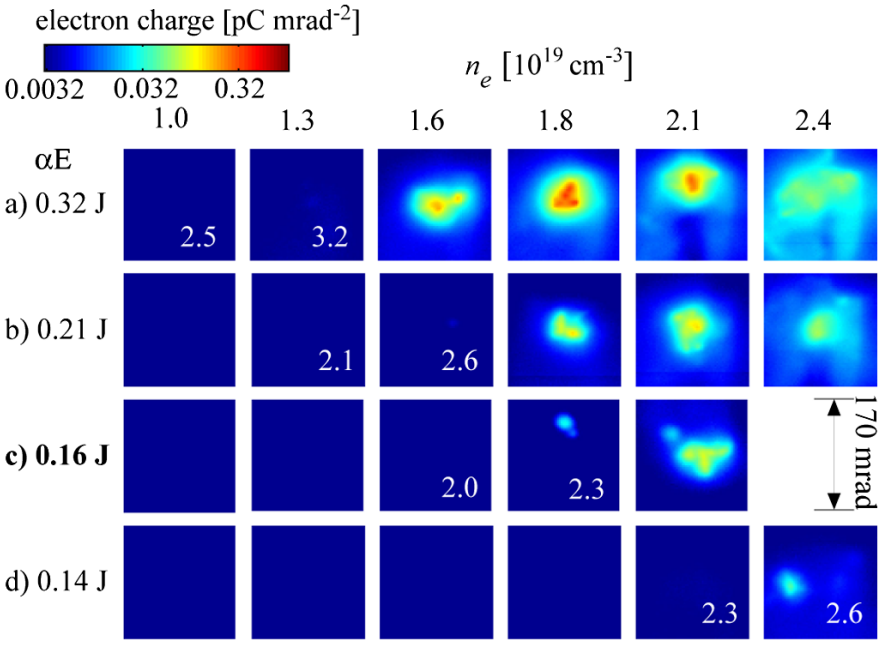

Figure 4.7: Electron beam profiles for various plasma densities for different values of the amount of laser energy within the FWHM of the focal spot α. Each panel is an average of five shots and is displayed on a logarithmic color scale. (a), (b), and (d) kept the total laser energy E constant but varied α whereas (c) reduced the laser energy E. (I made this figure, which was first published in Mangles, Bloom, et al. 2012 [99]. Reproduced under creative commons licence.)

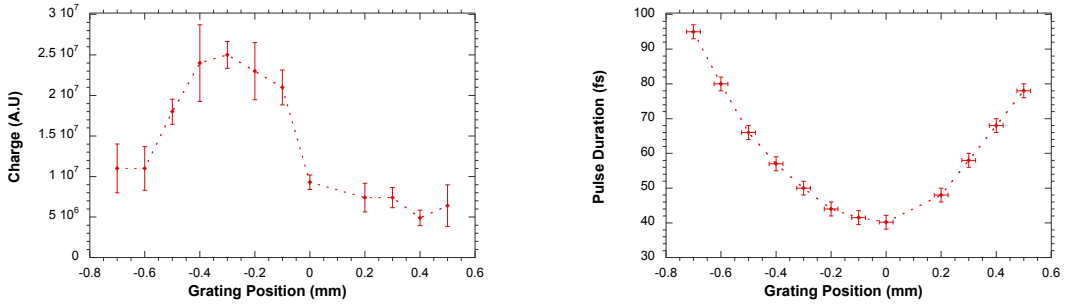

Figure 4.8: (Left) This is the recorded charge on the electron profile monitor for when the position of the compressor gratings is varied. (Right) The pulse duration measured using a "GRENOUILLE" against grating position.

Above 1.3 $\times 10^{19}$ cm^{-3} clear electron beams are present. However there are arguably clearer beams with higher charge and small divergence at 1.8 $\times 10^{19}$ cm^{-3} than at 1.6 or 2.1 $\times 10^{19}$ cm^{-3}.

The quality of the focal spot was varied as set out in the previous section and figure 4.4 shows the results of this study. In this graph, as it will be for all the figures in this section, each point represents the average of 5 shots and the error bars are representative of the standard deviation of these results. The charge shown for each profile measurement is simply the total number of CCD counts across the electron beam profile monitor.

From figure 4.4 it is clear that as the quality of the focal spot (α) is lowered the amount of charge on the profile is reduced. Here one can identify for the $\alpha = 0.5$ beam at pressure 1.8 $\times 10^{19}$ the hight point representing the clearer beams with higher charge and small divergence shown in figure 4.3[1]. An important thing to note is that at higher plasma densities the beam quality clearly deteriorates in figure 4.3 with multiple beamlets appearing. However in figure 4.4 you can see that though the beam quality is poor at these high densities the amount of charge is equivalent or greater than for the good quality beam.

In order to compare the data from the different focal spots it is useful to compare their power. In doing so its not a bad idea to normalise to the critical power for self

[1]The data is actually from $\alpha = 0.47$ in figure 4.4 and $\alpha = 0.40$ in figure 4.3. But the results for $\alpha = 0.40$ were so close to $\alpha = 0.47$ (0.5) that they have been omitted from figure 4.4. The two spots can be viewed in figure 4.2.

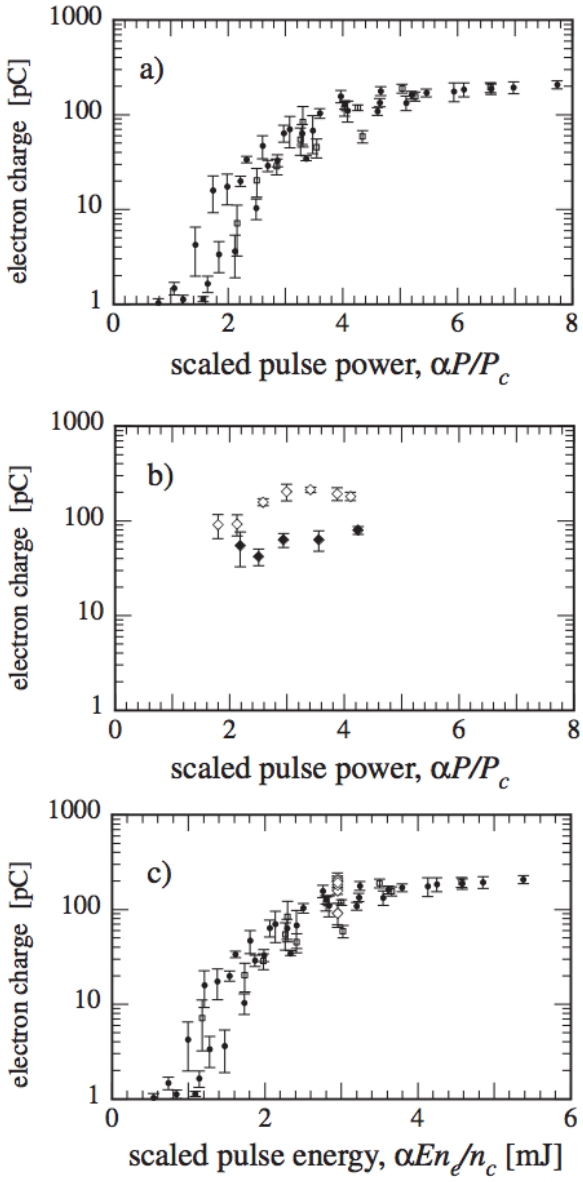

Figure 4.9: (a) Electron charge (>4 MeV) versus $\alpha P/P_c$ keeping the pulse duration constant but varying the focal spot quality α and the plasma density n_e (closed circles) or total pulse energy E, and plasma density (open squares) but keeping the pulse duration constant τ_0. (b) Electron charge versus $\alpha P/P_c$ varying pulse duration τ_0 while keeping plasma density n_e and energy in focal spot αE constant. (c) Data from (a) and (b) plotted versus $\alpha E n_e/n_c$. Each data point is an average of five shots and the error bars represent 1 standard deviation. (I made this figure, which was first published in Mangles, Bloom, et al. 2012 [99]. Reproduced under creative commons licence.)

focusing P_c which is in turn dependent on the plasma density[2]. This is done in figure 4.5. Here one can see that there is a clear trend.

The effect of changing the energy of the laser pulse as a function of density is shown in figure 4.6. This when plotted against $\alpha P/P_c$ as seen in figure 4.9 this data can also be seen to follow the same trend as the variation of focal spot quality.

Through variation of the compressor grating distance the pulse length (τ) was changed. The resulting pulse length was evaluated using a "GRENOUILLE"[3]. This effect is shown in figure 4.8 (b). It can been seen that counter to expectations the amount of accelerated charge actually increases at positions away from the grating's zero position; the position where the pulse is at its shortest and known as bandwidth limited. As shown on figure 4.9 the charge is optimised for a positively chirped pulse of 50 fs opposed to the bandwidth limited pulse of 41 fs. This effect was actually first reported by Leemans in 2002 [100], in which it was theorised that the electric field gradient at the front of the pulse was the necessary factor. This would indicate that is not in fact a power threshold as in figure 4.9 (a).

In figure 4.9 (c) the data from (a) and (b) is plotted as a function of energy $\alpha E n_e/n_c$ not power. The variation of pulse length fits better in this case indicative of an energy threshold.

4.2.1 Model of The Self-Injection Threshold in Self-Guided Laser Wakefield Accelerators.

The highly nonlinear broken wave regime is used in many experiments to produce quasimonoenergetic electron beams and is used in the experiments presented in this thesis. In such experiments a threshold plasma density is commonly observed, below which no electron beams are produced. In section 2.3.3 the cold wave-breaking limits were discussed. However they did not take into account the 3D field structures dependences on driving laser pulses.

Because of the inverse scaling of the electron beam energy with plasma density n_e, the highest energy beams achievable with a given laser system are achieved just

[2] $$P_c = \frac{8\pi\epsilon_0 m_e^2 c^5 \omega_0^2}{e^2\omega_p^2} \approx 17\frac{\omega_0^2}{\omega_p^2}\mathrm{GW}$$

[3] A "GRENOUILLE" is a device which operates utilising a similar principle to a frequency resolved optical grating F.R.O.G. .

above the threshold, and it is well known that many of the beam parameters including the spectrum and stability are also optimized just above the threshold density. This therefore makes this parameter of key importance to x-ray as well as electron generation by LWFAs. The threshold is also of importance if designing a LWFA to not self inject. In which case one would have to operate below the threshold.

The first period of the plasma wave behind the laser pulse in a LWFA can be thought of as a spheroid or bubble devoid of background plasma electrons travelling at $\gamma_{\phi p}$ behind the laser pulse. In the paper Kostyukov et al. 2004 [101] field equations are derived for the electric and magnetic field present in a spherical cavity moving through a plasma at relativistic velocities. In the paper Thomas et al. 2010 [102] it is shown using these fields that electrons initially at rest following near elliptical velocities due to the ponderomotive force of the laser will be accelerated to $\gamma_{\phi p} m_e c^2$ if the radius of the plasma bubble is larger than

$$k_p r_b > 2\sqrt{ln(2\gamma_{\phi p}^2)} \tag{4.1}$$

The paper Decker et al. 1996 [103] finds

$$\gamma_{\phi p}^2 \simeq \frac{n_c}{3n_e} \tag{4.2}$$

for the Lorentz factor associated with the phase velocity of the bubble, (in contrast to 2.55). In Lu et al. 2007 [104] the following relation between laser power $\alpha E/\tau$ and the matched bubble size is shown:

$$k_p r_b = 2\sqrt{2}\left(\frac{\alpha E}{\tau P_c}\right)^{1/6} \tag{4.3}$$

However the laser pulse duration $\tau(l)$ changes from the initial pulse duration entering the plasma τ_0 as a function of the propagation length l. The paper Schreiber et al. 2010 [105] presents a simple model for the rate of the pulse compression:

$$\tau(l) \simeq \tau_0 - \frac{l n_e}{2 c n_c} \tag{4.4}$$

However pulse compression can not continue after the pulse has passed the pump depletion length,

$$L_{pd} \simeq \frac{\tau_0 c n_c}{n_e} \tag{4.5}$$

Combining together these equations the following expressions for the threshold for electron self injection are reached. Depending on if the LWFA is longer or shorter

than the pump depletion length one or the other should be used.

$$\begin{aligned} \alpha E > & \frac{\tau_0 P_c}{16}\left[\ln\left(\frac{2n_c}{3n_e}\right)-1\right]^3 \\ & \text{for } l > L_{pd} \\ \alpha E > & \left(\tau_0 - \frac{l n_e}{2 c n_c}\right)\frac{P_c}{8}\left[\ln\left(\frac{2n_c}{3n_e}\right)-1\right]^3 \\ & \text{for } l < L_{pd} \end{aligned} \tag{4.6}$$

This expressions were then tested against experiment as will be discussed in the relevant chapters.

A previous study in Froula et al. 2009 [106] showed that, at low density, the threshold is approximately

$$\frac{\alpha P}{P_c} < 3 \tag{4.7}$$

A pure power dependence. This can be rearranged to similar form as the model developed in 4.6 above.

$$\alpha E > 3\frac{\pi \epsilon_0 m_e^2 c^5}{e^2}\frac{n_c}{n_e}\tau_0 \tag{4.8}$$

This alternate model will be contrasted with 4.6.

4.2.2 Comparing The Self-Injection Threshold Model With The Experiment.

In section 4.2.1 a model for the self injection threshold was presented along with a competing theory, given in equations 4.6 and 4.8 respectively. Figure 4.10 shows the two predictions along with the thresholds observed in this experiment due to variation of αE. The energy threshold is in good agreement to observation as opposed to the power threshold.

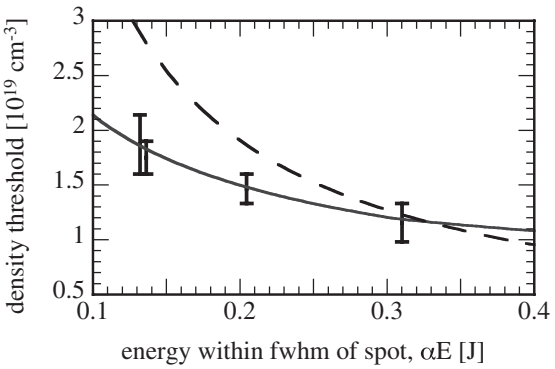

Figure 4.10: Observed electron density threshold for self injection as a function of laser energy (αE). The solid curve represents the model discussed in section 4.2.1 given by equation 4.6. The dashed curve represents the alternate threshold model given by 4.8.

Chapter 5

Laser WakeField Acceleration and Betatron X-Ray Generation Using the Astra Gemini Laser

The experiment described in this chapter used the Astra Gemini laser at the Rutherford Appleton Laboratory, UK. This two beam line laser was designed to deliver 15 J pulses with a duration of 30 fs onto the desired target, and so have a peak power of 500 TW. The focusing optic used is a f/20 one metre off-axis parabolic mirror which would be capable of producing intensities on target greater than 1.5 $\times 10^{20}$ Wcm^{-2}. As this corresponds to a normalised vector potential of $a_0 > 5$, the motion of electrons in this laser field will be highly relativistic.

The initial motivation for using such a laser to study electron acceleration was as an extension of previous work producing betatron x-rays from self-guided wakefield regime using the Hercules laser [69] where a peak power of 70 TW was used. The results of the last experiment were encouraging as we saw x-rays of peak brightnesses of 10^{22} ph/s/mm^2/mrad^2/0.1% bandwidth at critical energies of 10 keV, and sources sizes of between 1 and 3 μm which we demonstrated could be used for phase contrast imaging.

It was of great interest to see what x-rays would be produced by the more powerful laser as existing scalings predicted a large increase in the accelerated electron energies and so could produce both brighter and harder x-rays.

5.1 Experimental Set-Up

At the time of the experiment, the Astra Gemini laser delivered pulses of 10J on target with pulse durations of 55 fs, and peak power of 180 TW. An f/20 off axis parabolic mirror was used to focus these pulses onto the edge of a supersonic gas jet, producing intensities of 5×10^{19} Wcm, corresponding to a normalised vector potential of $a_0 \sim 3$. The nozzles used were high density conical nozzles with a range of entrance orifices producing plasma densities between 10^{18} to 10^{19} cm^{-3} depending on the backing gas pressures used. Only the nozzles with 10 and 15 mm entrances will be discussed here. They produce constant density regions of 8.5 and 11.5mm diameter respectively in their centres with sharp density ramps around their edges. The gas used was helium, as the laser pulse intensity is well above the threshold for ionisation one can expect the gas to be fully ionised long before the main pulse of the laser arrives. The nozzles were calibrated before the experiment by carrying out interferometry using argon gas, this was later confirmed by observed Raman satellites in an imaging system set up transversely to the laser propagation direction.

Figure 5.1 shows the experimental layout of the target vacuum chamber and diagnostics. The principal diagnostics which will be described here were a two screen magnetic spectrometer used in measuring the energy spectrum of the accelerated electrons which is described in chapter 3.1.1, and Csl:TI scintillator, fibre optically coupled to a CCD array which is the Princeton PIXIS system described in chapter 3.2.3 and used to measure the x-rays produced when combined with the filter packs discussed in section 3.2.1.

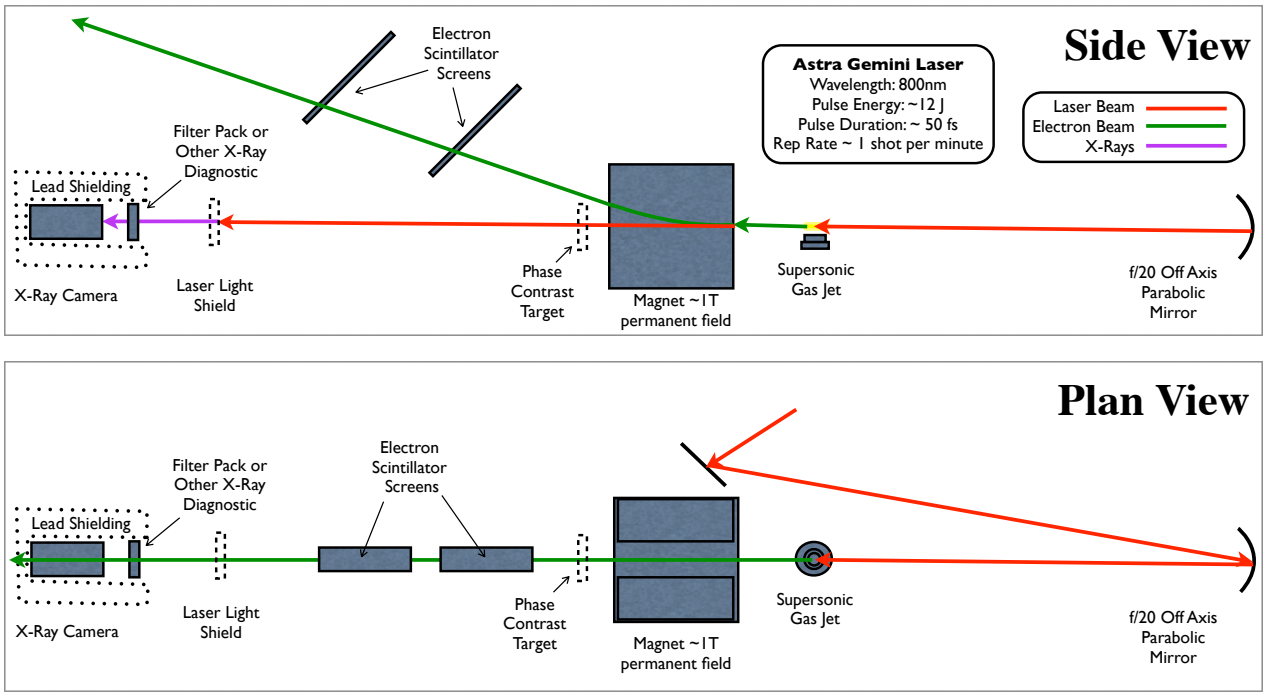

Figure 5.1: Experimental layout showing the laser beam path and the separation of the electron beam from the x-ray beam.

Previous experiments found that measurements of the betatron x-rays were obscured by bremsstrahlung gamma rays produced by the electron beam meeting objects within the experimental chamber or the chamber wall. Therefore this experiment was designed to avoid this in the following ways:

- A magnet was used with a high magnetic field to deflect the electrons by a large angle away from the x-ray path. The electron spectrometer was not fitted with collimating apertures as they would produce bremsstrahlung. Instead the two screen spectrometer technique described in section 4 was used which does not require collimating apertures. The c-shape magnet design allows for electrons to pass through without striking the yoke, further reducing bremsstrahlung production.

- The distance of the electrons flight before exiting the vacuum chamber was maximised thereby making the distance of the x-ray detector from the electrons point of impact on the vacuum chamber as large as possible.

- Lead shielding was placed in-between the x-ray detector and the point of impact of the electrons on the vacuum chamber.

- The Al vacuum chamber was fitted with a low-z polymer flange at the electrons impact point in order to minimise the bremsstrahlung produced.
- Inside the chamber the electrons flight path was kept as clear as possible with only the electron scintillator screens in their path. These screens were intentionally kept as thin as possible while remaining light tight, through the use of an aluminised mylar layer, and maintaining a thick enough Lanex layer to ensure good signal on the electron spectrometer.

These precautions together avoided the betatron x-rays from being obscured by bremsstrahlung radiation as was the case in previous experiments I have conducted.

A microscope objective could be lowered into place, and the gas jet removed, to record the focal spot of the laser, in vacuum; this in conjunction with motorised mirrors and the off-axis parabolic mirror being motorised allowed for the focus of the laser to be optimised while in vacuum. A top view camera was also set up above the interaction to image the whole plasma, and was useful for alignment.

In addition to the diagnostics mentioned, a probe beam was set up to image the plasma transversely, and carry out interferometry. An imaging system could be inserted in front of the x-ray diagnostic in order to image the exit mode of the laser from the plasma and also passed to an energy measuring diode. Data from these diagnostics won't be discussed here, however they did allow for confirmation that a wake field was being produced, and on shot verification of how the laser energy was being deposited into the plasma as a function of changing the backing gas pressure.

For data taking, shots could be taken around every 40s, limited mainly by the speed at which gas could be pumped out of the chamber. Images from the x-ray camera and two electron spectrometer screens were available immediately after each shot. This combined with crude image processing done immediately allowed for the experimental parameters to be searched to optimise both the x-ray production and electron beam energies.

5.2 3D Momentum Distributions of GeV Electron Beams

High-energy electron beams were produced over a range of plasma densities. The electron beam typically produced significant features on the electron spectrometer

screens due to betatron oscillations of the electron beam. Example scintillator screen images are shown in figures 5.2 and 5.3.

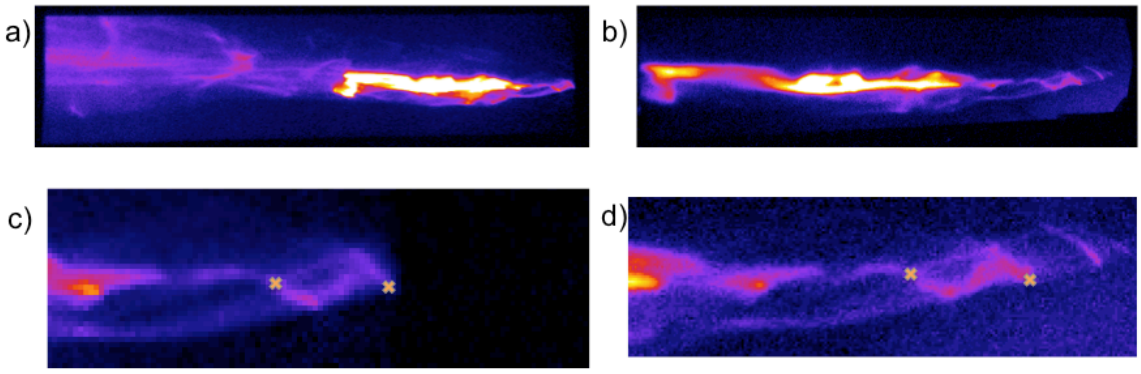

Figure 5.2: Raw images of electron spectrometer scintillator screens. Images from a) screen 1 and b) screen 2 for a shot at $n_e = 5 \times 10^{19}$ cm^{-3} and a 10 mm gas jet nozzle, c) and d) show a smaller region. The marked point on the right corresponds to 1.34 $\pm$ 0.07 GeV electrons at an angle of 3 mrad. The marked point on the left corresponds to 1.09 $\pm$ 0.04 GeV at an angle of -1 mrad.

Figure 5.2 shows the images from screens 1 and 2 for a shot at an electron plasma density of 5×10^{18} cm^{-3}, laser energy after amplification of 10.1 J, and a LWFA length of 10 mm, and results of the reconstruction method is shown. The error in this measurement was assessed: it was found that effects of positional error were greater than those from other sources such as the accuracy of the magnetic field measurement. By propagating the errors in the position for the screens, gas jet, plasma, magnet, and the human error in choosing clearly identifiable features in the spectra maximum bounds were found for s_1 and s_2; these maximum bounds were used in the reconstruction algorithm in order to find the limits shown in the reported error. Electrons were observed at energies as high as 1.34 ± 0.07 GeV on this shot. There are also features closer to the spectrometer axis that missed the first screen. The higher energy end of this spectrum shows clear betatron oscillations, responsible for the generation of bright x-rays.

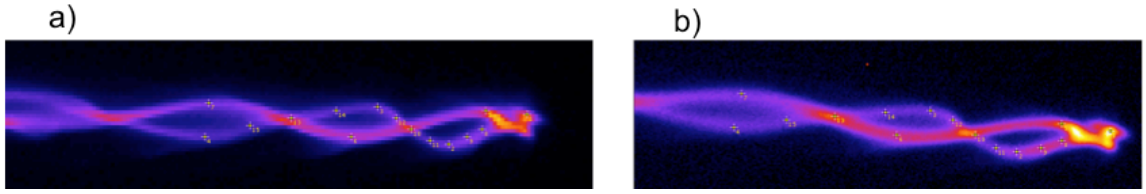

Figure 5.3: Raw images of electron spectrometer scintillator screens. Images from a) screen 1 and b) screen 2 for a shot at $n_e = 2 \times 10^{18}$ cm^{-3} and a 15 mm gas jet nozzle. The marked points have their momentum components p_x , p_y and p_z plotted in figure 5.

Figure 5.3 shows images of the two scintillator screens for a shot at an electron plasma density of 2×10^{18} cm^{-3}, a laser energy of 11.3 J, but using a 15 mm diameter supersonic nozzle. This shot appears to show two interleaving beamlets. We have analysed the full 3D momentum distribution of a set of points for one of these beamlets. This is shown in figure 5.4.

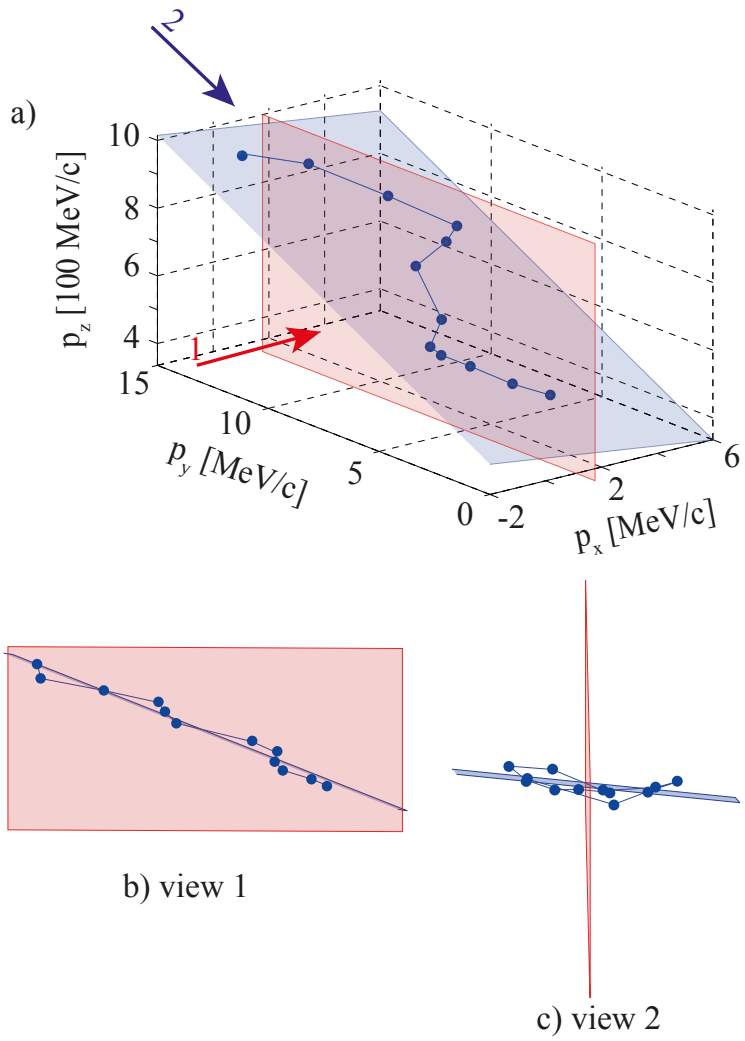

Figure 5.4: a) Three dimensional momentum distribution of one of the beamlets shown in figure 5.3. The blue points are 3D momentum coordinates of the identified features in the beam. The blue plane is the "plane of best-fit" to these points. The red plane corresponds to the laser electric field direction. Two additional views are shown (without axes) taken along the direction of the red and the blue arrows. b) shows the view along the red arrow (1), highlighting the head-to-tail tilt of the beam; c) shows the view along the blue arrow (2). This is a direction almost tangential to the red and blue planes, showing that the electrons are approximately distributed in a plane that is approximately at 90° to the laser electric field direction.

The three dimensional momentum information about this beamlet shows that the oscillation is approximately confined to a plane and that this plane is almost 90 degrees to the laser electric field direction, i.e. the strong betatron oscillations are

not due to interaction with the laser field. As to the apparent small oscillations out of the "plane of best fit" visible in figure 5.4, due to experimental uncertainty it is not possible to say if they are significant. There is a clear correlation between p_z and p_y, which can be interpreted as a "head-to-tail" tilt. Such tilts can be responsible for hosing instabilities in beam driven plasmas wakefield accelerators [107].

Preliminary simulations with Osiris do show that for extended plasma lengths the laser can be sufficiently depleted for the interaction to enter a "beam driven"phase (i.e. one where the electron beam itself drives a wakefield). However the resulting hosing does not show interleaving features in the electron beam. Such features are observed earlier in the interaction when the bubble undergoes rapid expansion due to modification of the laser strength by self-focusing, pulse compression and photon deceleration.

We have successfully fielded a two-screen spectrometer capable of measuring electron beams with energies greater than 1 GeV on Astra Gemini, having observed beams with features up to 1.34 ± 0.07 GeV. The two-screen method allows the full three dimensional momentum distribution of the beam to be examined which provides insight into the dynamics of electron injection and acceleration, vital for understanding the processes responsible for beam instabilities and x-ray generation.

5.3 A Model For The Electron Energy As Function Of Density Including The Pre-Injection Pulse Evolution Length

Changing the background density of the plasma has a profound effect on the type of electron spectra generated in the LWFA, and subsequently the betatron x-rays generated. Figure 5.5 a) shows the electron spectra produced during a series of shots where the plasma density was altered. Each shot shown is representative of the behaviour of the LWFA at this density. A qualitative transition is noticeable in the type of electron spectra, below $n_e \sim 4 \times 10^{18}$ cm^{-3} the beams are well collimated, with a divergence of > 20 mrad, above $n_e \sim 4 \times 10^{18}$ cm^{-3} the beams are more diffuse, the beam divergence is significantly larger (> 50 mrad) and significant transverse structure is observed in the beam profile.

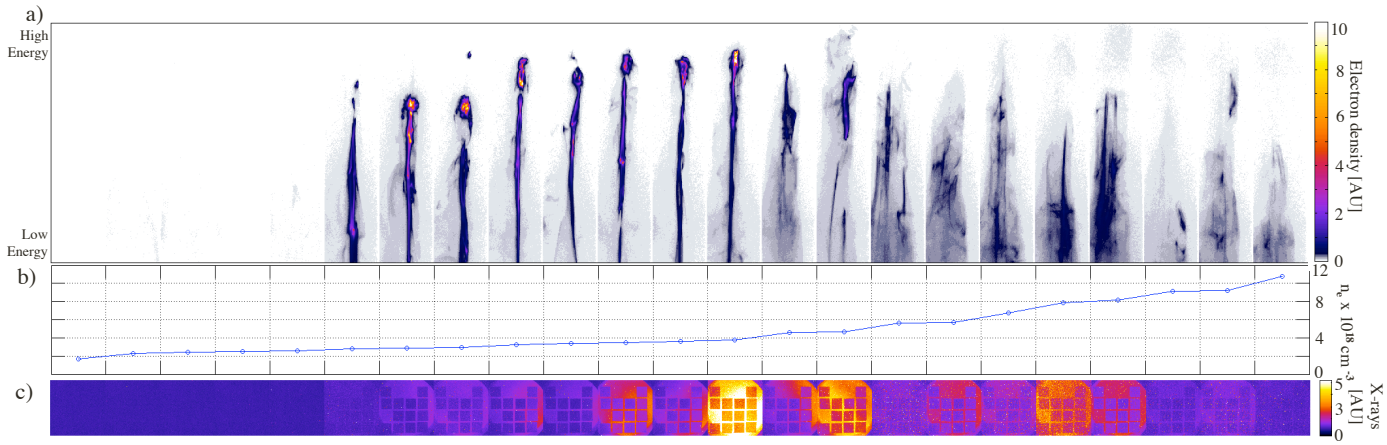

Figure 5.5: The data from 24 shots of the laser, using the 10 mm nozzle, is shown in order of increasing density (from left to right) a) Shows the images from one of the electron spectrometer screens. The electrons to the top of the images have been deflected less by the magnet and have a higher energy. b) Shows the plasma densities of each of these shots. c) The images from the Princeton PIXIS x-ray camera for each shot are shown.

In understanding why this change in spectral type occurs, we can consider some key lengths associated with laser wakefield accelerators. First there is a length of plasma at the beginning of the accelerator over which the laser pulse is still evolving, (self focusing and compressing in time), and the wakefield has not yet formed in such a way to allow for electron self injection. I will call this the pre-injection pulse evolution length (or PIPE Length). After self-injection has occurred (or started) the electrons are accelerated for some length, L_{ACC}. In practice this length is often limited by either the length of the plasma, L_{PLASMA}, or the length over which the laser pulse propagates before its energy is depleted to the extent it can no longer produce an accelerating wakefield, L_{ETCH}. Finally the dephasing length L_ϕ is important, this is the length over which an electron injected at the back of the wakefield bubble, will be accelerated enough, and have a long enough time of flight, to reach the centre of the bubble where the electric fields reverse and the electron will start to be decelerated. The relationship between L_{ACC} and L_ϕ will have a strong effect on the type of electron spectra emerging from the LWFA.

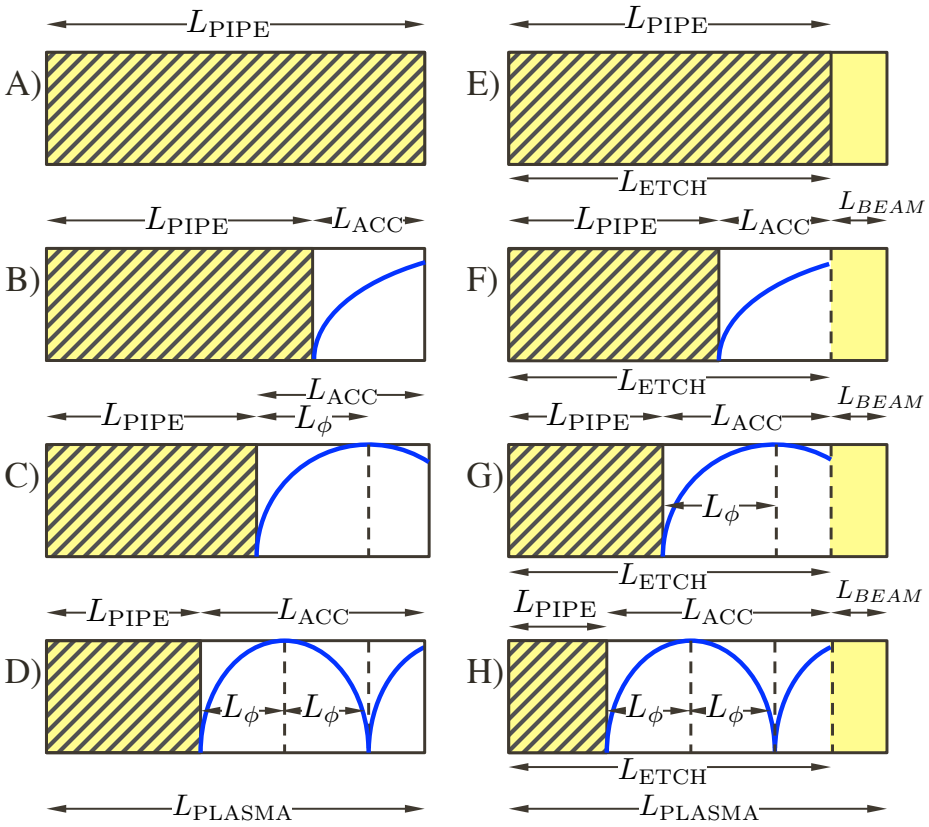

Figure 5.6: The illustration shows the various scenarios which can occur in a LWFA due to differing ratios between the lengths L_{PLASMA} , L_{ETCH}, L_{ACC}, L_{ϕ} and L_{PIPE}, (not to scale). The blue line represents the energy of an electron self injected at the beginning of L_{ACC}, and demonstrates the effect of L_{ϕ} on such an electron. (However in D and H the energies shown are for a idealised simplified symmetric series of wakefield periods which doesn't take into account the presence of the laser pulse, the plasma between wakefield periods or that the LWFA my be in a bubble regime.) A, B, C and D are limited by the plasma length L_{PLASMA}, whereas E, F, G and H are the same but limited instead by the laser depletion length L_{ETCH}.

Essentially all these lengths have a dependence on the plasma density n_e as well as the initial laser pulse conditions. Figure 5.6 shows the various possible scenarios dependent on the ratio of these lengths. Scenarios A, B, C and D are all limited by the plasma length, whereas E, F, G and H are the same but limited instead by the laser depletion length. Scenarios F, G and H differ from B, C and D as the accelerated electrons may go on to drive a wakefield of their own. This beam driven wakefield can lead to further electron acceleration, Chen 1985 [108]. The electron beam propagating

through the plasma (over length L_{BEAM}) can also be affected by instabilities, such as the current filamentation instability Huntington 2011 [109] which can drastically change the electron spectrum which is measured outside of the plasma. The cases of A and E are trivial as the laser pulse never evolves to drive a plasma wave capable of self injection. In the case of B and F the acceleration length ends before electrons injected at the beginning of the acceleration length can dephase, and so the maximum achievable electron energy is not reached.

The transition of the fifth shot to the sixth shot in figure 5.5 (Counting from left to right), corresponds to a transition from A to B in figure 5.6 (or E to F), and represents the threshold for self injection in a LWFA.

One possible explanation for the transition from collimated beams to diffuse spectra, seen between shots 12 and 13 in figure 5.5, is a transition from scenario B to F in figure 5.6 (or possibly a transition from C to G)). To assess this a simple model of the pipe length's dependence on plasma density has been developed.

5.3.1 A Simple Model Applied To Maximum Achievable Electron Energy In The LWFA

Simple models of L_{ETCH} and L_ϕ already exist in the literature Lu 2007 [104].

$$L_{\mathrm{ETCH}} = \tau_0 c \frac{n_c}{n_e} \tag{5.1}$$

and

$$L_\phi = \frac{2}{3} R \frac{n_c}{n_e} \tag{5.2}$$

where R is the bubble radius and τ_0 is the duration of the laser pulse before entering the plasma.

To try and find a very simple model of how the PIPE length scales with plasma density I tried the following:

$$L_{PIPE} = S \frac{n_c}{n_e} \tag{5.3}$$

where S is just a linear constant. This simple model completely ignores the initial laser pulse parameters such as power, pulse duration, spot size and wavelength which should play a role in pulse evolution, however it may be useful in comparing LWFAs where the input laser pulse is the same. Indeed in what follows I hope to demonstrate to the reader that this is the case.

Let us now consider what the maximum energy E_m an electron can be accelerated to in a given LWFA scenario. If the electron beam is considered as an ensemble of electrons with different energies, E_m will be the upper limit of the energies contained in the ensemble. E_m will not necessarily be the mean energy of the electrons contained in the ensemble, though it is possible for these energies to be the same, e.g. through phase rotation. E_m is the energy an electron which was initially at rest in the bubble frame, and at the back edge of the bubble will be accelerated to, if it remains in the bubble until it reaches the centre of the bubble, and is not decelerated by dephasing.

A generally used scaling expression for the maximum achievable energy gain of a single stage LWFA [104] is,

$$\gamma_{max} = \frac{2n_c}{3n_e} a_0 \tag{5.4}$$

However a_0 as considered in vacuum is an underestimation of the laser pulse's normalized vector potential in the plasma, as self focusing and temporal pulse compression act to compress the pulse in both space and time. The a_0 after these effects can be estimated as:

$$a_{max} = 2\left(\frac{P_F}{P_C}\right)^{1/3} \tag{5.5}$$

where $P_F = \alpha E/\tau_F$. The energy in the laser pulse's FWHM is αE, and τ_F is the FWHM laser pulse duration after plasma pulse compression given by:

$$\tau_F = \tau_0 - \frac{n_e}{n_c}\frac{L}{c} \tag{5.6}$$

Where L is the length over which compression happens and τ_0 is the initial pulse duration.

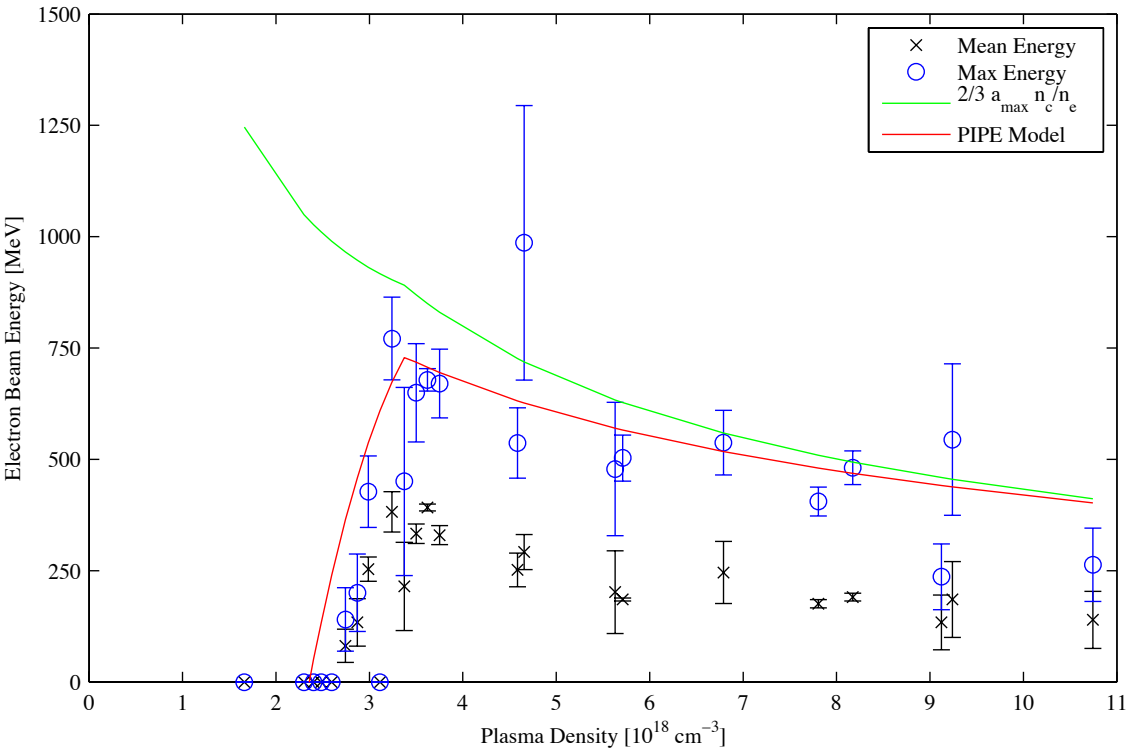

Figure 5.7: Variation of electron beam energy with density for the 10mm nozzle. In blue are shown the upper limit of the electron's energy spectra for a number of shots at each plasma density. The blue circles are the mean value of the upper energy limit of these shots. The bars shown are the standard error about the mean. In black are shown the mean electron energy in the spectra. The black crosses are the mean of multiple shots. The bars again show the standard error about the mean. In green is shown the prediction of equations 5.4, 5.5 and 5.6. The red line shows the prediction of the simple model taking into account the PIPE length.

Figure 5.7 shows details of electron beams from multiple shots at different densities. The upper limit of the electrons energy spectrum is shown by the blue circles and shows good agreement with the prediction of equation 5.4 when equation 5.5 and 5.6 are used (shown by the green line in figure 5.7).

However this assumes electrons are able to travel at least one dephasing length. In practice the PIPE length reduces the effective acceleration length L_{ACC}.

$$L_{ACC} = L_{INT} - L_{PIPE} \tag{5.7}$$

where L_{INT} is either the total length of the LWFA (8.5 mm for the 10 mm gas jet

nozzle used in this experiment) or the pump depletion length, which ever is shorter. Due to the non-linear interplay between the processes of self-focusing, pulse compression, energy depletion and photon deceleration and their role in determining the wake amplitude I have not found a simple expression for the PIPE length, however as a first approximation, it is reasonable to assume that the rate of evolution will be inversely proportional to plasma density, so I assume that the pipe length scales as:

$$L_{PIPE} = S\frac{n_c}{n_e} \tag{5.8}$$

And assuming that inside the bubble the fields are linearly increasing from the centre, [110]. So:

$$\gamma = \gamma_{max}(2\frac{L_{ACC}}{L_\phi} - \frac{L_{ACC}^2}{L_\phi^2}) \tag{5.9}$$

We find that if the coefficient $S \approx 11.5$ mm, the PIPE model (shown in red) corresponds to the experimentally recorded results in figure 5.7.

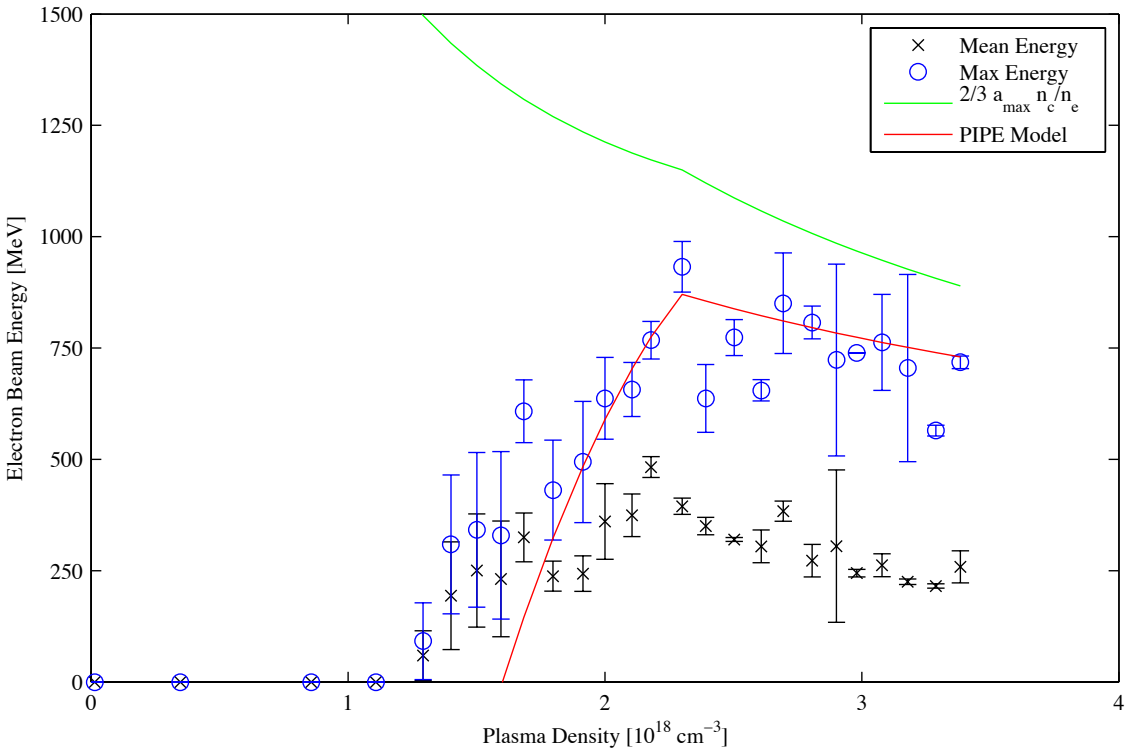

Figure 5.8: Variation of electron beam energy with density for the 15 mm nozzle. In blue are shown the upper limit of the electron's energy spectra for a number of shots at each plasma density. The blue circles are the mean value of the upper energy limit of these shots. The bars shown are the standard error about the mean. In black are shown the mean electron energy in the spectra. The black crosses are the mean of multiple shots. The bars again show the standard error about the mean. In green is shown the prediction of equations 5.4, 5.5 and 5.6. The red line shows the prediction of the simple model taking into account the PIPE length.

Interestingly if we take this value for S and apply it to data taken using the same setup with a 15 mm gas jet nozzle we see a similar correlation. This is shown in figure 5.8

Scenario	n_e	L_{PIPE}	L_{ACC}	L_ϕ	L_{ETCH}	L_{PLASMA}	L_{BEAM}
	cm^{-3}	mm	mm	mm	mm	mm	mm
A	1.0×10^{18}	20.0	0.0	*20.1	28.7	8.5	0.0
B	3.3×10^{18}	6.1	2.4	4.6	8.7	8.5	0.0
C	2.4×10^{19}	0.8	0.4	0.3	1.2	1.2	0.0
E	1.0×10^{18}	20.0	0.0	*20.1	28.7	30.0	0.0
F	3.8×10^{18}	5.3	2.3	3.8	7.6	8.5	0.9
G	2.4×10^{19}	0.8	0.4	0.3	8.5	1.2	7.3

Figure 5.9: The table shows which scenario shown in figure 5.6 the simple model predicts will occur for various plasma densities and plasma lengths, for S = 11.5 mm. The laser parameters used are those of the experiment. *Scenarios A and E are trivial because no electron acceleration occurs. So the dephasing length has no real meaning.

Using this very simple model one can see that it is possible to enter several of the scenarios shown in figure 5.6 by just changing the plasma density and the length of the wakefield accelerator. The table in figure 5.9 shows which scenario this model predicts will occur for various plasma densities and plasma lengths. Scenarios D and H are not shown in the table because they are not accessible with these laser parameters. Importantly the transition from scenario B to scenario F can be seen to occur at a plasma density near to where, in the experimental data of figure 5.5, the electron spectra change shape from well collimated beams to diffuse. So confirming this as the most likely explanation of the change in spectral shape.

5.4 X-Ray Measurements

Using the Princeton PIXIS system, x-ray measurements were taken with the 10 mm nozzle. As discussed in the experimental methods section both the peak x-ray brightness and the critical energy of the x-ray spectrum could be found. Figure 5.10 shows the variation of peak x-ray brightness with changes to the background plasma density. For the calculation of brightness a source size of 1 μm has been assumed. This is because on shot measurements of the source size was not possible on this series of shots. However this size is consistent with the x-ray source size measurements taken during the same experiment. The temporal duration of the x-ray beam is assumed to be 55 fs, the same as the driving laser pulse FWHM. In reality this is merely the upper limit of the x-ray temporal duration, which may reasonably be less than 10 fs, so the figures shown for peak x-ray brightness may be an underestimation.

In figure 5.10 one can see the average peak x-ray brightness consistently varies between two and three $\times 10^{24}$ photons per photons per second per mrad^2 per mm^2 per 0.1% bandwidth over the plasma density region of 3 to 5 $\times 10^{18}$ cm^{-3}. This statistical trend is roughly correlated with the mean electron beam energy average at these densities also shown in figure 5.10. It also shows correlation with the average maximum electron beam energy shown in figure 5.11. Though they are statistical outliers, the brightest shots at each density are of physical importance. They indicate that given the right conditions x-ray brightnesses of as great as 10^{25} photons per second per mrad^2 per mm^2 per 0.1% bandwidth can be achieved, corresponding to $\sim 10^{10}$ photons incident on our camera per shot.

My hypothesis, centred around the scenarios of figure 5.6, is as follows: Generally in the region of 3 to 4 $\times 10^{18}$ cm^{-3} the accelerator is transitioning from scenario B to F (plasma length limited to pump depletion length limited). This is due to the pipe length shortening due to increasing plasma density as discussed in section 5.3. However occasionally, as in the case of these outlying shots, the pipe length is significantly shorter leading to scenario C or G occurring at these background plasma densities. This leads to betatron x-ray emission happening over a longer electron path length both before and after dephasing, thus resulting in a larger x-ray yield. I believe this pipe length shortening must be as a result of changes in the laser wavefront resulting in a faster pulse evolution. (This is illustrated in figure 5.12).

Using the filter pack method, described in the methods section, the hardness of the x-rays was measured on each shot. This can be best parameterised as a single number the critical energy of a synchrotron like spectrum, (The value at which half the energy of the spectrum is contained within photons that have energies greater than this value). The results of this measurement are shown in figure 5.13 .

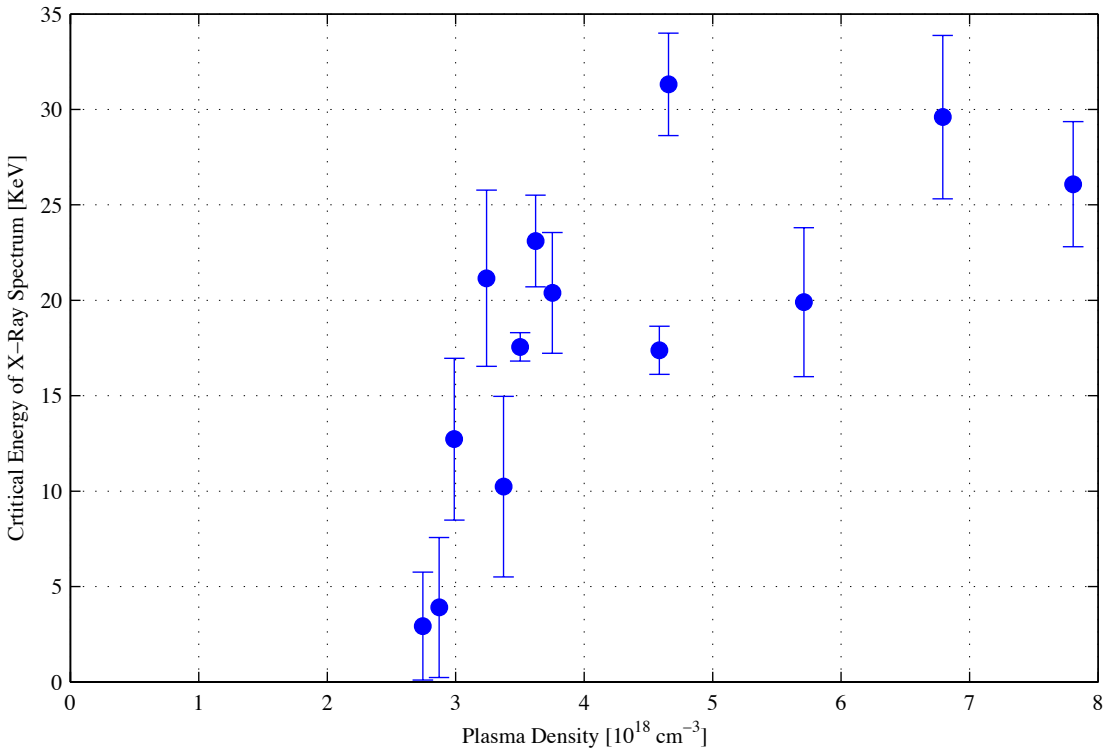

Figure 5.13: The average measured x-ray spectrum critical energy for multiple shots at different plasma densities. A synchrotron like spectrum is assumed (see section 3 for more details). The error bars show the standard error about the mean.

One can see that after the initial ramp up of both electron energy and x-ray brightness which occurs at plasma densities less than 3.5×10^{18} cm^{-3}, the critical energy of the x-ray spectrum is consistently between 15 and 25 keV. So the x-rays are both hard and bright. At higher plasma densities (4.5×10^{18} cm^{-3}) though both the mean electron energy and x-ray brightness somewhat decrease the critical energy of the spectrum appears to increase.

This is not all that surprising as the critical energy is expected to vary as in the following equation ([90], [111], [112]):

$$E_c = \frac{3\hbar}{4c}\gamma_e^2\omega_p^2 r_\beta \tag{5.10}$$

Where r_β is the betatron radius: the amplitude of the electrons' oscillation. ω_p^2 will increase linearly with plasma density. Besides we cannot be sure that the recorded mean electron energies are accurate representations of the energy is reached inside

the accelerator for these densities, as for these densities the electron beam is certainly propagating through a length of plasma without a laser Wakefield, and so may be effected by instabilities such as the current filamentation instability [109]. Thus the electron energies inside the accelerator may be greater than those measured outside at these densities. This would explain the increase in critical energy at higher densities and may mean that, if higher energy x-rays are required, working at even higher densities with decreased accelerator length may be the preferable option.

In summary high brightness hard x-rays were seen with critical energies varying between 15 keV and 30 keV and peak brightnesses between 10^{24} and 10^{25} photons per second per mrad^2 per mm^2 per 0.1% bandwidth. A strong correlation between the x-ray brightness and electron beam energy was seen. The variation of x-ray brightness with plasma density is explained by the transition of the laser Wakefield accelerator from scenario B to scenario F (the acceleration length limited by the plasma length to the acceleration length limited by the pump depletion length). The brightest shots are explained if the pipe length is unusually short, potentially due to unmeasured changes in the laser wave front, which cause the acceleration length to be unusually long or to enter scenarios C and G (which are like B and F but the acceleration length passes dephasing).

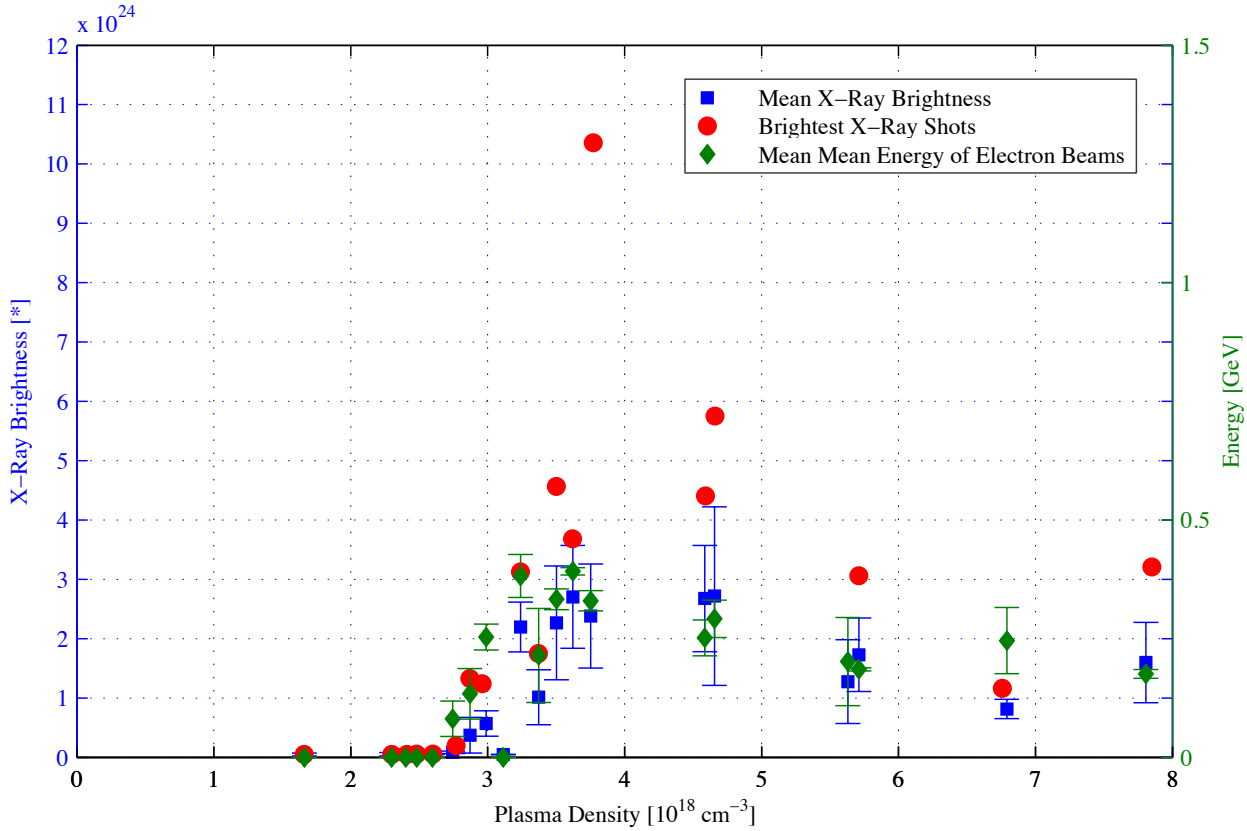

Figure 5.10: Blue: The average peak x-ray brightness of multiple shots at each density. *The units of brightness are photons per second per mrad^2 per mm^2 per 0.1% bandwidth. A source size and 1 μm is assumed, and the x-ray pulse duration is assumed to be 55 fs. The error bars show the standard error about the mean. Red: The peak x-ray brightness of the brightest shots at each density. The error in each individual measurement is smaller than the circle shown. Green: The average of multiple shots' electron beam mean energy. The error bars shown are the standard error about the mean.

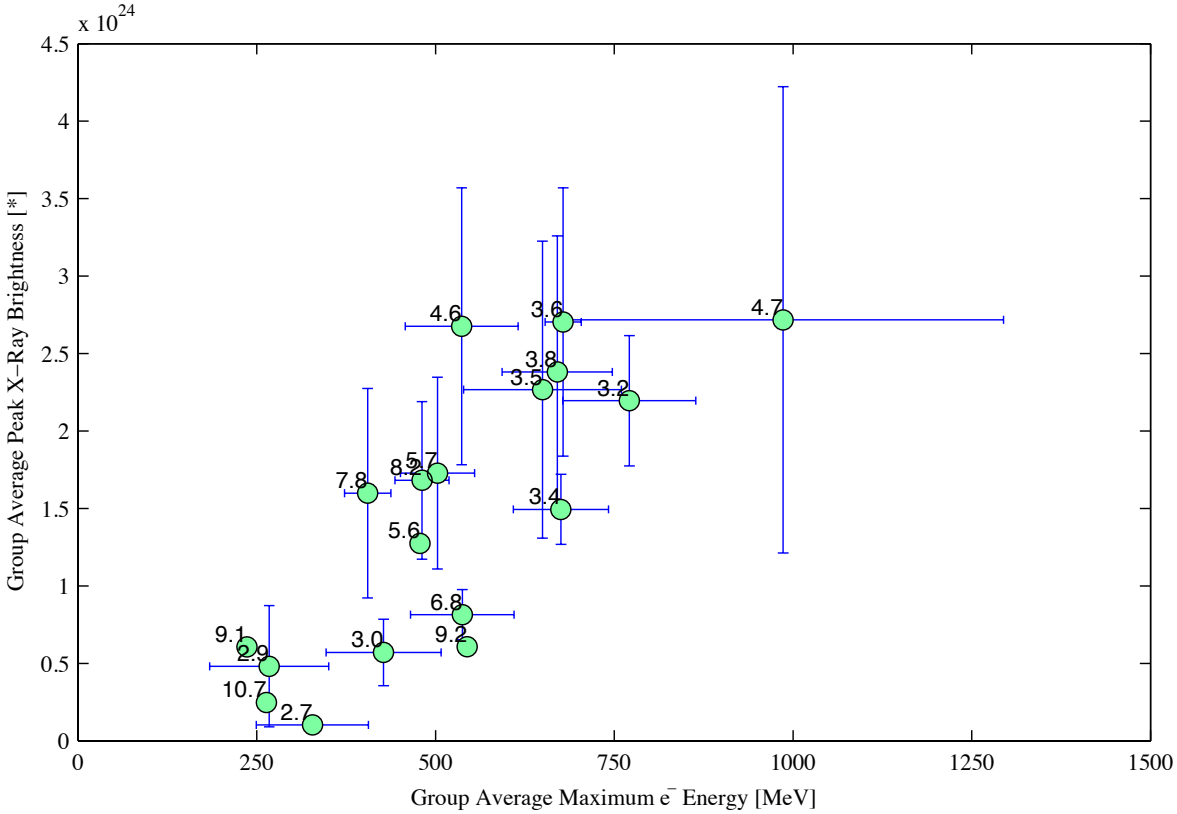

Figure 5.11: The average peak x-ray brightness for groups of shots at different plasma densities is shown plotted against the maximum electron energy average for the groups of shots. The error bars show the standard error about the mean. To the top left of each point the plasma density is written in units of 10^{18} cm^{-3}. Those points without error bars represent single shots. *The units of brightness are photons per second per mrad^2 per mm^2 per 0.1% bandwidth. A source size and 1μm is assumed, and the x-ray pulse duration is assumed to be 55 fs.

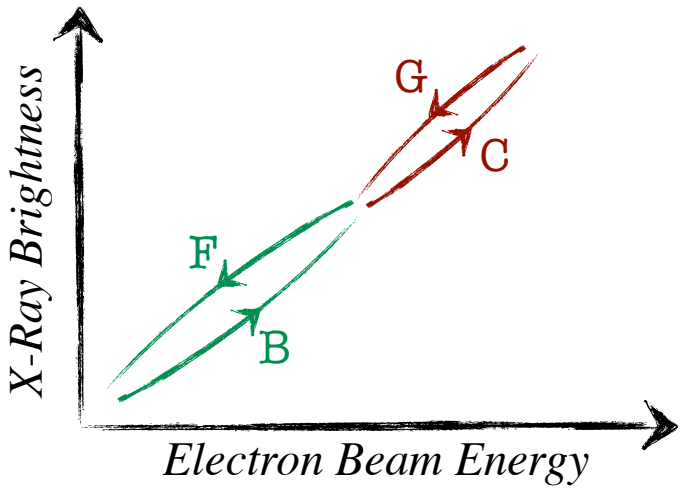

Figure 5.12: An illustration showing the various scenarios I hypothesise are responsible for the x-ray brightnesses observed. The scenarios are detailed in figure 5.6. In red are those responsible for the outlying very bright shots. In green are those responsible for the majority of the shots observed. The arrows on the lines indicate increasing plasma density.

Chapter 6

Discussion, Conclusions and Outlook

6.1 Threshold For Self-Injection In A Self-Guided LWFA

In this thesis, it has been shown in section 4.2 that the threshold for self injection in a self-guided laser wakefield accelerator is dependent on both the energy contained in the FWHM of the laser focal spot and the background electron plasma density. The dependence on power, as affected by laser pulse duration, is less important than the quality of the laser focal spot.

A model of the self-injection threshold based on combining simple theoretical models of electron motion, laser pulse compression, and wakefield bubble size has been discussed (4.2.1) and shown to have good agreement with experiment (4.2.2).

Figure 6.1 shows a comparison of reported LWFA experiments' self-injection thresholds, and the calculated prediction of the model (equation 4.6). In blue are shown the results from the Lund Experiment changing the laser energy. In red the threshold from the Gemini experiment. These experiments have peak laser powers of 18 TW and 180 TW respectively. One can see that the model shows good predictive power between these two lasers with an order of magnitude difference in power. In addition I have shown the reported threshold densities from other published experiments in green. I conclude that the model is an effective predictor as it is in good agreement to the observations made in experiment.

It can be useful in planning future experiments using both higher energy lasers

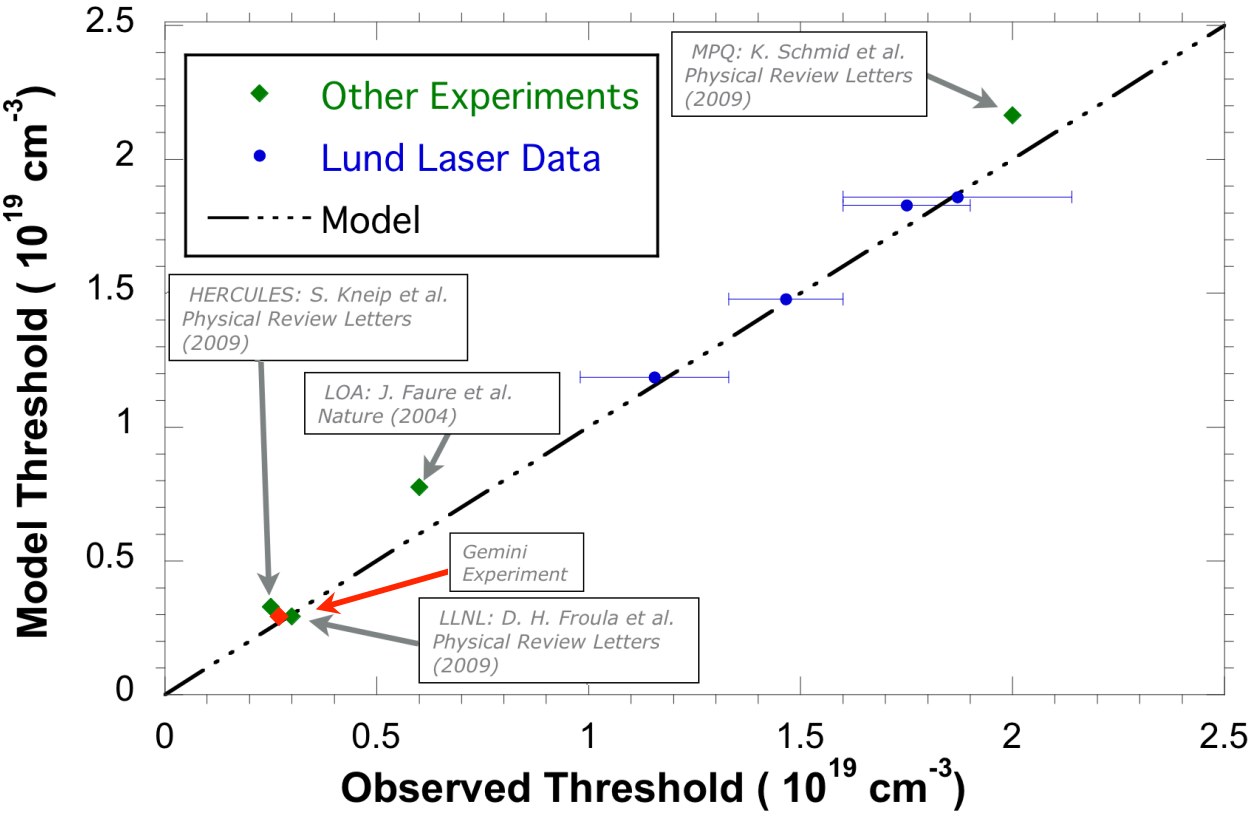

Figure 6.1: Plot of reported density threshold, verses predicted density threshold for the experiments presented herein and other published experiments. The circles show the predictions of the model given by equation 4.6 and the diamonds show the threshold based on 4.8

with lower density plasmas to produce higher energy electron and x-ray beams, and for lower energy laser systems where high repletion rate maybe required and precise design of gas delivery and removal for multiple shots is important, in bringing laser Wakefield technology to other applications.

6.2 Two-Screen Spectrometer Method for Measuring the 3D Momentum Distributions of GeV Electron Beams

In section 5.2 I showed a methodology which allows the full three dimensional momentum distribution of a LWFAs electron beam to be examined which provides insight

into the dynamics of electron injection and acceleration, vital for understanding the processes responsible for x-ray generation. The electron motion inside the laser wakefield is responsible for the generation of x-rays and through observing it directly gives a powerful tool in improving x-ray generation. In the future the technique could be used to understand how changes to the laser power, laser focus and adding aberrations to the laser wavefront, effect the electron motion via direct measurement rather than computer simulation. (It has been shown that x-ray critical energy can be increased through tailoring the laser wavefront [112].)

6.3 The Pre-Injection Pulse-Evolution Length of a LWFA

I have shown in section 5.3 that the laser pulse evolution (both self focusing and pulse compression) and the propagation of the laser through the length of plasma in the LWFA before self-injection of electrons has a effect on the electron energies produced. By defining a Pre-Injection Pulse-Evolution (PIPE) Length I have created a simple model to predict the maximum achievable electron energy in a self guided LWFA as a function of plasma density. I have shown this works for different accelerator lengths.

6.4 betatron X-Rays from LWFAs

Care must be taken in separating betatron X-rays from bremsstrahlung gamma-rays produced by LWFAs electron beams. This is important from an experimental and application point of view and prevented me from effectively measuring the x-rays from the 18TW Lund experiment. However in another experiment Genoud et al. 2011 [113] using the same laser saw x-rays with a critical energy of 1.7 keV and brightness of 3×10^{17} photons per second per mrad^2 per mm^2 per 0.1% bandwidth.

I was also involved in an experiment producing betatron x-rays using the 25 TW laser in LOA France, published in Thaury et al. 2013 [114], x-rays of 3 keV were seen Corde 2011 [115]. In Michigan using the Hercules laser (69 TW), the experiment I was also a part of, generated x-rays with a critical energy of 5 keV [69] (and 15 keV [116]) and brightness of 10^{22} photons per second per mrad^2 per mm^2 per 0.1% bandwidth.[1]

[1]Footnote: There is a disparity with the definition of critical energy used in these sources. I have

So the results of the experiment using the Gemini laser (180 TW) reported in section 5.4 of this thesis, with x-rays of 15-30 keV critical energy and brightness of 10^{24}-10^{25} photons per second per mrad^2 per mm^2 per 0.1% bandwidth, show a significant improvement in both energy and brightness over these previous experiments (see figure 6.2).

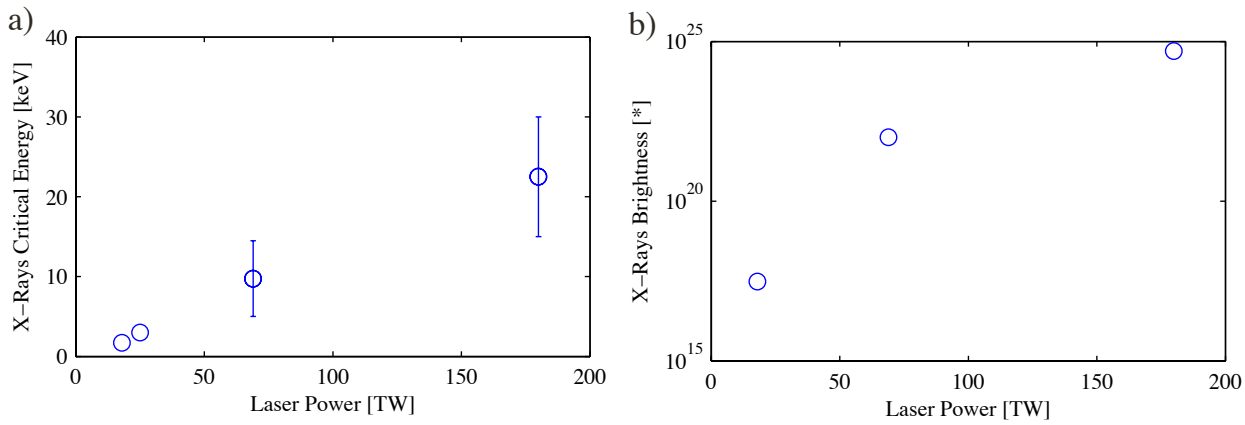

Figure 6.2: a) Reported betatron x-ray critical energies generated by LWFAs shown by laser peak power. From Genoud et al. 2011 [113], Thaury et al. 2013 [114] , Kneip et al. 2010 [116] and section 5.4 of this thesis. The bars show the range of critical energies seen under differing conditions. b) Reported betatron x-ray brightness generated by LWFAs shown by laser peak power. From Genoud et al. 2011 [113], Kneip et al. 2010 [116], and 5.4 of this thesis. *The units of brightness are photons per second per mrad^2 per mm^2 per 0.1% bandwidth.

This increase in critical energy and brightness of x-rays is due to the increase in the energy of the accelerated electrons. The Lund Laser (18 TW) produced electrons of up to 120 MeV [112] and in the Gemini Experiment (180 TW) electrons up to 1.3 GeV were seen (see figure 5.2). So an order of magnitude increase in laser energy has had an order of magnitude increase in accelerated electrons. A clear correlation between the x-ray brightness and electron beam energy was seen in figure 5.11 using a single laser.

I have discussed in Chapter 5 the effect the laser pulse evolution (both self focusing and pulse compression) and the propagation of the laser through the length of plasma

used and will continue to use throughout this work the definition from the 3rd Edition of Jackson [117]. Some sources such as Kneip 2010 [116] use the definition from the 2nd Edition of Jackson [118] which results in exactly double the value of critical energy I use.

in the LWFA before self-injection of electrons occurs on both the electron beam energies and x-rays generated. The PIPE length model and scenarios I described in Figure 5.6 explained the changes in electron energy due to changing the electron plasma density. They also help explain the variation in x-ray brightness and critical energy. I postulated that the very bright shots as shown in figure 5.10 pipe length is unusually short, potentially due to unmeasured changes in the laser wavefront, which caused the acceleration length to be unusually long and enter a scenario where a larger proportion of the electrons, which make up the electron beam ensemble, get closer to or pass and decelerate from, the dephasing energy.

Another possible explanation for the brightest shots is the effect of bubble injection expansion. As the wakefield bubble expands electrons are gradually injected. Depending on how this expansion occurs electrons may find themselves inside the bubble's electromagnetic fields at varying degrees from the laser axis. My instinct from PIC simulations is that if the bubble expands very quickly by a large amount, there will be a greater number of electrons inside the bubble off axis from this effect. Because the bubble fields increase linearly transversely from the laser axis, any displacement from the axis results in an increase in transverse momentum in the electron. One would then expect such an electron to produce a greater amount betatron radiation.

This can be contrasted with the situation of a bubble of fixed size traveling through a plasma, which is used in deriving the fields in Kostyukov et al. 2004 [101] and assumed in the threshold for injection in Thomas 2010 [102], which I have discussed and matched to experiments in section 4.2. In this situation electrons are injected by following elliptical trajectories in an unchanging bubble, and the transverse momentum of the election is from following these trajectories.

I have demonstrated the Two-Screen Spectrometer Method for Measuring the 3D Momentum Distributions of GeV Electron Beams in section 5.3 which may be used to examine the transverse momentum of the electrons directly after exiting the plasma. Perhaps in the future this can be used to confirm if bubble expansion is responsible for the brightest x-ray shots. However exact variation of the accelerator length would be necessary to avoid the electron beam interacting with the background plasma after the laser pulse has depleted as seen in section 5.3.

6.5 Phase Contrast Imaging

The betatron x-rays from laser wakefield accelerators can be easily used to conduct phase contrast imaging. This is especially true if an in-line geometry with no x-ray optics is used keeping the experimental set up simple. All that is required is a sufficiently small x-ray source to provide a sufficiently high-spatial coherence and that the object is in the near-field Fresnel diffraction regime close to light source. Then all that is required is that the observer is at a sufficient distance from the object. In the experiment described in Chapter 5, I placed phase contrast targets immediately after the deflecting magnet, as shown in figure 5.1.

Figures 6.3 and 6.4 show images from the x-ray camera. In these cases the Phase Contrast Target was a dead Acheta domesticus, (commonly called the house cricket and commonly farmed for food and sold as pet feed in the United Kingdom.) One can note that the exoskeleton of the creature is completely transparent to the x-rays, however the edges of the skeleton and structures inside the animal are visible. This is due to phase contrast taking place, proving the utility of the LWFA of this specific experiment, as an x-ray source for phase contrast imaging. X-ray phase contrast imaging is currently under investigation as an advanced medical imaging technique suitable for imaging soft tissue [119] and LWFA may be a useful alternative to micro-focus x-ray tubes as the x-ray critical energy can be produced in the 1-100 keV range and the radiation is delivered in tens of femto-seconds. This could remove the need for minutes or hours of exposure which can be a problem with x-ray tube based sources. Phase contrast imaging with LWFA betatron x-rays may be a solution waiting for a problem due to the novel nature of the source.

6.6 Future Directions

My thesis has shown that Laser Wakefield Accelerators have significant potential as x-ray sources for imaging. I have shown that achieving optimal x-ray and electron beam conditions with a given laser system will require the simultaneous control of both the plasma density and the plasma length – this conclusion suggests that future experiments will need to be performed with variable length gas cells rather than the fixed length gas jets used to date.

Future directions for the continuation of this work include investigating the use of betatron radiation sources for imaging of bio-medically interesting soft tissue such as

breast and prostate, both of which are major areas of interest in the field of cancer diagnosis and treatment. The ultra-short nature of the betatron x-rays also makes them ideal for imaging rapidly moving systems such as laser driven shocks.

The rapid increase with laser power of both the energy and brightness of the betatron radiation reported in this thesis indicates that the next generation of multi-PW laser systems will be able to produce ultra-bright sources of gamma rays that could perhaps be used in QED and nuclear physics experiments.

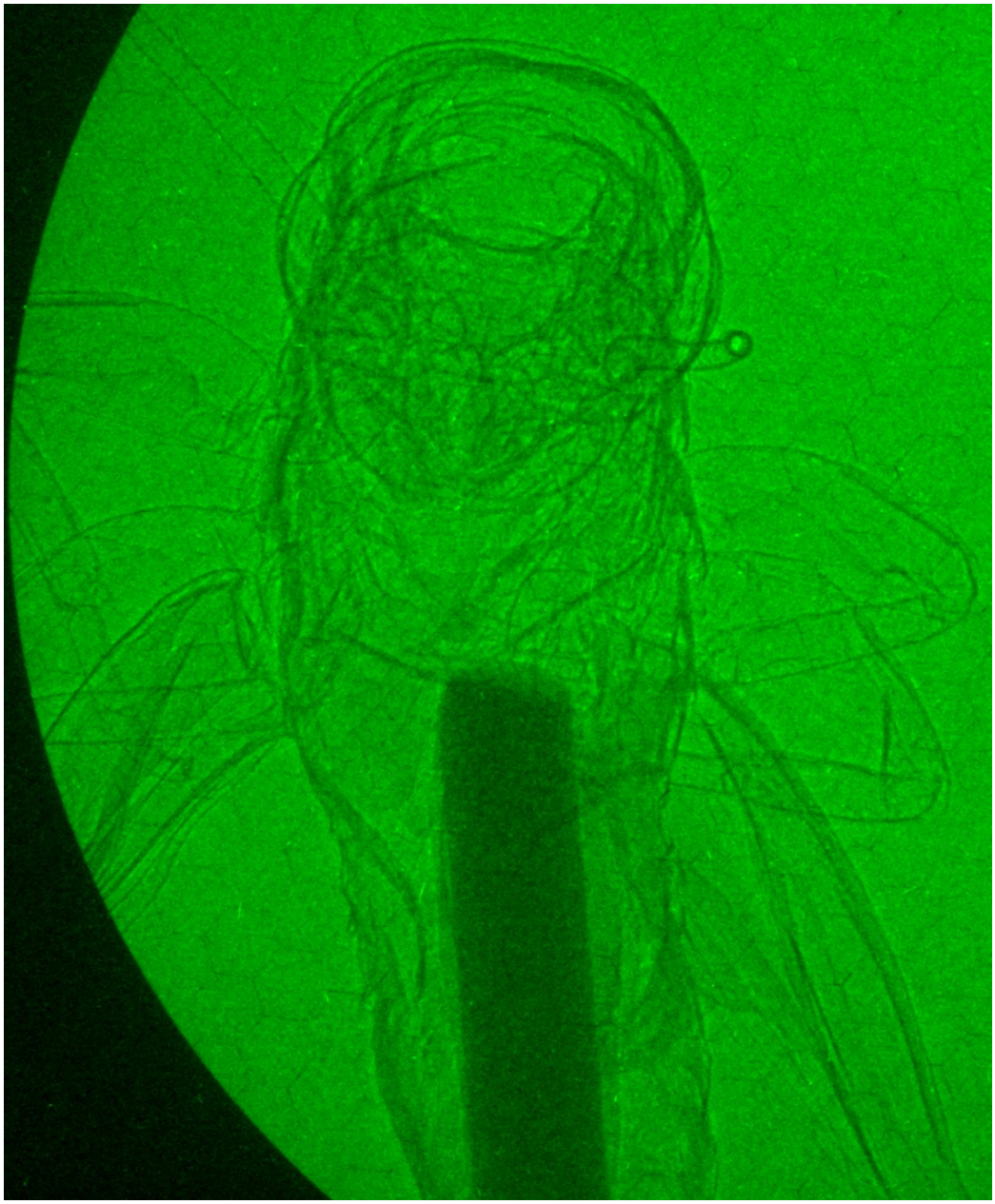

Figure 6.3: This image shows a high resolution x-ray image taken with the x-rays produced by a laser wakefield accelerator. The very small (micrometer sized) x-ray source allows a technique called phase contrast imaging to be used. This allows high definition imaging of objects even when they are transparent to the x-rays and is particularly good at showing up edges and boundaries. The image was taken on the experiment detailed in chapter 5.

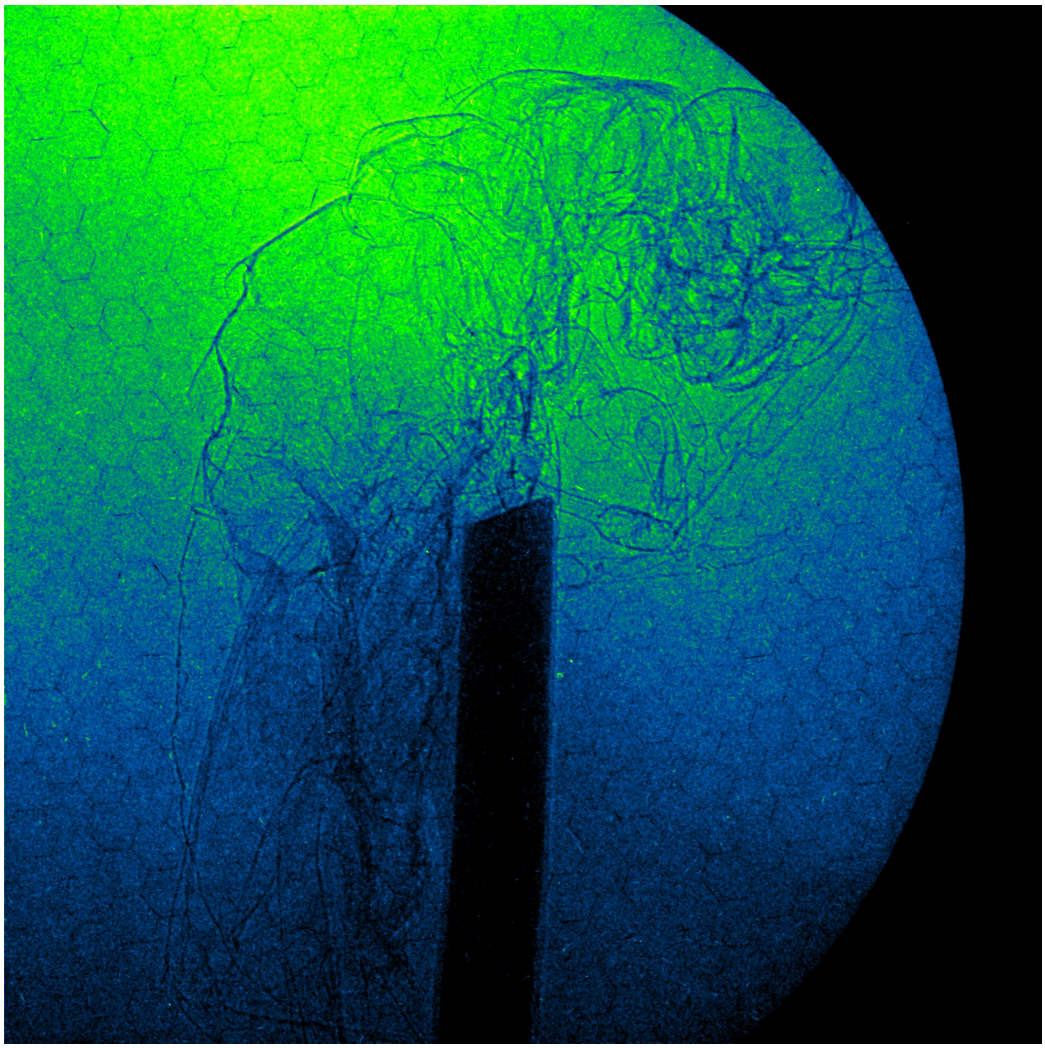

Figure 6.4: This image shows a high resolution x-ray image taken with the x-rays produced by a laser wakefield accelerator. The very small (micrometer sized) x-ray source allows a technique called phase contrast imaging to be used. This allows high definition imaging of objects even when they are transparent to the x-rays and is particularly good at showing up edges and boundaries. The image was taken on the experiment detailed in chapter 5.

Appendix A

Formula

This appendix represents a collection of formula and definitions which are used throughout without justification. It is provided for the convenience of the reader[1].

A.1 Maxwell's Equations

Gauss's Law

$$\nabla \cdot \overrightarrow{\mathbf{E}} = \frac{\rho}{\epsilon_0} \tag{A.1}$$

Gauss's Law of Magnetism

$$\nabla \cdot \overrightarrow{\mathbf{B}} = 0 \tag{A.2}$$

Faraday's Law

$$\nabla \times \overrightarrow{\mathbf{E}} = -\frac{\partial \overrightarrow{\mathbf{B}}}{\partial t} \tag{A.3}$$

Ampére's Law

$$\nabla \times \overrightarrow{\mathbf{B}} = \mu_0 \overrightarrow{\mathbf{J}} + \mu_0 \epsilon_0 \frac{\partial \overrightarrow{\mathbf{E}}}{\partial t} \tag{A.4}$$

A.2 Taylor's Series

The Taylor series of a real or complex function $f(x)$ which is infinitely differentiable in a neighbourhood of a real or complex number a is given by:

$$f(x) \approx \sum_{n=0}^{\infty} \frac{f^n(a)}{n!}(x-a)^n \tag{A.5}$$

[1]It is also indeed provided as a convenient reference to the writer.

where $f^n(a)$ denotes the nth derivative of f evaluated at the point a. For a function of more than on variable this becomes:

$$f(x_1, ..., x_d) = \sum_{n_1=0}^{\infty} ... \sum_{n_d=0}^{\infty} \frac{(x_1 - a_1)^{n_1} ... (x_d - a_d)^{n_d}}{n_1! ... n_d!} \left(\frac{\partial^{n_1+...+n_d} f}{\partial x_1^{n_1} ... \partial x_d^{n_d}} \right) (a_1, ..., a_d) \quad \text{(A.6)}$$

So for a function of two variables x and y around the point (a, b) the Taylor series to second order is:

$$\begin{aligned} f(x,y) \approx\ & f(a,b) + (x-a)\, f_x(a,b) + (y-b)\, f_y(a,b) \\ & + \frac{1}{2!} \left[(x-a)^2 f_{xx}(a,b) + 2(x-a)(y-b) f_{xy}(a,b) + (y-b)^2 f_{yy}(a,b) \right], \end{aligned}$$

where f_x and so on is the partial derviative $\partial f / \partial x$.

A.3 Miscellaneous

The Lorentz force (The force on a charge)

$$\overrightarrow{\mathbf{F}} = q(\overrightarrow{\mathbf{E}} + \overrightarrow{\mathbf{v}} \times \overrightarrow{\mathbf{B}}) \quad \text{(A.7)}$$

The Continuity Equation

$$\nabla \cdot \overrightarrow{\mathbf{J}} + \frac{\partial \rho}{\partial t} = 0 \quad \text{(A.8)}$$

The Convective Derivative

$$\frac{d\overrightarrow{\mathbf{G}}}{dt} = \frac{\partial \overrightarrow{\mathbf{G}}}{\partial t} + (\overrightarrow{\mathbf{v}} \cdot \nabla)\overrightarrow{\mathbf{G}} \quad \text{(A.9)}$$

Equation of Motion in a Plasma

$$m \left(\frac{\partial \overrightarrow{\mathbf{v}}}{\partial t} + (\overrightarrow{\mathbf{v}} \cdot \nabla)\overrightarrow{\mathbf{v}} \right) = q(\overrightarrow{\mathbf{E}} + \overrightarrow{\mathbf{v}} \times \overrightarrow{\mathbf{B}}) \quad \text{(A.10)}$$

Phase Velocity [2]

$$v_\phi = \frac{\omega}{k} \quad \text{(A.11)}$$

Group Velocity

$$v_g = \frac{d\omega}{dk} \quad \text{(A.12)}$$

[2] See D. Angular frequency in radians ω ($= 2\pi\times$ frequency) and the wave number $k = 2\pi/\lambda$

A.4 Identities

Here are some mathematical identities for reference.

$$\nabla \times (\nabla \times \overrightarrow{\mathbf{A}}) = \nabla(\nabla \cdot \overrightarrow{\mathbf{A}}) - \nabla^2 \overrightarrow{\mathbf{A}} \tag{A.13}$$

$$\overrightarrow{\mathbf{A}} \times (\overrightarrow{\mathbf{B}} \times \overrightarrow{\mathbf{C}}) = (\overrightarrow{\mathbf{A}} \cdot \overrightarrow{\mathbf{C}})\overrightarrow{\mathbf{B}} - (\overrightarrow{\mathbf{A}} \cdot \overrightarrow{\mathbf{B}})\overrightarrow{\mathbf{C}}. \tag{A.14}$$

Appendix B

Derivation of the Debye length

First let us consisider a plasma with a Boltzman distrbution of particles,

$$n_s = n_0 e^{-\frac{q_s \phi}{k_B T_s}} \tag{B.1}$$

where s is the particle species (either electrons or ions), q_s is the charge of the species, ϕ its pontiential, and T_s its temperature. n_0 is the election and ion density very far away where charges are balanced and there is no ϕ.

Now if we assume that the ion and electron temperatures are the same ($T_e = T_i$), and we are dealing with a helium like plasma where $q_e = -q_i$. Using Poisson's equation ($\nabla^2 \phi = \rho_{free}/\epsilon_0$) we have:

$$\nabla^2 \phi(r) = -\frac{\rho}{\epsilon_0} = \frac{q(n_i - n_e)}{\epsilon_0} = \frac{e n_0 (e^{\frac{e\phi(r)}{k_B T_e}} - 1)}{\epsilon_0} \tag{B.2}$$

We can expand around the exponential in a Taylor series (see A.2):

$$\nabla^2 \phi(r) = \frac{e n_0}{\epsilon_0} \left[\frac{e\phi(r)}{k_B T_e} + \frac{1}{2} \left(\frac{e\phi(r)}{k_B T_e} \right)^2 + ... \right] \tag{B.3}$$

We may then just keep the linear term but only if $k_B T_e \gg e\phi(r)$ however as $\phi(r)$ tends to fall of exponentially this is only for a small region. Keeping only the linear terms we have:

$$\nabla^2 \phi(r) = \frac{e^2 n_0}{\epsilon_0} \frac{\phi(r)}{k_B T_e} \tag{B.4}$$

The solution to this is equation is of the form:

$$\phi = \phi_0 \, e^{-\frac{|r|}{\lambda_D}} \tag{B.5}$$

where λ_D is a constant with units of length which defines the fall off of potential. From B.4 it is identifiable as:

$$\lambda_D = \left(\frac{\epsilon_0 k_B T_e}{n_0 e^2} \right)^2 \tag{B.6}$$

This is generally known as the Debye length. Because electrons generally are more mobile than ions and are therefore responsible for shielding it is appropriate to use $n_0 = n_e$.

Appendix C

Derivation of the Plasma Frequency

When electrons are displaced from their uniform background distribution, electric fields will be built up in such directions as to restore them to their original positions and restore neutrality to the plasma. However due to inertia it is inevitable that they will overshoot those positions and oscillate around their equilibrium positions with a characteristic frequency known as the plasma frequency.

The oscillation is so fast that the massive ions may be considered as fixed. The following assumptions must also be made.

- There is no magnetic field
- It is a cold plasma. There are no thermal motions ($k_B T = 0$)
- The ions are uniformly distributed and fixed.
- The extent of the plasma is infinite.
- The electrons only move in the x direction.

$$\nabla = \hat{\mathbf{i}}\,\partial/\partial x \qquad \vec{\mathbf{E}} = \hat{\mathbf{i}}\,E \qquad \nabla \times \vec{\mathbf{E}} = 0 \qquad \vec{\mathbf{E}} = -\nabla\phi \tag{C.1}$$

As we are assuming their is no fluctuating magnetic field this can be considered an electrostatic oscillation. The equation of motion A.10 is then,

$$m_e n_e \left(\frac{\partial \vec{\mathbf{v}}_e}{\partial t} + (\vec{\mathbf{v}}_e \cdot \nabla)\vec{\mathbf{v}}_e \right) = -e n_e (\vec{\mathbf{E}} + \vec{\mathbf{v}}_e \times \vec{\mathbf{B}}) \tag{C.2}$$

and the equation of continutity A.8 is then

$$\nabla \cdot n_e \overrightarrow{\mathbf{v}}_e + \frac{\partial n_e}{\partial t} = 0 \tag{C.3}$$

from the first Maxwell equation (Gauss's Law) A.1 we have

$$\epsilon_0 \frac{\partial \overrightarrow{\mathbf{E}}}{\partial \overrightarrow{\mathbf{x}}} = e(n_i - n_e) \tag{C.4}$$

We can split the dependent variables into two parts and equalibrum part and a perturbation part:

$$n_e = n_E + n_P \qquad \overrightarrow{\mathbf{v}}_e = \overrightarrow{\mathbf{v}}_E + \overrightarrow{\mathbf{v}}_P \qquad \overrightarrow{\mathbf{E}} = \overrightarrow{\mathbf{E}}_E + \overrightarrow{\mathbf{E}}_P \tag{C.5}$$

As the equlibrum quantites express the state of the plasma in the absence of oscillation.

$$\nabla n_E = \overrightarrow{\mathbf{v}}_E = \overrightarrow{\mathbf{E}}_E = \frac{\partial n_E}{\partial t} = \frac{\partial \overrightarrow{\mathbf{v}}_E}{\partial t} = \frac{\partial \overrightarrow{\mathbf{E}}_E}{\partial t} = 0 \tag{C.6}$$

$$n_{iP} = 0 \qquad n_{iE} = n_{eE} \tag{C.7}$$

Applying these condtions and linearising (removing all terms with an ampliture quantity n_P, $\overrightarrow{\mathbf{v}}_P$, $\overrightarrow{\mathbf{E}}_P$ appearing as a more than a 1st power) equations C.2, C.3, and C.4 become:

$$m_e \frac{\partial \overrightarrow{\mathbf{v}}_P}{\partial t} = -e \overrightarrow{\mathbf{E}}_P \tag{C.8}$$

$$\frac{\partial n_P}{\partial t} + n_E \nabla \cdot \overrightarrow{\mathbf{v}}_P = 0 \tag{C.9}$$

$$\epsilon_0 \nabla \cdot \overrightarrow{\mathbf{E}} = -e n_P \tag{C.10}$$

Those oscillating are assumed to be oscillating sinusoidally:

$$\overrightarrow{\mathbf{v}}_P = v_{max}\, e^{i(kx-\omega t)} \widehat{\mathbf{x}} \tag{C.11}$$

$$n_P = n_{max}\, e^{i(kx-\omega t)} \tag{C.12}$$

$$\overrightarrow{\mathbf{E}}_P = E_{max}\, e^{i(kx-\omega t)} \widehat{\mathbf{x}} \tag{C.13}$$

So the equations then become:

$$-i m_e \omega v_{max} e^{i(kx-\omega t)} \widehat{\mathbf{x}} = -e E_{max} e^{i(kx-\omega t)} \widehat{\mathbf{x}} \tag{C.14}$$

$$-i\omega n_{max}\, e^{i(kx-\omega t)} + n_E i k v_{max}\, e^{i(kx-\omega t)} = 0 \tag{C.15}$$

$$\epsilon_0 i k E_{max}\, e^{i(kx-\omega t)} = -e n_{max}\, e^{i(kx-\omega t)} \tag{C.16}$$

Solving for ω, noting that n_E is n_e of our initial plasma, and eliminating E_{max} and n_{max} we finally get:

$$\omega_p = \left(\frac{e^2 n_e}{\epsilon_0 m_e} \right)^{1/2} \tag{C.17}$$

Appendix D

Phase Velocity, Group Velocity, and Dispersion Relation

Phase Velocity

A sinusoidally oscillating quantity can be, and often is, represented by

$$n = n_{max} e^{i(\vec{\mathbf{k}} \cdot \vec{\mathbf{r}} - \omega t)}$$

which becomes $n = n_{max} e^{i(kx - \omega t)}$ if propagation is in the x direction. The real component of this is

$$\Re(n) = n_{max} \cos(kx - \omega t)$$

A point of constant phase[1] on the wave will move so that:

$$\frac{d}{dt}(kx - \omega t) = 0$$

So the velocity of this point is:

$$\frac{dx}{dt} = \frac{\omega}{k} \equiv v_\phi \tag{D.1}$$

where v_ϕ is know as the PHASE VELOCITY. It should be the same for all waves in a given medium.

Group Velocity

Consider two waves:

$$E_1 = E_0 cos\,[(k + \Delta k)x - (\omega + \Delta\omega)t], \qquad E_2 = E_0 cos\,[(k - \Delta k)x - (\omega - \Delta\omega)t]$$

[1] A point where the magnitude of the quantity n is unchanging but moves in space.

Their frequency therefore differs by $2\Delta\omega$. The phase velocity v_ϕ should be the same for both, this necessitates that the difference in their wave number being $2\Delta k$. Letting:

$$a = kx - \omega t \qquad\qquad b = (\Delta k)x - (\Delta\omega)t$$

Then the effect of the two waves interfering is

$$\begin{aligned} E_1 + E_2 &= E_0 \cos(a+b) + E_0 \cos(a-b) \\ &= 2E_0 \cos a \; cosb \\ &= 2\cos[kx - \omega t]\cos[(\Delta k)x - (\Delta\omega)t] \end{aligned}$$

where $E_0 \cos b$ represents an envelope wave which carries information its velocity is $\Delta\omega/\Delta k$. This represents a carrier wave modulated by an envelope wave $\cos[(\Delta k)x - (\Delta\omega)t]$. The carrier wave carries information and it can be seen in the same way as above its velocity is given by $\Delta\omega/\Delta k$. As $\Delta\omega \to 0$ then it becomes:

$$v_g \equiv \frac{d\omega}{dk} \tag{D.2}$$

Which is known as the GROUP VELOCITY.

Dispersion Relation

For a given wave form in a given medium the relation between the angular frequency in radians ω ($= 2\pi\times$ frequency) and the wave number $k = 2\pi/\lambda$ is known as the dispersion relation.

List of Figures

2.1 Relevant lengths in the definition of the Rayleigh length. 20

3.1 A two screen electron spectrometer. Electrons of differing energies are shown passing through scintillating screens as calculated by tracking algorithm. The setup shown is for the Gemini 2011 experiment, and the magnet field map is shown in figure 3.4. 40

3.2 The geometry of an electron passing through an ideal rectangular magnetic field. 41

3.3 The mapped field of the magnet used in the Lund Experiment. The units of the labelled contours are mT 43

3.4 The mapped field of the magnet used in the Gemini Experiment. The units of the labelled contours are mT. The magnet consists of rectangular pole pieces constructed from sintered neodymium blocks, mounted in a c-shaped yoke. This c-shape allows low energy electrons to leave the spectrometer without striking the yoke, further reducing the bremsstrahlung radiation produced. The pole piece separation is 25 mm. We find that the field maximum is 1.02 T in the mid-plane of the magnet with a field uniformity of 0.01 T r.m.s. over the central 200 mm of the magnet. The yoke design ensures that there is no field reversal along the electron propagation direction. The magnet is constructed in two sections, each 150 mm long. In this experiment these were fixed together providing a single magnet 300 mm long. 44

3.5 Three electron paths are shown which all impact screen 1 at the same position. b) Shows the path of an electron exiting the LWFA along the laser axis. a) Shows a higher energy electron exiting at a positive angle. c) Shows a lower energy electron exiting at a negative angle. . 46

3.6 Diagram of the iterative algorithm for finding the energy and exit angle of electrons exiting a LWFA incident on a two screen spectrometer. . 48
3.7 Initial filter pack design. Designed for categorising the critical energy of a betatron-like x-ray spectrum between 1 and 10 keV. The backing material 6 μm of mylar (Biaxially-oriented polyethylene terephthalate) with 90 nm of aluminium. 51
3.8 Table of filters used in initial filter pack design. Designed for categorising the critical energy of a betatron like x-ray spectrum between 1 and 10 keV. 51
3.9 Table of elements used in filter pack designed for betatron like spectra with critical energies between 1 and 100 keV. 52
3.10 This a typical (if bright) image captured by the x-ray camera on the Lund experiment. The different filters are clearly visible. For analysis purposes the image is broken into the sections shown. 1) and 8) act as a background calibration and are covered with 2mm Copper. 2) 3μm V, 3) 3μm Fe, 4) 5μm Ni, 5) 5μm Zn, 6) 3μm Zr, 7) The backing material 6 μm of mylar (Biaxially-oriented polyethylene terephthalate) with 90 nm of aluminium. The camera was a front illuminated Andor CCD mounted in vacuum. The axis show pixel number. 53
3.11 Grid filter pack design 4x4. Designed for categorising the critical energy of a betatron like x-ray spectrum between 1 and 100 keV. The backing material 6 μm of mylar (Biaxially-oriented polyethylene terephthalate) with 90 nm of aluminium. Used in the Gemini Experiment chapter. 54
3.12 Grid filter pack design 8x8. Designed for categorising the critical energy of a betatron like x-ray spectrum between 1 and 100 keV. The backing material 6 μm of mylar (Biaxially-oriented polyethylene terephthalate) with 90 nm of aluminium. Used in the Gemini Experiment. 55
3.13 An image from the Princeton PIXIS camera system used on the Gemini experiment. The colour table is arbitrary but linear. One can see the x-ray beam varies in intensity. 56

3.14 An image from the Princeton PIXIS camera system used on the Gemini experiment. The colour table is arbitrary but linear and saturated in places. The extent of each filter region is shown in blue. The regions around each filter(to normalise for inhomogeneities in the beam) are shown in green. 56
3.15 Photograph of a filter pack in place on the Gemini experiment. A beryllium window is used to pass the x-rays into air. The length of vacuum tube is used to provide information on the level of bremsstrahlung radiation. 57
3.16 An illustration of the stages involved in an x-ray causing an ADC count in the Princeton PIXIS camera system. 58
3.17 The Princeton PIXIS system's CCD array quantum efficiency is shown in red. The Princeton PIXIS camera system's Csl:TI scintillator's x-rays absorption efficiency is shown in blue. This includes the transmission through the 10 mm Be window. Data reproduced from Princeton Instruments documentation [92]. 59
3.18 The ADC settings for the Princeton PIXIS system. Reproduced from Princeton Instrument's unique calibration. 61
3.19 Photo of calibration setup with approximate scale. 61
3.20 Exposure to Fe-55 for 1800 s. b) Exposure with no source present. c) A pixel by pixel subtraction of a) from b). The images above show the camera counts. The histograms below show the exact colour tables used for the images above. 62
3.21 The geometry used for the off axis distribution of a disk radiation source. 63
3.22 The on axis distribution due to a point like source (green line) and the on axis distribution for a disk source (red dotted line). 64
3.23 Calculation of the off axis distribution of radiation for a uniform disk source of 2.5926 MBq activity radius 5.5 mm, placed at distance z from a pixel detector with the same pixel size and dimensions as the Princeton PIXIS system. The distribution was calculated numerically and in this case the constant M (defined above) has been set to one. a) z = 1 mm. b) z = 3 mm. c) z = 5 mm. 64

3.24 Blue Solid Line: A lineout through the centre of the signal due to exposure to the Fe-55 source for 1800 s after a pixel by pixel background subtraction. Red Dashed Line: The off axis distribution calculated with fitted values of z=3.11 mm and M = 0.942 for a uniform 2.5926 MBq activity disk source of radius 5.5 mm, 1800 s exposure. 65

4.1 The experimental set up for the Lund Laser Lab experiment. 68
4.2 Focal spot images recorded with increasing amounts of spherical aberration. From left to right the intensity contained in the FWHM is (a) 47%, (b) 40%, (c) 31%, (d) 20%. 70
4.3 Measurements of the electron beam profile for different plasma densities for $\alpha = 0.40$. The colour table is linear and in arbitrary units. A threshold for injection is clearly visible between densities of 1.3 and 1.6 x 10^{19} cm^3. 71
4.4 The recorded charge for the different focal spot qualities (α) for different plasma densities (n_e). 72
4.5 The recorded charge for the different focal spot qualities (α) plotted against the power in the FWHM of the pulse as a ratio of power for self focusing ($\alpha P/P_p$). 73
4.6 The recorded charge for the different laser energies against different plasma densities (n_e). $\alpha = 0.47$. 74
4.7 Electron beam profiles for various plasma densities for different values of the amount of laser energy within the FWHM of the focal spot α. Each panel is an average of five shots and is displayed on a logarithmic color scale. (a), (b), and (d) kept the total laser energy E constant but varied α whereas (c) reduced the laser energy E. (I made this figure, which was first published in Mangles, Bloom, et al. 2012 [99]. Reproduced under creative commons licence.) 75
4.8 (Left) This is the recorded charge on the electron profile monitor for when the position of the compressor gratings is varied. (Right) The pulse duration measured using a "GRENOUILLE" against grating position. 76

4.9 (a) Electron charge (>4 MeV) versus $\alpha P/P_c$ keeping the pulse duration constant but varying the focal spot quality α and the plasma density n_e (closed circles) or total pulse energy E, and plasma density (open squares) but keeping the pulse duration constant τ_0. (b) Electron charge versus $\alpha P/P_c$ varying pulse duration τ_0 while keeping plasma density n_e and energy in focal spot αE constant. (c) Data from (a) and (b) plotted versus $\alpha E n_e/n_c$. Each data point is an average of five shots and the error bars represent 1 standard deviation. (I made this figure, which was first published in Mangles, Bloom, et al. 2012 [99]. Reproduced under creative commons licence.) 77

4.10 Observed electron density threshold for self injection as a function of laser energy (αE). The solid curve represents the model discussed in section 4.2.1 given by equation 4.6. The dashed curve represents the alternate threshold model given by 4.8. 81

5.1 Experimental layout showing the laser beam path and the separation of the electron beam from the x-ray beam. 84

5.2 Raw images of electron spectrometer scintillator screens. Images from a) screen 1 and b) screen 2 for a shot at $n_e = 5 \times 10^{19}$ cm^{-3} and a 10 mm gas jet nozzle, c) and d) show a smaller region. The marked point on the right corresponds to 1.34 $\pm$ 0.07 GeV electrons at an angle of 3 mrad. The marked point on the left corresponds to 1.09 $\pm$ 0.04 GeV at an angle of -1 mrad. 86

5.3 Raw images of electron spectrometer scintillator screens. Images from a) screen 1 and b) screen 2 for a shot at $n_e = 2\times10^{18}$ cm^{-3} and a 15 mm gas jet nozzle. The marked points have their momentum components p_x , p_y and p_z plotted in figure 5. 87

5.4 a) Three dimensional momentum distribution of one of the beamlets shown in figure 5.3. The blue points are 3D momentum coordinates of the identified features in the beam. The blue plane is the "plane of best-fit" to these points. The red plane corresponds to the laser electric field direction. Two additional views are shown (without axes) taken along the direction of the red and the blue arrows. b) shows the view along the red arrow (1), highlighting the head-to-tail tilt of the beam; c) shows the view along the blue arrow (2). This is a direction almost tangential to the red and blue planes, showing that the electrons are approximately distributed in a plane that is approximately at 90° to the laser electric field direction. 88

5.5 The data from 24 shots of the laser, using the 10 mm nozzle, is shown in order of increasing density (from left to right) a) Shows the images from one of the electron spectrometer screens. The electrons to the top of the images have been deflected less by the magnet and have a higher energy. b) Shows the plasma densities of each of these shots. c) The images from the Princeton PIXIS x-ray camera for each shot are shown. 90

5.6 The illustration shows the various scenarios which can occur in a LWFA due to differing ratios between the lengths L_{PLASMA} , L_{ETCH}, L_{ACC}, L_{ϕ} and L_{PIPE}, (not to scale). The blue line represents the energy of an electron self injected at the beginning of L_{ACC}, and demonstrates the effect of L_{ϕ} on such an electron. (However in D and H the energies shown are for a idealised simplified symmetric series of wakefield periods which doesn't take into account the presence of the laser pulse, the plasma between wakefield periods or that the LWFA my be in a bubble regime.) A, B, C and D are limited by the plasma length L_{PLASMA}, whereas E, F, G and H are the same but limited instead by the laser depletion length L_{ETCH}. 91

5.7 Variation of electron beam energy with density for the 10mm nozzle. In blue are shown the upper limit of the electron's energy spectra for a number of shots at each plasma density. The blue circles are the mean value of the upper energy limit of these shots. The bars shown are the standard error about the mean. In black are shown the mean electron energy in the spectra. The black crosses are the mean of multiple shots. The bars again show the standard error about the mean. In green is shown the prediction of equations 5.4, 5.5 and 5.6. The red line shows the prediction of the simple model taking into account the PIPE length. 94

5.8 Variation of electron beam energy with density for the 15 mm nozzle. In blue are shown the upper limit of the electron's energy spectra for a number of shots at each plasma density. The blue circles are the mean value of the upper energy limit of these shots. The bars shown are the standard error about the mean. In black are shown the mean electron energy in the spectra. The black crosses are the mean of multiple shots. The bars again show the standard error about the mean. In green is shown the prediction of equations 5.4, 5.5 and 5.6. The red line shows the prediction of the simple model taking into account the PIPE length. 96

5.9 The table shows which scenario shown in figure 5.6 the simple model predicts will occur for various plasma densities and plasma lengths, for S = 11.5 mm. The laser parameters used are those of the experiment. *Scenarios A and E are trivial because no electron acceleration occurs. So the dephasing length has no real meaning. 97

5.13 The average measured x-ray spectrum critical energy for multiple shots at different plasma densities. A synchrotron like spectrum is assumed (see section 3 for more details). The error bars show the standard error about the mean. 99

5.10 Blue: The average peak x-ray brightness of multiple shots at each density. *The units of brightness are photons per second per mrad^2 per mm^2 per 0.1% bandwidth. A source size and 1 μm is assumed, and the x-ray pulse duration is assumed to be 55 fs. The error bars show the standard error about the mean. Red: The peak x-ray brightness of the brightest shots at each density. The error in each individual measurement is smaller than the circle shown. Green: The average of multiple shots' electron beam mean energy. The error bars shown are the standard error about the mean. 101

5.11 The average peak x-ray brightness for groups of shots at different plasma densities is shown plotted against the maximum electron energy average for the groups of shots. The error bars show the standard error about the mean. To the top left of each point the plasma density is written in units of 10^{18} cm^{-3}. Those points without error bars represent single shots. *The units of brightness are photons per second per mrad^2 per mm^2 per 0.1% bandwidth. A source size and 1μm is assumed, and the x-ray pulse duration is assumed to be 55 fs. 102

5.12 An illustration showing the various scenarios I hypothesise are responsible for the x-ray brightnesses observed. The scenarios are detailed in figure 5.6. In red are those responsible for the outlying very bright shots. In green are those responsible for the majority of the shots observed. The arrows on the lines indicate increasing plasma density. 103

6.1 Plot of reported density threshold, verses predicted density threshold for the experiments presented herein and other published experiments. The circles show the predictions of the model given by equation 4.6 and the diamonds show the threshold based on 4.8 105

6.2 a) Reported betatron x-ray critical energies generated by LWFAs shown by laser peak power. From Genoud et al. 2011 [113], Thaury et al. 2013 [114] , Kneip et al. 2010 [116] and section 5.4 of this thesis. The bars show the range of critical energies seen under differing conditions. b) Reported betatron x-ray brightness generated by LWFAs shown by laser peak power. From Genoud et al. 2011 [113], Kneip et al. 2010 [116], and 5.4 of this thesis. *The units of brightness are photons per second per mrad^2 per mm^2 per 0.1% bandwidth. 107

6.3 This image shows a high resolution x-ray image taken with the x-rays produced by a laser wakefield accelerator. The very small (micrometer sized) x-ray source allows a technique called phase contrast imaging to be used. This allows high definition imaging of objects even when they are transparent to the x-rays and is particularly good at showing up edges and boundaries. The image was taken on the experiment detailed in chapter 5. 111

6.4 This image shows a high resolution x-ray image taken with the x-rays produced by a laser wakefield accelerator. The very small (micrometer sized) x-ray source allows a technique called phase contrast imaging to be used. This allows high definition imaging of objects even when they are transparent to the x-rays and is particularly good at showing up edges and boundaries. The image was taken on the experiment detailed in chapter 5. 112

Bibliography

[1] E. Esarey, C. B. Schroeder, and W. P. Leemans, *Physics of laser-driven plasma-based electron accelerators*, Reviews of Modern Physics **81**, 1229 (2009).

[2] V. Malka, S. Fritzler, E. Lefebvre, M. M. Aleonard, F. Burgy, J. P. Chambaret, J. F. Chemin, K. Krushelnick, G. Malka, S. P. D. Mangles, Z. Najmudin, M. Pittman, J. P. Rousseau, J. N. Scheurer, B. Walton, and A. E. Dangor, *Electron acceleration by a wake field forced by an intense ultrashort laser pulse*, Science **298**, 1596 (2002).

[3] T. Tajima and J. M. Dawson, *Laser Electron-Accelerator*, Physical Review Letters **43**, 267 (1979).

[4] H. Hamster, A. Sullivan, S. Gordon, W. White, and R. W. Falcone, *Subpicosecond, Electromagnetic Pulses from Intense Laser-Plasma Interaction*, Physical Review Letters **71**, 2725 (1993).

[5] K. Nakajima, D. Fisher, T. Kawakubo, H. Nakanishi, A. Ogata, Y. Kato, Y. Kitagawa, R. Kodama, K. Mima, H. Shiraga, K. Suzuki, K. Yamakawa, T. Zhang, Y. Sakawa, T. Shoji, Y. Nishida, N. Yugami, M. Downer, and T. Tajima, *Observation of Ultrahigh Gradient Electron Acceleration by a Self-Modulated Intense Short Laser-Pulse*, Physical Review Letters **74**, 4428 (1995).

[6] A. Modena, Z. Najmudin, A. E. Dangor, C. E. Clayton, K. A. Marsh, C. Joshi, V. Malka, C. B. Darrow, C. Danson, D. Neely, and F. N. Walsh, *Electron Acceleration from the Breaking of Relativistic Plasma-Waves*, Nature **377**, 606 (1995).

[7] F. Amiranoff, S. Baton, D. Bernard, B. Cros, D. Descamps, F. Dorchies, F. Jacquet, V. Malka, J. R. Marques, G. Matthieussent, P. Mine, A. Modena,

P. Mora, J. Morillo, and Z. Najmudin, *Observation of laser wakefield acceleration of electrons*, Physical Review Letters **81**, 995 (1998).

[8] M. N. Rosenbluth and C. S. Liu, *Excitation of Plasma Waves by Two Laser Beams*, Physical Review Letters **29**, 701 (1972).

[9] N. M. Kroll, A. Ron, and N. Rostoker, *Optical Mixing as a Plasma Density Probe*, Physical Review Letters **13**, 83 (1964).

[10] C. E. Clayton, C. Joshi, C. Darrow, and D. Umstadter, *Relativistic Plasma-Wave Excitation by Collinear Optical Mixing*, Physical Review Letters **54**, 2343 (1985).

[11] A. E. Dangor, A. K. L. Dymokebradshaw, and A. E. Dyson, *Observation of Relativistic Plasma-Waves Generated by the Beat-Wave with 1 Mu-M Lasers*, Physica Scripta **T30**, 107 (1990).

[12] Y. Kitagawa, T. Matsumoto, T. Minamihata, K. Sawai, K. Matsuo, K. Mima, K. Nishihara, H. Azechi, K. A. Tanaka, H. Takabe, and S. Nakai, *Beat-Wave Excitation of Plasma-Wave and Observation of Accelerated Electrons*, Physical Review Letters **68**, 48 (1992).

[13] M. Everett, A. Lal, D. Gordon, C. E. Clayton, K. A. Marsh, and C. Joshi, *Trapped Electron Acceleration by a Laser-Driven Relativistic Plasma-Wave*, Nature **368**, 527 (1994).

[14] C. E. Clayton, M. J. Everett, A. Lal, D. Gordon, K. A. Marsh, and C. Joshi, *Acceleration and Scattering of Injected Electrons in Plasma Beat-Wave Accelerator Experiments*, Physics of Plasmas **1**, 1753 (1994).

[15] F. Amiranoff, J. Ardonceau, M. Bercher, D. Bernard, B. Cros, A. Debraine, J. M. Dieulot, J. Fusellier, F. Jacquet, J. M. Joly, M. Juillard, G. Matthieussent, P. Matricon, P. Mine, B. Montes, P. Mora, R. Morano, J. Morillo, F. Moulin, P. Poilleux, A. E. Specka, and C. Stenz, *The Plasma Beat-Wave Acceleration Experiment at Ecole Polytechnique*, Nuclear Instruments & Methods in Physics Research Section A - Accelerators Spectrometers Detectors and Associated Equipment **363**, 497 (1995).

[16] B. Walton, Z. Najmudin, M. S. Wei, C. Marle, R. J. Kingham, K. Krushelnick, A. E. Dangor, R. J. Clarke, M. J. Poulter, C. Hernandez-Gomez, S. Hawkes, D. Neely, J. L. Collier, C. N. Danson, S. Fritzler, and V. Malka, *Large-amplitude plasma wave generation with a high-intensity short-pulse beat wave*, Optics Letters **27**, 2203 (2002).

[17] B. Walton, Z. Najmudin, M. S. Wei, C. Marle, R. J. Kingham, K. Krushelnick, A. E. Dangor, R. J. Clarke, M. J. Poulter, C. Hernandez-Gomez, S. Hawkes, D. Neely, J. L. Collier, C. N. Danson, S. Fritzler, and V. Malka, *Measurements of plasma-wave generation using a short-pulse high-intensity laser beat wave*, Physics of Plasmas **13**, 013103 (2006).

[18] D. Strickland and G. Mourou, *Compression of Amplified Chirped Optical Pulses*, Optics Communications **55**, 447 (1985).

[19] C. A. Coverdale, C. B. Darrow, C. D. Decker, W. B. Mori, K. C. Tzeng, K. A. Marsh, C. E. Clayton, and C. Joshi, *Propagation of Intense Subpicosecond Laser-Pulses through Underdense Plasmas*, Physical Review Letters **74**, 4659 (1995).

[20] A. Ting, C. I. Moore, K. Krushelnick, C. Manka, E. Esarey, P. Sprangle, R. Hubbard, H. R. Burris, R. Fischer, and M. Baine, *Plasma wakefield generation and electron acceleration in a self-modulated laser wakefield accelerator experiment*, Physics of Plasmas **4**, 1889 (1996).

[21] M. I. K. Santala, Z. Najmudin, E. L. Clark, M. Tatarakis, K. Krushelnick, A. E. Dangor, V. Malka, J. Faure, R. Allott, and R. J. Clarke, *Observation of a hot high-current electron beam from a self-modulated laser wakefield accelerator*, Physical Review Letters **86**, 1227 (2001).

[22] Z. Najmudin, K. Krushelnick, E. L. Clark, S. P. D. Mangles, B. Walton, A. E. Dangor, S. Fritzler, V. Malka, E. Lefebvre, D. Gordon, F. S. Tsung, and C. Joshi, *Self-modulated wakefield and forced laser wakefield acceleration of electrons*, Physics of Plasmas **10**, 2071 (2003).

[23] W. Lu, C. Huang, M. Zhou, W. B. Mori, and T. Katsouleas, *Nonlinear theory for relativistic plasma wakefields in the blowout regime*, Physical Review Letters **96**, 165002 (2006).

[24] A. Pukhov and J. Meyer-ter Vehn, *Laser wake field acceleration: the highly non-linear broken-wave regime*, Applied Physics B-Lasers and Optics **74**, 355 (2002).

[25] S. P. D. Mangles, C. D. Murphy, Z. Najmudin, A. G. R. Thomas, J. L. Collier, A. E. Dangor, E. J. Divall, P. S. Foster, J. G. Gallacher, C. J. Hooker, D. A. Jaroszynski, A. J. Langley, W. B. Mori, P. A. Norreys, F. S. Tsung, R. Viskup, B. R. Walton, and K. Krushelnick, *Monoenergetic beams of relativistic electrons from intense laser-plasma interactions*, Nature **431**, 535 (2004).

[26] C. G. R. Geddes, C. Toth, J. van Tilborg, E. Esarey, C. B. Schroeder, D. Bruhwiler, C. Nieter, J. Cary, and W. P. Leemans, *High-quality electron beams from a laser wakefield accelerator using plasma-channel guiding*, Nature **431**, 538 (2004).

[27] J. Faure, Y. Glinec, A. Pukhov, S. Kiselev, S. Gordienko, E. Lefebvre, J. P. Rousseau, F. Burgy, and V. Malka, *A laser-plasma accelerator producing monoenergetic electron beams*, Nature **431**, 541 (2004).

[28] S. P. D. Mangles, A. G. R. Thomas, M. C. Kaluza, O. Lundh, F. Lindau, A. Persson, F. S. Tsung, Z. Najmudin, W. B. Mori, C. G. Wahlstrom, and K. Krushelnick, *Laser-wakefield acceleration of monoenergetic electron beams in the first plasma-wave period*, Physical Review Letters **96**, 215001 (2006).

[29] C. T. Hsieh, C. M. Huang, C. L. Chang, Y. C. Ho, Y. S. Chen, J. Y. Lin, J. Wang, and S. Y. Chen, *Tomography of injection and acceleration of monoenergetic electrons in a laser-wakefield accelerator*, Physical Review Letters **96**, 095001 (2006).

[30] B. Hidding, K. U. Amthor, B. Liesfeld, H. Schwoerer, S. Karsch, M. Geissler, L. Veisz, K. Schmid, J. G. Gallacher, S. P. Jamison, D. Jaroszynski, G. Pretzler, and R. Sauerbrey, *Generation of quasimonoenergetic electron bunches with 80-fs laser pulses*, Physical Review Letters **96**, 105004 (2006).

[31] T. Hosokai, K. Kinoshita, A. Zhidkov, K. Nakamura, T. Watanabe, T. Ueda, H. Kotaki, M. Kando, K. Nakajima, and M. Uesaka, *Effect of a laser prepulse on a narrow-cone ejection of MeV electrons from a gas jet irradiated by an ultrashort laser pulse*, Physical Review E **67**, 036407 (2003).

[32] S. Karsch, J. Osterhoff, A. Popp, T. P. Rowlands-Rees, Z. Major, M. Fuchs, B. Marx, R. Horlein, K. Schmid, L. Veisz, S. Becker, U. Schramm, B. Hidding, G. Pretzler, D. Habs, F. Gruner, F. Krausz, and S. M. Hooker, *GeV-scale electron acceleration in a gas-filled capillary discharge waveguide*, New Journal of Physics **9**, 415 (2007).

[33] W. P. Leemans, B. Nagler, A. J. Gonsalves, C. Toth, K. Nakamura, C. G. R. Geddes, E. Esarey, C. B. Schroeder, and S. M. Hooker, *GeV electron beams from a centimetre-scale accelerator*, Nature Physics **2**, 696 (2006).

[34] S. P. D. Mangles, A. G. R. Thomas, M. C. Kaluza, O. Lundh, F. Lindau, A. Persson, Z. Najmudin, C. G. Wahlstrom, C. D. Murphy, C. Kamperidis, K. L. Lancaster, E. Divall, and K. Krushelnick, *Effect of laser contrast ratio on electron beam stability in laser wakefield acceleration experiments*, Plasma Physics and Controlled Fusion **48**, B83 (2006).

[35] S. P. D. Mangles, A. G. R. Thomas, O. Lundh, F. Lindau, M. C. Kaluza, A. Persson, C. G. Wahlstrom, K. Krushelnick, and Z. Najmudin, *On the stability of laser wakefield electron accelerators in the monoenergetic regime*, Physics of Plasmas **14**, 056702 (2007).

[36] F. Lindau, O. Lundh, S. P. D. Mangles, M. C. Kaluza, K. Krushelnick, Z. Najmudin, A. Persson, A. G. R. Thomas, and C. G. Wahlstrom, *Characterization of quasi-monoenergetic electron beams at the lund laser centre*, IEEE Transactions on Plasma Science **36**, 1707 (2008).

[37] T. P. Rowlands-Rees, C. Kamperidis, S. Kneip, A. J. Gonsalves, S. P. D. Mangles, J. G. Gallacher, E. Brunetti, T. Ibbotson, C. D. Murphy, P. S. Foster, M. J. V. Streeter, F. Budde, P. A. Norreys, D. A. Jaroszynski, K. Krushelnick, Z. Najmudin, and S. M. Hooker, *Laser-Driven Acceleration of Electrons in a Partially Ionized Plasma Channel*, Physical Review Letters **100**, 1 (Mar 2008).

[38] C. McGuffey, A. G. R. Thomas, W. Schumaker, T. Matsuoka, V. Chvykov, F. J. Dollar, G. Kalintchenko, V. Yanovsky, A. Maksimchuk, K. Krushelnick, V. Y. Bychenkov, I. V. Glazyrin, and A. V. Karpeev, *Ionization Induced Trapping in a Laser Wakefield Accelerator*, Physical Review Letters **104**, 025004 (2010).

[39] A. Pak, K. A. Marsh, S. F. Martins, W. Lu, W. B. Mori, and C. Joshi, *Injection and Trapping of Tunnel-Ionized Electrons into Laser-Produced Wakes*, Physical Review Letters **104**, 025003 (2010).

[40] D. J. Spence, A. Butler, and S. M. Hooker, *First demonstration of guiding of high-intensity laser pulses in a hydrogen-filled capillary discharge waveguide*, Journal of Physics B-Atomic Molecular and Optical Physics **34**, 4103 (2001).

[41] J. Osterhoff, A. Popp, Z. Major, B. Marx, T. P. Rowlands-Rees, M. Fuchs, M. Geissler, R. Hoerlein, B. Hidding, S. Becker, E. A. Peralta, U. Schramm, F. Gruener, D. Habs, F. Krausz, S. M. Hooker, and S. Karsch, *Generation of stable, low-divergence electron beams by laser-wakefield acceleration in a steady-state-flow gas cell*, Physical Review Letters **101**, 085002 (2008).

[42] C. Courtois, A. Couairon, B. Cros, J. R. Marques, and G. Matthieussent, *Propagation of intense ultrashort laser pulses in a plasma filled capillary tube: Simulations and experiments*, Physics of Plasmas **8**, 3445 (2001).

[43] P. Volfbeyn, E. Esarey, and W. P. Leemans, *Guiding of laser pulses in plasma channels created by the ignitor-heater technique*, 40th Annual Meeting of the Division of Plasma Physics of the American-Physical-Society **6**, 2269 (1998).

[44] C. G. Durfee and H. M. Milchberg, *Light Pipe for High-Intensity Laser-Pulses*, Physical Review Letters **71**, 2409 (1993).

[45] K. Krushelnick, A. Ting, C. I. Moore, H. R. Burris, E. Esarey, P. Sprangle, and M. Baine, *Plasma channel formation and guiding during high intensity short pulse laser plasma experiments*, Physical Review Letters **78**, 4047 (1997).

[46] D. Umstadter, J. K. Kim, and E. Dodd, *Laser injection of ultrashort electron pulses into wakefield plasma waves*, Physical Review Letters **76**, 2073 (1996).

[47] J. Faure, C. Rechatin, A. Norlin, A. Lifschitz, Y. Glinec, and V. Malka, *Controlled injection and acceleration of electrons in plasma wakefields by colliding laser pulses*, Nature **444**, 737 (2006).

[48] C. Rechatin, J. Faure, A. Ben-Ismail, J. Lim, R. Fitour, A. Specka, H. Videau, A. Tafzi, F. Burgy, and V. Malka, *Controlling the Phase-Space Volume of Injected Electrons in a Laser-Plasma Accelerator*, Physical Review Letters **102**, 164801 (2009).

[49] X. Davoine, E. Lefebvre, C. Rechatin, J. Faure, and V. Malka, *Cold Optical Injection Producing Monoenergetic, Multi-GeV Electron Bunches*, Physical Review Letters **102**, 065001 (2009).

[50] H. Kotaki, I. Daito, M. Kando, Y. Hayashi, K. Kawase, T. Kameshima, Y. Fukuda, T. Homma, J. Ma, L. M. Chen, T. Z. Esirkepov, A. S. Pirozhkov, J. K. Koga, A. Faenov, T. Pikuz, H. Kiriyama, H. Okada, T. Shimomura, Y. Nakai, M. Tanoue, H. Sasao, D. Wakai, H. Matsuura, S. Kondo, S. Kanazawa, A. Sugiyama, H. Daido, and S. V. Bulanov, *Electron Optical Injection with Head-On and Countercrossing Colliding Laser Pulses*, Physical Review Letters **103**, 194803 (2009).

[51] A. Irman, M. J. H. Luttikhof, A. G. Khachatryan, F. A. van Goor, J. W. J. Verschuur, H. M. J. Bastiaens, and K. J. Boller, *Design and simulation of laser wakefield acceleration with external electron bunch injection in front of the laser pulse*, Journal of Applied Physics **102**, 7 (2007).

[52] W. P. Leemans and E. Esarey, *Laser-driven plasma-wave electron accelerators*, Physics Today **3**, 44 (2009 2009).

[53] P. Chen, J. M. Dawson, R. W. Huff, and T. Katsouleas, *Acceleration of Electrons by the Interaction of a Bunched Electron-Beam with a Plasma*, Physical Review Letters **54**, 693 (1985).

[54] A. Caldwell, K. Lotov, A. Pukhov, and F. Simon, *Proton-driven plasma-wakefield acceleration*, Nature Physics **5**, 363 (2009).

[55] R. Bingham, J. M. Dawson, J. J. Su, and H. A. Bethe, *Collective Interactions between Neutrinos and Dense-Plasmas*, Physics Letters A **193**, 279 (1994).

[56] I. Blumenfeld, C. E. Clayton, F. J. Decker, M. J. Hogan, C. K. Huang, R. Ischebeck, R. Iverson, C. Joshi, T. Katsouleas, N. Kirby, W. Lu, K. A. Marsh, W. B. Mori, P. Muggli, E. Oz, R. H. Siemann, D. Walz, and M. M. Zhou, *Energy doubling of 42 GeV electrons in a metre-scale plasma wakefield accelerator*, Nature **445**, 741 (2007).

[57] A. Rousse, K. Phuoc, R. Shah, A. Pukhov, E. Lefebvre, V. Malka, S. Kiselev, F. Burgy, J.-P. Rousseau, D. Umstadter, and D. Hulin, *Production of a keV X-*

Ray Beam from Synchrotron Radiation in Relativistic Laser-Plasma Interaction, Physical Review Letters **93**, 1 (Sept. 2004).

[58] I. Kostyukov, S. Kiselev, and A. Pukhov, *X-ray generation in an ion channel*, Physics of Plasmas **10**, 4818 (2003).

[59] I. Kostyukov, A. Pukhov, and S. Kiselev, *Phenomenological theory of laser-plasma interaction in "bubble" regime*, Physics of Plasmas **11**, 5256 (2004).

[60] S. Kiselev, A. Pukhov, and I. Kostyukov, *X-ray generation in strongly nonlinear plasma waves*, Physical Review Letters **93**, 135004 (2004).

[61] A. G. R. Thomas and K. Krushelnick, *Betatron x-ray generation from electrons accelerated in a plasma cavity in the presence of laser fields*, Physics of Plasmas **16**, 103103 (2009).

[62] A. G. R. Thomas, *Scalings for radiation from plasma bubbles*, Physics of Plasmas **17**, 056798 (2010).

[63] K. T. Phuoc, F. Burgy, J. P. Rousseau, V. Malka, A. Rousse, R. Shah, D. Umstadter, A. Pukhov, and S. Kiselev, *Laser based synchrotron radiation*, Physics of Plasmas **12**, 023101 (2005).

[64] F. Albert, K. T. Phuoc, R. Shah, S. Corde, R. Fitour, A. Tafzi, F. Burgy, D. Douillet, T. Lefrou, and A. Rousse, *Full characterization of a laser-produced keV x-ray betatron source*, Iop Publishing Ltd, Hersonissos, Greece (2008), 35th European-Physical-Society Conference on Plasma Physics.

[65] F. Albert, R. Shah, K. T. Phuoc, R. Fitour, F. Burgy, J. P. Rousseau, A. Tafzi, D. Douillet, T. Lefrou, and A. Rousse, *Betatron oscillations of electrons accelerated in laser wakefields characterized by spectral x-ray analysis*, Physical Review E **77**, 056402 (2008).

[66] S. Kneip, S. R. Nagel, C. Bellei, N. Bourgeois, A. E. Dangor, A. Gopal, R. Heathcote, S. P. D. Mangles, J. R. Marques, A. Maksimchuk, P. M. Nilson, K. T. Phuoc, S. Reed, M. Tzoufras, F. S. Tsung, L. Willingale, W. B. Mori, A. Rousse, K. Krushelnick, and Z. Najmudin, *Observation of synchrotron radiation from electrons accelerated in a petawatt-laser-generated plasma cavity*, Physical Review Letters **100**, 105006 (2008).

[67] S. P. D. Mangles, G. Genoud, S. Kneip, M. Burza, K. Cassou, B. Cros, N. P. Dover, C. Kamperidis, Z. Najmudin, A. Persson, J. Schreiber, F. Wojda, and C. G. Wahlstrom, *Controlling the spectrum of x-rays generated in a laser-plasma accelerator by tailoring the laser wavefront*, Applied Physics Letters **95**, 181106 (2009).

[68] S. Kneip, C. McGuffey, J. L. Martins, S. F. Martins, C. Bellei, V. Chvykov, F. Dollar, R. Fonseca, C. Huntington, G. Kalintchenko, A. Maksimchuk, S. P. D. Mangles, T. Matsuoka, S. R. Nagel, C. A. J. Palmer, J. Schreiber, K. T. Phuoc, A. G. R. Thomas, V. Yanovsky, L. O. Silva, K. Krushelnick, and Z. Najmudin, *Bright spatially coherent synchrotron X-rays from a table-top source*, Nat Phys **advance online publication** (2010).

[69] S. Kneip, C. McGuffey, F. Dollar, M. S. Bloom, V. Chvykov, G. Kalintchenko, K. Krushelnick, A. Maksimchuk, S. P. D. Mangles, T. Matsuoka, Z. Najmudin, C. A. J. Palmer, J. Schreiber, W. Schumaker, A. G. R. Thomas, and V. Yanovsky, *X-ray phase contrast imaging of biological specimens with femtosecond pulses of betatron radiation from a compact laser plasma wakefield accelerator*, Applied Physics Letters **99**, 093701 (2011).

[70] K. T. Phuoc, S. Corde, R. Shah, F. Albert, R. Fitour, J. P. Rousseau, F. Burgy, B. Mercier, and A. Rousse, *Imaging electron trajectories in a laser-wakefield cavity using betatron x-ray radiation*, Physical Review Letters **97**, 225002 (2006).

[71] K. T. Phuoc, S. Corde, R. Fitour, R. Shah, F. Albert, J. P. Rousseau, F. Burgy, A. Rousse, V. Seredov, and A. Pukhov, *Analysis of wakefield electron orbits in plasma wiggler*, Physics of Plasmas **15**, 073106 (2008).

[72] K. T. Phuoc, R. Fitour, A. Tafzi, T. Garl, N. Artemiev, R. Shah, F. Albert, D. Boschetto, A. Rousse, D. E. Kim, A. Pukhov, V. Seredov, and I. Kostyukov, *Demonstration of the ultrafast nature of laser produced betatron radiation*, Physics of Plasmas **14**, 080701 (2007).

[73] A. G. Khachatryan, F. A. van Goor, and K. J. Boller, *Coherent and incoherent radiation from a channel-guided laser wakefield accelerator*, New Journal of Physics **10**, 083043 (2008).

[74] S. Q. Wang, C. E. Clayton, B. E. Blue, E. S. Dodd, K. A. Marsh, W. B. Mori, C. Joshi, S. Lee, P. Muggli, T. Katsouleas, F. J. Decker, M. J. Hogan, R. H. Iverson, P. Raimondi, D. Walz, R. Siemann, and R. Assmann, *X-ray emission from betatron motion in a plasma wiggler*, Physical Review Letters **88**, 135004 (2002).

[75] C. E. Clayton, B. E. Blue, E. S. Dodd, C. Joshi, K. A. Marsh, W. B. Mori, S. Wang, P. Catravas, S. Chattopadhyay, E. Esarey, W. P. Leemans, R. Assmann, F. J. Decker, M. J. Hogan, R. Iverson, P. Raimondi, R. H. Siemann, D. Walz, T. Katsouleas, S. Lee, and P. Muggli, *Transverse envelope dynamics of a 28.5-GeV electron beam in a long plasma*, Physical Review Letters **88**, 154801 (2002).

[76] J. M. J. Madey, *Stimulated Emission of Bremsstrahlung in a Periodic Magnetic Field*, Journal of Applied Physics **42**, 1906 (1971).

[77] F. Gruner, S. Becker, U. Schramm, M. Fuchs, R. Weingartner, D. Habs, J. Meyer-Ter-Vehn, M. Geissler, M. Ferrario, L. Serafini, B. Van Der Geer, H. Backe, W. Lauth, and S. Reiche, *Design considerations for table-top, laser-based VUV and X-ray free electron lasers*, Applied Physics B-Lasers and Optics **86**, 431 (2007).

[78] H. P. Schlenvoigt, K. Haupt, A. Debus, F. Budde, O. Jackel, S. Pfotenhauer, H. Schwoerer, E. Rohwer, J. G. Gallacher, E. Brunetti, R. P. Shanks, S. M. Wiggins, and D. A. Jaroszynski, *A compact synchrotron radiation source driven by a laser-plasma wakefield accelerator*, Nature Physics **4**, 130 (2008).

[79] M. Fuchs, R. Weingartner, A. Popp, Z. Major, S. Becker, J. Osterhoff, I. Cortrie, B. Zeitler, R. Horlein, G. D. Tsakiris, U. Schramm, T. P. Rowlands-Rees, S. M. Hooker, D. Habs, F. Krausz, S. Karsch, and F. Gruner, *Laser-driven soft-X-ray undulator source*, Nature Physics **5**, 826 (2009).

[80] P. Gibbon, *Short Pulse Laser Interactions with Matter an Introdution*, Imperial College Press (2005).

[81] A. Akhiezer and R. Polovin, *Theory of Wave Motion of an Electron Plasma*, Soviet Physics JETP **3**, 696 (1956).

[82] A. Decoster, *Nonlinear travelling waves in a homogeneous cold collisionless plasma*, Physics Reports **47**, 285 (1978).

[83] R. J. Noble, *Plasma-wave generation in the beat-wave accelerator*, Physical Review A **32** (1985).

[84] J. D. Oberman and Carl, *High-Frequency Conductivity and the Emission and Absorption Coefficients of a Fully Ionized Plasma*, Physics of Fluids **5**, 517 (1962).

[85] J. M. Dawson, *Nonlinear Electron Oscillations in a Cold Plasma*, Physical Review **113**, 383 (1959).

[86] E. Esarey, C. Schroeder, and W. Leemans, *Physics of laser-driven plasma-based electron accelerators*, Reviews of Modern Physics **81**, 1229 (Aug. 2009).

[87] Y. Glinec, J. Faure, A. Guemnie-Tafo, V. Malka, H. Monard, J. P. Larbre, V. De Waele, J. L. Marignier, and M. Mostafavi, *Absolute calibration for a broad range single shot electron spectrometer*, Review of Scientific Instruments **77**, 103301 (2006).

[88] P. Kirkpatrick, *On the Theory and Use of Ross Filters*, Review of Scientific Instruments **10**, 186 (1939).

[89] S. Kneip, *Laser Plasma Accelerator and Wiggler*, Ph.D. Thesis, Imperial College London (2010).

[90] E. Esarey, B. Shadwick, P. Catravas, and W. Leemans, *Synchrotron radiation from electron beams in plasma-focusing channels*, Physical Review E **65**, 1 (May 2002).

[91] B. Lab, *X-Ray Interactions With Matter Database* http://henke.lbl.gov/optical_constants/filter2.html (November 2013).

[92] P. Instruments, http://www.princetoninstruments.com (June 2013).

[93] P. Instruments, *CCD Primer: Fiber Optics* http://www.princetoninstruments.com/cms/index.php/ccd-primer/151-fiber-optics (December 2011).

[94] J. R. Janesick, *Scientific charge-coupled devices*, Vol. 117, SPIE press Bellingham, WA (2001).

[95] J. Smith and M. Storm, *Generalized Off-Axis Distributions from Disk Sources of Radiation*, Journal of Applied Physics **c**, 519 (1954).

[96] E. Hussein, *Handbook on Radiation Probing, Gauging, Imaging and Analysis*, Vol. 1, Springer (2003).

[97] S. Semushin and V. Malka, *High density gas jet nozzle design for laser target production*, Review of Scientific Instruments **72**, 2961 (2001).

[98] A. Buck, K. Zeil, A. Popp, K. Schmid, A. Jochmann, S. D. Kraft, B. Hidding, T. Kudyakov, C. M. S. Sears, L. Veisz, S. Karsch, J. Pawelke, R. Sauerbrey, T. Cowan, F. Krausz, and U. Schramm, *Absolute charge calibration of scintillating screens for relativistic electron detection*, Review of Scientific Instruments **81** (2010).

[99] S. P. D. Mangles, G. Genoud, M. S. Bloom, M. Burza, Z. Najmudin, A. Persson, K. Svensson, A. G. R. Thomas, and C.-G. Wahlström, *Self-injection threshold in self-guided laser wakefield accelerators*, Physical Review Special Topics - Accelerators and Beams **15**, 011302 (Jan. 2012).

[100] W. Leemans, P. Catravas, E. Esarey, C. Geddes, C. Toth, R. Trines, C. Schroeder, B. Shadwick, J. van Tilborg, and J. Faure, *Electron-Yield Enhancement in a Laser-Wakefield Accelerator Driven by Asymmetric Laser Pulses*, Physical Review Letters **89**, 174802 (Oct. 2002).

[101] I. Kostyukov, A. Pukhov, and S. Kiselev, *Phenomenological theory of laser-plasma interaction in bubble regime*, Physics of Plasmas **11**, 5256 (2004).

[102] A. G. R. Thomas, *Scalings for radiation from plasma bubbles*, Physics of Plasmas **17**, 056708 (2010).

[103] C. Decker, W. Mori, K. Tzeng, and T. Katsouleas, *The evolution of ultraintense, shortpulse lasers in underdense plasmas*, Physics of Plasmas **3**, 2047 (1996).

[104] W. Lu, M. Tzoufras, C. Joshi, F. Tsung, W. Mori, J. Vieira, R. Fonseca, and L. Silva, *Generating multi-GeV electron bunches using single stage laser wake-*

field acceleration in a 3D nonlinear regime, Physical Review Special Topics - Accelerators and Beams **10**, 061301 (Jun. 2007).

[105] J. Schreiber, C. Bellei, S. P. D. Mangles, C. Kamperidis, S. Kneip, S. R. Nagel, C. A. J. Palmer, P. P. Rajeev, M. J. V. Streeter, and Z. Najmudin, *Complete Temporal Characterization of Asymmetric Pulse Compression in a Laser Wakefield*, Physical Review Letters **105**, 235003 (Dec. 2010).

[106] D. H. Froula, C. E. Clayton, T. Döppner, K. A. Marsh, C. P. J. Barty, L. Divol, R. A. Fonseca, S. H. Glenzer, C. Joshi, W. Lu, S. F. Martins, P. Michel, W. B. Mori, J. P. Palastro, B. B. Pollock, A. Pak, J. E. Ralph, J. S. Ross, C. W. Siders, L. O. Silva, and T. Wang, *Measurements of the Critical Power for Self-Injection of Electrons in a Laser Wakefield Accelerator*, Physical Review Letters **103**, 1 (Nov. 2009).

[107] C. Huang, W. Lu, M. Zhou, C. Clayton, C. Joshi, W. Mori, P. Muggli, S. Deng, E. Oz, T. Katsouleas, M. Hogan, I. Blumenfeld, F. Decker, R. Ischebeck, R. Iverson, N. Kirby, and D. Walz, *Hosing Instability in the Blow-Out Regime for Plasma-Wakefield Acceleration*, Physical Review Letters **99** (Dec. 2007).

[108] P. Chen, J. Dawson, R. Huff, and T. Katsouleas, *Acceleration of Electrons by the interaction of a bunched electron beam with a plasma*, Physical review letters (1985).

[109] C. M. Huntington, A. G. R. Thomas, C. McGuffey, T. Matsuoka, V. Chvykov, G. Kalintchenko, S. Kneip, Z. Najmudin, C. Palmer, V. Yanovsky, A. Maksimchuk, R. P. Drake, T. Katsouleas, and K. Krushelnick, *Current Filamentation Instability in Laser Wakefield Accelerators*, Physical Review Letters **106**, 105001 (Mar 2011).

[110] I. Kostyukov, A. Pukhov, and S. Kiselev, *Phenomenological theory of laser-plasma interaction in bubble regime*, Physics of Plasmas **11**, 5256 (2004).

[111] A. Rousse, K. Ta Phuoc, R. Shah, R. Fitour, and F. Albert, *Scaling of betatron X-ray radiation*, The European Physical Journal D **45**, 391 (Aug. 2007).

[112] S. P. D. Mangles, G. Genoud, S. Kneip, M. Burza, K. Cassou, B. Cros, N. P. Dover, C. Kamperidis, Z. Najmudin, A. Persson, J. Schreiber, F. Wojda, and

C.-G. Wahlstrom, *Controlling the spectrum of x-rays generated in a laser-plasma accelerator by tailoring the laser wavefront*, Applied Physics Letters **95**, 181106 (2009).

[113] G. Genoud, *Laser-Driven Plasma Wave for Particle Acceleration and X-Ray Production*, Ph.D. Thesis, Lund University (2011).

[114] C. Thaury, K. Phuoc, and S. Corde, *Probing electron acceleration and x-ray emission in laser-plasma accelerators*, Physics of Plasmas (... **063101**, 2 (2013).

[115] S. Corde, K. Phuoc, R. Fitour, J. Faure, A. Tafzi, J. Goddet, V. Malka, and A. Rousse, *Controlled Betatron X-Ray Radiation from Tunable Optically Injected Electrons*, Physical Review Letters **107**, 2 (Dec. 2011).

[116] S. Kneip, C. McGuffey, J. L. Martins, S. F. Martins, C. Bellei, V. Chvykov, F. Dollar, R. Fonseca, C. Huntington, G. Kalintchenko, A. Maksimchuk, S. P. D. Mangles, T. Matsuoka, S. R. Nagel, C. A. J. Palmer, J. Schreiber, K. T. Phuoc, A. G. R. Thomas, V. Yanovsky, L. O. Silva, K. Krushelnick, and Z. Najmudin, *Bright spatially coherent synchrotron X-rays from a table-top source*, Nature Physics **6**, 980 (Oct. 2010).

[117] J. Jackson, *Classical Electrodynamics 3rd Ed*, Wiley (1998).

[118] J. Jackson, *Classical Electrodynamics 2nd Ed*, Wiley (1962).

[119] R. S. D. Meeting, *http://rsta.royalsocietypublishing.org/content/372/2010.toc* (March 2014).